

## ABSTRACT

### Multi-Strange Baryon Correlations at RHIC

Betty I. Bezverkhny Abelev

Yale University

May 2007

A hot and dense medium is produced in central Au<sup>197</sup>+Au<sup>197</sup> collisions at  $\sqrt{s_{NN}} = 200$  GeV at the Relativistic Heavy Ion Collider (RHIC) in Brookhaven National Laboratory. A particular puzzle has been the origin of hadrons produced in the intermediate transverse momentum ( $2 < p_T < 6$  GeV/c) region. Recombination and Coalescence models have been proposed to explain the mechanism of particle production in this energy range. Because the production of  $s$ -quarks via parton fragmentation is suppressed in the  $p_T$  region of interest with respect to the lighter quarks, the fragmentation contribution of  $s$ -quarks to strange particles should also be suppressed. Therefore, particles made entirely of  $s$  and  $\bar{s}$  quarks which originated from fragmentation are not expected to be detected. A statistical measurement of jets via azimuthal correlations using multi-strange ( $\Xi^\pm$  and  $\Omega^\pm$ ) baryons as trigger particles is performed in the most central Au+Au collisions. Contrary to predictions, a strong same-side peak (correlated with the jet direction) with non-zero yield has been observed in both cases. The correlation function for  $\Xi$  baryons is also studied as a function of pseudorapidity  $\eta$  and azimuthal angle  $\phi$ . An elongation in  $\Delta\eta$ , commonly called the "ridge", is observed under the trigger-particle (same-side) peak.

The  $\Xi^\pm$  correlation function with charged particles has been obtained in  $p+p$  and  $d+Au$  minimum bias collisions for comparison with that in central Au+Au events. While there are insufficient statistics to calculate the same-side yields in the  $p+p$  data, the yield in the  $d+Au$  data is extracted. Correlation functions are also studied in events triggered on high-energy deposits in the electromagnetic calorimeter. These will be presented along with the possibility of using the STAR calorimeter as an anti-baryon trigger.



# Multi-Strange Baryon Correlations at RHIC

A Dissertation  
Presented to the Faculty of the Graduate School  
of  
Yale University  
in Candidacy for the Degree of  
Doctor of Philosophy

By  
Betty I. Bezverkhny Abelev

Dissertation Director: John Harris

May 2007

© Copyright 2007

by

Betty I. Bezverkhny Abelev

**All Rights Reserved**

Моему папе.

# Acknowledgements

First of all, my gratitude goes to John W. Harris, who took me on, even though I had zero heavy ion experience, and who stuck by me through all the lows (and highs!) of grad school. I am incredibly fortunate to have you as my mentor. Thank you, my dear Helen Caines – for your infinite patience, and wisdom, and friendship. You’re a true role model, and I am looking forward to working with you and John for many years to come.

Thank you to the rest of my patient dissertation committee – Walter Goldberger, Bonnie Fleming, and Keith Baker. I am very grateful to Rene Bellwied, who not only greatly encouraged and inspired this work, but also agreed to be my outside reader.

I absolutely have to thank people without whom I would probably never make it to graduate school: Roger Tobin – who always believed in me; my first physics teacher, Irina Alekseevna Zimneva, who’s taken our band of unruly 12 year-olds to St. Petersburg Faculty of Physics demonstrations and made sure experiments were interesting; Ilya Shlyakhter, who forced me to write the best admissions essay I possibly could; and my dear babushka Rita, my first true mentor and my first inspiration – I hope I fulfilled your wishes by, as you say, at least 80%. I know you believe in me too.

Thank you to the best Relativistic Heavy Ion Group ever – its members, past and present, for invaluable discussions, for answering my stupid and not-so-stupid questions – Mike Miller, the best gossip; Jon Gans, the best purveyor of all things sarcastic; Matt Horsley, via whom we first found out about 9/11; Manuel Calderón de la Barca Sánchez, who explained to me what *multiplicity* was, and who defended his thesis on that memorable 9/11; Boris Hippolyte, the best ever neighbor; Christina

Markert, the handiest physicist I know; Nikolai Smirnov, the best source of all things sweet and all things detector; and everyone else who are also the best – Thomas Ullrich, Richard Witt and Mark Heinz, Oana Catu and Christine Nattrass, Stephen Baumgardt and Anders Knospe, and Matt Lamont, of course. My darling three JB's: Jaro, Jano, and Kubo – I hope for many meetings and gatherings and opportunities to see each other, at work and otherwise.

Thank you to my other fellow STAR collaborators for teaching me the basics of, well, everything – Gene Van Buren, Julien Faivre, Jérôme Baudot and Jérôme Lauret, and to Ying Guo, who pioneered strange particles correlations.

I am proud to be one of the five Yale 2000 women, Sarah Bickman, Grace Chern, Veronica Savu, and Sevil Salur, whose friendship and help have sustained me over these six and a half years. I don't have enough words of gratitude for Veronica and Sevil – my best friend and my best mate – we've shared so much – good and bad – and yet I hope to share so much much more in the future! Also my thanks and appreciation go to the best lab partner and hugger ever – Aric Sanders, a fellow Yale 2000 – and to Dale Li, who, together with Aric, Sarah, and me made up the most desperate study groups Yale has ever seen.

Finally, thank you to my wonderful family, but most of all to my мама and папа, Raya and Igor, who've raised me a person, not a girl, and to my sister Fannya – who is everything I am – and more. And Max. Without you nothing would be possible. Nothing. You are my heart, my love, my inspiration, мой зислмойс.

It's hard to believe that this part of my life is now over. To new beginnings!

# Contents

<b>Acknowledgements</b>	<b>iv</b>
<b>1 Introduction</b>	<b>1</b>
1.1 Strangeness production as a QGP signature . . . . .	6
1.1.1 Strangeness enhancement in the QGP . . . . .	6
1.1.2 Suppression of the high momentum spectra . . . . .	9
1.1.3 Other QGP signatures . . . . .	15
1.2 Strange hadron measurements at intermediate $p_T$ . . . . .	17
1.3 Theoretical framework at intermediate $p_T$ . . . . .	20
1.4 Thesis outline . . . . .	23
<b>2 Experimental Setup</b>	<b>24</b>
2.1 RHIC . . . . .	24
2.1.1 Mechanics of particle acceleration . . . . .	26
2.1.2 Interaction areas . . . . .	27
2.2 STAR . . . . .	31
2.2.1 The STAR Magnet . . . . .	33
2.2.2 Tracking Detectors . . . . .	34
2.2.3 Calorimetry . . . . .	40
2.2.4 Triggering detectors . . . . .	41
2.2.5 STAR Data Acquisition System . . . . .	45
<b>3 Data Reconstruction and Simulations</b>	<b>46</b>
3.1 Event Reconstruction . . . . .	46

3.1.1	Tracking and Track Selection . . . . .	47
3.1.2	Event Vertexing and Primary Track Finding . . . . .	49
3.2	$\Xi$ and $\Omega$ Baryon Reconstruction . . . . .	51
3.2.1	$\Xi$ baryons . . . . .	53
3.2.2	$\Omega$ Baryons . . . . .	55
3.3	$\Xi$ and $\Omega$ baryons correlation candidates . . . . .	56
3.3.1	$p + p$ . . . . .	56
3.3.2	$d$ +Au . . . . .	57
3.3.3	Au+Au . . . . .	58
3.4	Constructing a correlation function . . . . .	60
3.5	Correcting for detector acceptance . . . . .	64
3.5.1	Mixed events correction . . . . .	64
3.5.2	Associated track efficiency correction . . . . .	67
3.6	Monte-Carlo Simulations . . . . .	70
3.6.1	PYTHIA . . . . .	70
<b>4</b>	<b>Data Analysis</b>	<b>73</b>
4.1	$p$ + $p$ . . . . .	73
4.1.1	Minimum bias $p + p$ collisions . . . . .	73
4.1.2	High-tower triggered events and trigger Bias . . . . .	76
4.2	$d$ +Au . . . . .	80
4.2.1	Correlations . . . . .	82
4.3	Au+Au . . . . .	82
4.3.1	Selection of associated tracks . . . . .	84
4.3.2	Flow subtraction . . . . .	84
4.3.3	The ZYAM method . . . . .	92
4.3.4	Correlations . . . . .	93
<b>5</b>	<b>Interpretation and Context</b>	<b>107</b>
5.1	Comparison to other correlation measurements . . . . .	108
5.1.1	$p + p$ measurement . . . . .	108
5.1.2	$d$ +Au measurement . . . . .	109

5.1.3	Au+Au results . . . . .	111
5.1.4	Other RHIC experiments . . . . .	114
5.2	Discussion . . . . .	115
5.3	Conclusion . . . . .	119
5.4	Outlook . . . . .	119
<b>A</b>	<b>Kinematic Variables</b>	<b>121</b>
<b>B</b>	<b>Centrality definition in Au+Au collisions</b>	<b>123</b>
	<b>Bibliography</b>	<b>135</b>

# List of Figures

1.1	A schematic phase diagram of nuclear matter . . . . .	4
1.2	Possible scenarios for a relativistic heavy-ion collision evolution . . . .	5
1.3	The Feynman diagrams of $s\bar{s}$ pair production . . . . .	7
1.4	Volume dependence of strange baryon densities . . . . .	8
1.5	A cartoon representation of a charged particle spectrum . . . . .	9
1.6	Evidence of energy loss due to a the dense medium in central Au+Au collisions . . . . .	12
1.7	$R_{AA}$ , $R_{AB}$ and calculation that include only hadronic energy loss . . .	12
1.8	The $R_{CP}$ as a function of $p_T$ for $(h^+ + h^-)/2$ . . . . .	13
1.9	$\Lambda/K_S^0$ ratio in four Au+Au collision centrality regions and $p + p$ data	17
1.10	Nuclear modification factors for strange particles . . . . .	18
1.11	A cartoon illustrating possible particle production mechanisms . . . .	21
1.12	$\Lambda^0$ and $\Omega$ baryon spectra and the Oregon Recombination Model calculations . . . . .	21
2.1	The diagram of RHIC accelerator-collider complex . . . . .	25
2.2	A beam's eye and side view of the PHENIX detector . . . . .	28
2.3	The geometrical acceptances of the PHOBOS silicon detectors . . . .	30
2.4	Photographs of the STAR detector and a seam between two TPC read-out boards . . . . .	31
2.5	A schematic representation of the STAR detector . . . . .	32
2.6	A schematic representation of the longitudinal cross-section of the STAR magnet . . . . .	33

2.7	Measurement of the radial component of the STAR magnetic field, as a function of axial ( $z$ ) position at three radii taken at $\phi = 0^\circ$ . . . . .	34
2.8	The layout of the Time Projection Chamber . . . . .	35
2.9	The layout of a TPC sector and readout pad . . . . .	36
2.10	A schematic representation of a TPC cluster in STAR coordinates . . . . .	39
2.11	$dE/dx$ vs. total momentum of particles found in TPC . . . . .	39
2.12	The position of ZDCs with respect to the interaction area . . . . .	42
2.13	Trigger definitions in Au+Au collisions at $\sqrt{s_{NN}} = 200$ GeV . . . . .	43
3.1	Visualization of the track helix in two projections . . . . .	48
3.2	Tracks seen in the TPC . . . . .	51
3.3	The topology of a cascade decay . . . . .	54
3.4	The invariant mass of $\Xi^-$ and $\bar{\Xi}^+$ baryons (with $p_T > 2$ GeV/c) in $\sqrt{s} = 200$ GeV minimum bias $p + p$ data . . . . .	56
3.5	The invariant mass of $\Xi^-$ and $\bar{\Xi}^+$ baryons (with $p_T > 2$ GeV/c) in $\sqrt{s_{NN}} = 200$ GeV $d$ +Au data . . . . .	58
3.6	The $\Xi$ baryon invariant mass peak in $\sqrt{s_{NN}} = 200$ GeV 0-10% central Au+Au collisions used for correlations measured with $2.5 < p_T$ -trigger $< 4.5$ GeV . . . . .	61
3.7	$\Omega$ baryon (at $2.5 < p_T < 4.5$ GeV/c) signal in Au+Au central data after the initial filtering cuts . . . . .	62
3.8	Correlated background of $\Omega$ baryons . . . . .	64
3.9	The final $\Omega$ baryon invariant mass peak in $\sqrt{s_{NN}} = 200$ GeV 0-10% central Au+Au collisions used for correlations . . . . .	65
3.10	Calculating the $\Delta\phi$ . . . . .	66
3.11	Raw distributions of associated tracks in $\eta$ and $\phi$ . . . . .	67
3.12	Mixed events correlation functions . . . . .	67
3.13	2-dimensional detector acceptance function . . . . .	68
3.14	Charged track finding efficiency in two Au+Au centrality bins . . . . .	68
3.15	A Monte-Carlo simulation of a $\Xi^-$ decay in vacuum . . . . .	69

3.16	$\Xi$ -charged track correlation function constructed using PYTHIA-generated particles . . . . .	71
3.17	$\Xi$ spectra from PYTHIA and $p + p$ minimum bias collisions . . . . .	72
4.1	$\Xi^\pm$ - $h^\pm$ correlations in Year 2002 minimum bias $p + p$ data . . . . .	74
4.2	Reference event charged particle multiplicity as a function of $p_T$ of the $\Xi^\pm$ . . . . .	75
4.3	$\Xi^-$ corrected spectrum in 3 event multiplicity bins . . . . .	76
4.4	$\Xi^-$ and $\bar{\Xi}^+$ rapidity distributions in $p + p$ minimum bias data . . . . .	77
4.5	Uncorrected minimum bias and high- $p_T$ triggered $\Xi^-$ spectra . . . . .	78
4.6	Uncorrected minimum bias and high- $p_T$ triggered charged spectra . . . . .	79
4.7	Multiplicity distributions of three $p + p$ event classes . . . . .	80
4.8	Raw $\Xi$ baryon correlations with charged tracks in high- $p_T$ triggered data set . . . . .	80
4.9	Normalized correlations: $\Xi^-$ correlated with charged tracks . . . . .	81
4.10	Number of uncorrected charged tracks per $\Xi$ in an eligible $\sqrt{s_{NN}} = 200$ GeV $d$ +Au minimum bias event . . . . .	82
4.11	$\Xi$ baryon correlation function in $d$ +Au collisions . . . . .	83
4.12	The physics of spatial asymmetry . . . . .	85
4.13	Schematic representation of the event plane . . . . .	87
4.14	Multi-strange baryon flow in 0-80% Minimum Bias events . . . . .	90
4.15	Quark scaling including multi-strange baryons . . . . .	91
4.16	Parameterized $v_2$ in two centrality bins . . . . .	92
4.17	$\Xi^\pm$ - $h^\pm$ correlation functions in six $p_T$ -trigger bins . . . . .	96
4.18	$\Xi^\pm$ - $h^\pm$ correlation function yields . . . . .	97
4.19	Raw $\Omega$ correlation function, corrected for associated track efficiency . . . . .	98
4.20	$\Omega$ and $\Xi$ correlation functions in 0-10% central Au+Au collisions . . . . .	99
4.21	$\Xi$ and $\Omega$ correlation functions after background subtraction . . . . .	100
4.22	2D charged-charged correlation functions . . . . .	101
4.23	$\Xi^\pm$ - $h^\pm$ correlation analysis in $\Delta\phi \times \Delta\eta$ . . . . .	104
4.24	A schematic representation of a 2-dimensional correlation function . . . . .	105

4.25	Fits to the ridge-only region ( $0.7 <  \Delta\eta  < 1.4$ ) and the ridge+jet region ( $ \Delta\eta  < 0.7$ ) same-side peaks . . . . .	105
4.26	The remainder of the subtraction of the $0.7 <  \Delta\eta  < 1.4$ correlation function slice from the $ \Delta\eta  < 0.7$ slice . . . . .	106
5.1	Integrated jet yields as a function of collision centrality . . . . .	110
5.2	Jet yield as a function of trigger particle $p_T$ in 0-10% central Au+Au collisions . . . . .	111
5.3	Correlation functions after elliptic flow subtraction . . . . .	112
5.4	Jet+Ridge yields of strange particles in 0-10% central Au+Au collisions	113
5.5	Jet yields in Au+Au from PHENIX . . . . .	115
5.6	Armesto et al: a Sketch of parton radiation in various environments .	118
B.1	A representation of two Au ions colliding . . . . .	124
B.2	$\sqrt{s_{NN}} = 200$ GeV Au+Au minimum bias distribution with centrality definitions . . . . .	125
B.3	Central trigger event selection . . . . .	126
B.4	Event selection for this thesis. . . . .	127

# List of Tables

1.1	The quark family of elementary particles . . . . .	2
3.1	Selected properties of the multi-strange baryons and their decays . . .	50
3.2	Reconstruction level cuts on cascade-type vertices . . . . .	53
3.3	Selection parameters for $\Xi^-$ and $\bar{\Xi}^+$ baryons with ( $p_T > 2$ GeV) in $\sqrt{s} = 200$ GeV $p + p$ minimum bias data. . . . .	57
3.4	Selection parameters for $\Xi^-$ and $\bar{\Xi}^+$ baryons with $p_T > 2.0$ GeV/c in $\sqrt{s_{NN}}$ $d+Au$ data. . . . .	59
3.5	Selection parameters for $\Xi^-$ and $\bar{\Xi}^+$ baryons in $\sqrt{s_{NN}} = 200$ GeV 0-10% central Au+Au data . . . . .	60
3.6	Omega cut parameters used to obtain the particles in the Au+Au correlation function . . . . .	63
4.1	Parameters used for $v_2$ parametrization as a function of centrality class	92
4.2	Centrality and mean $p_T$ parameters for $\Xi^\pm$ - $h^\pm$ correlation functions. .	95
4.3	Flow parameters for 6 $\Xi$ $p_T$ -trigger bins . . . . .	95
4.4	Multiplicity and associated and trigger particle $\langle p_T \rangle$ parameters used to produce the correlation functions in Figure 4.20. . . . .	99

# Chapter 1

## Introduction

It is now almost universally accepted that the matter surrounding us today was created billions of years ago in an explosion termed “The Big Bang.” It is believed that after the occurrence of the Big Bang the Universe expanded and cooled to become what we are currently observing: an isotropic region of uncertain boundaries and a background temperature of 2.7K. However, if we were to observe the Universe a millisecond after the Big Bang, our observations would be very different. The temperature of what was then the Universe is thought to have been on the order of trillions of degrees Kelvin, and the dominating state of matter was a soup of weakly-interacting or non-interacting elementary particles including quarks and gluons, which we call the Quark-Gluon Plasma (QGP).

As the universe cooled, quarks and gluons became bound in hadrons, three quark (baryon) or quark-anti-quark (meson) objects. This is the way we encounter quarks today, in our every day, ordinary cold nuclear matter. To understand the nature of the Universe just after the Big Bang and to study quark properties, we must first understand what makes the quarks bind to make hadrons, and what conditions must be met in order for quarks to become unbound.

All known elementary particles are described by the Standard Model of particle interactions. In the Standard Model, particles can be classified as leptons, quarks, or interaction mediators. The leptons are described by the three leptonic quantum numbers and electric charge, while quarks are described by their flavor (the equivalent

quark	charge	name	bare mass [MeV]
u	$+\frac{2}{3}$	up	1.5-3.0
d	$-\frac{1}{3}$	down	3-7
s	$-\frac{1}{3}$	strange	$95 \pm 25$
c	$+\frac{2}{3}$	charm	$1250 \pm 90$
t	$+\frac{2}{3}$	top	$174200 \pm 3300$
b	$-\frac{1}{3}$	bottom	$4200 \pm 70$

Table 1.1: The quark family of elementary particles. The masses are taken from [1].

of the leptonic quantum number), charge, and *color*, an additional quantum number. A quark can have one of three colors, *R* (red), *G* (green), and *B* (blue). Hadrons are colorless, i.e., they are either composed of a quark and an anti-quark of the same color, or are made up of three *RGB* quarks (anti-quarks). Quarks are fermions (all have a spin of  $1/2$ ), and if not for color, the Pauli exclusion principle would forbid three-quark states of the same flavor. The *RGB* quantum number enables us to describe states of three quarks of the same flavor, such as the  $\Delta^{++}$  baryon, made up of three *u* (up) quarks. Masses and charges of all six quarks are listed in Table 1.1.

The interaction between quarks is described by a field theory called Quantum Chromodynamics (QCD), which in many respects is similar to Quantum Electrodynamics. However, there is an important difference. The “charge” in QCD is color. Gluons, which act as color mediators, make up a color octet ( $R\bar{G}$ ,  $R\bar{B}$ ,  $G\bar{R}$ ,  $G\bar{B}$ ,  $B\bar{R}$ ,  $B\bar{G}$ ,  $\sqrt{\frac{1}{2}}(R\bar{R} - G\bar{G})$ , and  $\sqrt{\frac{1}{6}}(R\bar{R} + G\bar{G} - 2B\bar{B})$ ). Because gluons carry color, they can self-interact. This introduces a peculiar condition. The strong force between two quarks does not decrease with distance, but grows stronger. The potential between two quarks can be written as

$$V(r) = -\frac{4\alpha_s}{3r} + kr \quad (1.1)$$

where  $\alpha_s$  is the strong coupling constant,  $4/3$  is the color factor,  $r$  is the distance between two quarks, and  $k$  is a constant, experimentally determined to be about 16 tons (166 kN or about 1 GeV/fm) [2]. At large distances the first term in Eq. 1.1 becomes negligible and the equation becomes linearly dependent on  $r$ . Thus it is clear that the energy of the field between two quarks can grow arbitrary large with

increasing distances. This is what is known as “confinement” - the quarks cannot be separated by being pulled apart; as the quarks separate, it becomes energetically favorable to produce a quark-anti-quark pair from the vacuum to reduce the original two-quark potential [3].

Thus we know that quarks cannot be separated physically. However, it is also true that when momentum transfer becomes large,  $\alpha_s$  (the measure of strength of the force between two quarks) decreases. Ref. [2] expresses the strong coupling constant,  $\alpha_s$ , in terms of momentum transfer  $q^2$  and  $\Lambda_{QCD}$ , a constant thought to be between 100 and 500 MeV as

$$\alpha_s(|q^2|) = \frac{12\pi}{(11n - 2f)\ln(|q^2|/\Lambda^2)} \quad (1.2)$$

Here  $n$  stands for the number of colors (3 in the Standard Model), and  $f$  for the number of flavors (6 in the Standard Model). Thus, it is enough to decrease the distance between quarks (Eq. 1.1) and increase the energy transfer in order for the quarks to become deconfined. This effect is called *asymptotic freedom*. The QGP has long been thought to be a state of equilibrated matter, where asymptotic freedom has been established.

How does one go about creating the QGP? Looking at the schematic diagram of the phases of nuclear matter, shown in figure 1.1, we see that the early Universe conditions included zero baryo-chemical potential,  $\mu_B$  (an equal amount of quarks and anti-quarks), and very high temperatures. A QGP might already exist in neutron stars and supernovae, made entirely of baryonic matter (high  $\mu_B$ ), with extremely high baryon densities and temperatures much lower than the 170 MeV shown in the figure (the number comes from the critical temperature at  $\mu_B = 0$  in calculations on a 2 and 3 quark lattice, and is thought to be about 170 MeV). However, these are inaccessible for study. Thus we attempt to approximate the  $\mu_B$  condition, which is similar to that of the Big Bang, in a laboratory. To do this, facilities were built to collide ions as heavy as Au or Pb in hopes of creating a state of matter with partonic degrees of freedom.

The field of relativistic heavy ion collisions (RHI) has been in existence for over

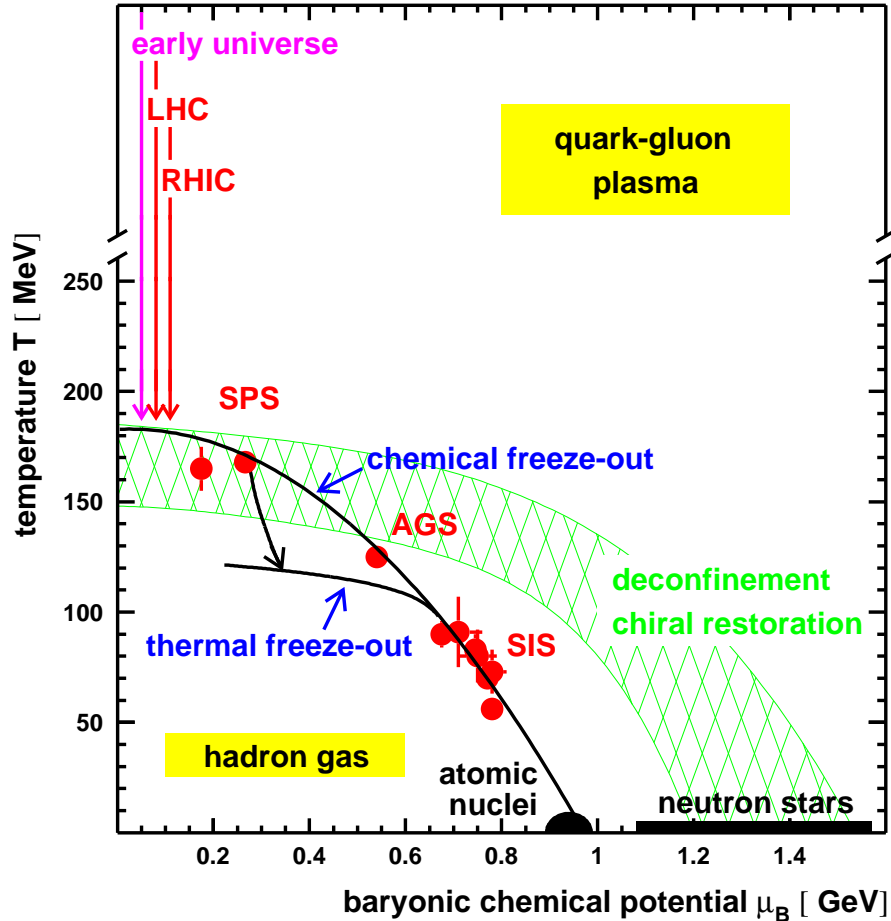


Figure 1.1: A schematic phase diagram of nuclear matter, adopted from [4]. Heavy ion collisions at RHIC are thought to be at low baryon chemical potential and temperatures greater than or equal to 170 MeV. See text for details.

thirty years. The phase-transition diagram also indicates the  $T$ - $\mu_B$  phase-space accessible to facilities used for RHI in the past: SIS (Superconducting Synchrotron), AGS (Alternating Gradient Synchrotron), and SPS (Super Proton Synchrotron). Currently, extensive preparations are taking place for the heavy ion program to open at the Large Hadron Collider (LHC) at CERN. Recent studies, including this, have been done using the data obtained at the Brookhaven National Laboratory's Relativistic Heavy Ion Collider (RHIC). The experimental setup will be described in detail in

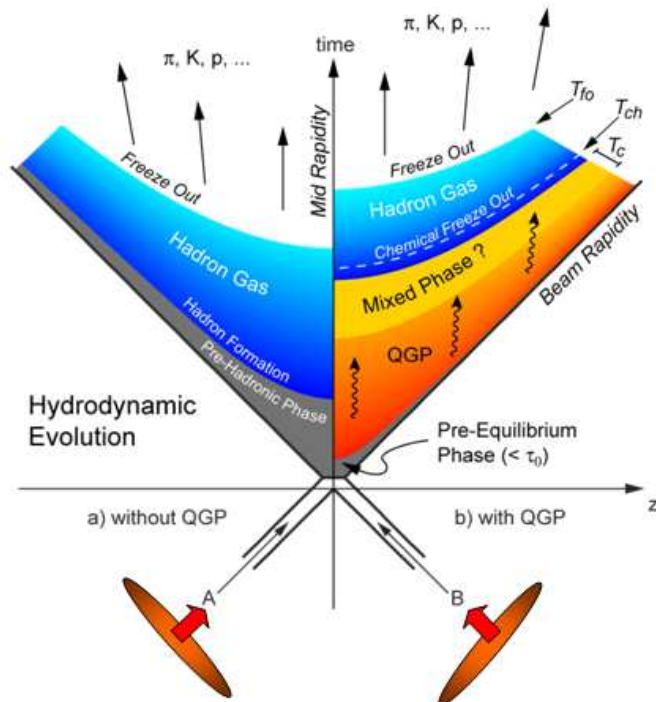


Figure 1.2: Possible scenarios for a relativistic heavy-ion collision evolution.

Chapter 2, while in this section we examine the possible scenarios for colliding heavy nuclei.

Figure 1.2 shows a space-time diagram for the collision of two ions. The nuclei travel at a speed of  $0.99c$ , and thus are Lorentz-contracted. In the figure the nuclei are represented by orange pancake-like ellipses. As these “pancakes” collide, the most energetic interactions form the earliest probes: quarkonia (pairs of heavy quarks and anti-quarks) are thought to be created, as well as “jets,” a result of large momentum transfer hard scattering processes that produce high energy partons liberated from their respective nucleons. In vacuum, these partons fragment into hadrons, produced in a signature tight cone. Jets and heavy quarks make especially valuable probes of matter created, since they are produced before the formation of the medium. As

they traverse the medium, possible modifications to the jet and heavy quark yields and spectra may occur. When detected after the collision, they can offer significant insight into the nature of the medium. This can be done by comparing unmodified (in-vacuum) jet and quarkonia yields and spectra to those which have passed through the medium.

After the initial collision phase, thought to last less than a  $fm/c$ , two scenarios are possible. In the first scenario we would observe formation of a hadron (mostly pion) gas. This scenario could almost be likened to a superposition of many binary collisions of nucleons, such as  $p + p$ . The formation of hadrons would be followed by kinetic freeze-out, which fixes the shape of particle momentum spectra.

In the other scenario the initial stage would be followed by an equilibrated plasma state, gradually becoming a mixed phase of partons and hadrons as the plasma cools. Once the mixed phase is over and chemical freeze-out<sup>1</sup> of the resultant particles occurs, the fireball becomes a hadron gas, also followed by kinetic freeze-out, as in the former scenario.

A way to distinguish between the two scenarios will be presented in the following section.

## 1.1 Strangeness production as a QGP signature

Before the first relativistic heavy ion collisions ever took place, the theoretical framework for establishing the type of matter to be created was set in place. The main focus of this section will be the predictions relevant to the production of strangeness in heavy ion collisions, however other predictions that involve observables created during the early stages of a heavy ion collision will be discussed as well.

### 1.1.1 Strangeness enhancement in the QGP

The basic argument for strangeness enhancement in the QGP is that it is energetically favorable to produce strange particles on a partonic level rather than in a hadron gas.

---

<sup>1</sup>After chemical freeze-out occurs, particle abundances have already been established, and thus the number of particles of a given species will no longer change

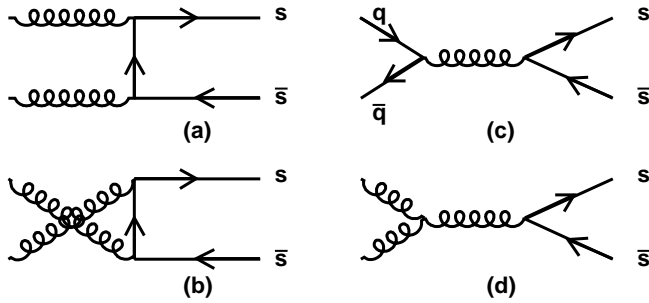


Figure 1.3: The Feynman diagrams of  $s\bar{s}$  pair production.

In a medium with partonic degrees of freedom, the strange particles can be produced via gluon fusion, or (with a smaller cross-section) via fusion of a light quark-anti-quark pair, as shown in Figure 1.3. Thus the threshold for the production of an  $s\bar{s}$  pair is given by the parton pair’s mass [5]:

$$Q_{qgp} = 2m_s \approx 200 \text{ MeV} \quad (1.3)$$

On the other hand, in a hadron gas the formation of strange particles occurs via  $NN \rightarrow N\Lambda K$  processes, and the threshold energy for producing strange particles is given by [5]

$$Q_{hg} = m_\Lambda + m_K - m_N \approx 670 \text{ MeV} \quad (1.4)$$

However, this argument is mainly valid for interactions of a small system, not for large systems where particles can re-interact following the initial binary scattering. An enhancement in strange particle abundances is seen where QGP was not expected to be produced: at AGS (top  $\sqrt{s_{NN}} = 5 \text{ GeV}$ ) and SPS ( $\sqrt{s_{NN}} = 17 \text{ GeV}$ ) energies. To understand this enhancement, we must turn to the description of the interacting systems from the point of view of statistical mechanics.

In  $p + p$  collisions the baryon quantum number has to be conserved locally, so the system can be described in terms of a canonical ensemble, with only two parameters,  $\beta$  (the inverse slope parameter equal to  $1/T$ , where  $T$  is “temperature”), and  $\gamma$ , the “chemical fugacity.” For a large system, we can introduce potentials (for example, the

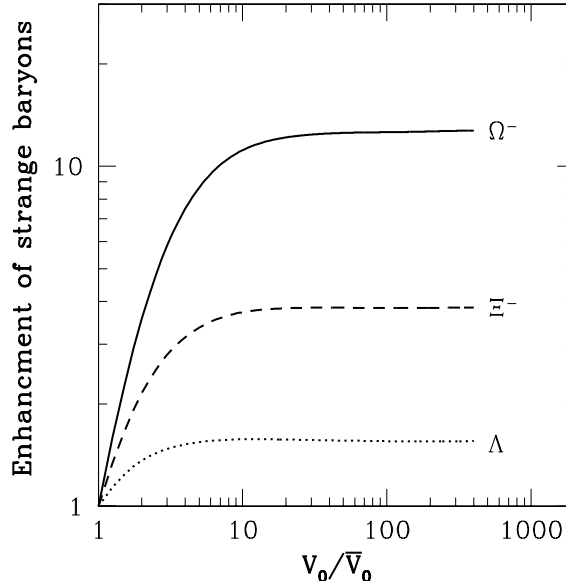


Figure 1.4: Volume dependence of strange baryon densities normalized to their value calculated at  $V_0 = \bar{V}_0 = 7.4 \text{ fm}^3$  for temperature  $T = 168 \text{ MeV}$  and chemical potential  $\mu = 266 \text{ MeV}$ . The volume parameter scales with the number of participants. From [6].

non-zero baryon density can be expressed through the baryo-chemical potential ( $\mu_b$ ) and describe the system using the grand-canonical ensemble [7, 8]. If a system can be described via a grand-canonical ensemble, local conservation of baryon quantum number is no longer required. An  $\Omega^-$  ( $sss$ ) baryon does not have to be formed next to an  $\bar{\Omega}^+$  ( $\bar{s}\bar{s}\bar{s}$ ) baryon. Instead, the  $\bar{s}$  quarks that remain from the  $s\bar{s}$  pair production, can be used to form kaons. Thus the strangeness enhancement, to quote Reinhard Stock, is “the fading away of small volume canonical constraints, in the terminology of the statistical model” [8]. This is illustrated in Figure 1.4. The figure shows a calculation of strange baryon abundances using the grand-canonical partition function normalized to the volume of the system described by the canonical ensemble [5]. As the size of the system grows, so does the number of produced strange baryons. The greater the strangeness content of the baryon, the higher is the “enhancement,” or, conversely, the more its production channel was suppressed in a canonical ( $p + p$ ) system.

By itself, the removal of this canonical suppression does not signal the creation of the quark-gluon plasma. However, reaching the apparent saturation limit indicates a

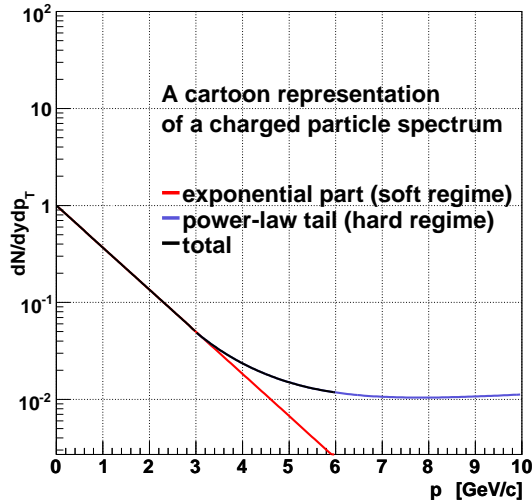


Figure 1.5: A cartoon representation of a charged particle spectrum. Below (above)  $p_T = 3$  GeV/c the exponential (power law) component dominates.

regime where QGP would be possible.

### 1.1.2 Suppression of the high momentum spectra

One known particle production mechanism in elementary collisions is by hard scattering, and via parton fragmentation into hadrons. In elementary collisions, the cross sections are calculable using perturbative QCD (pQCD) methods [9].

The energy carried by the jet depends on the fraction of incident hadron momentum ( $x_{Bjorkien} = \frac{p_{parton}}{p_{hadron}}$ , or  $x$ ) carried by the parton that fragments into the jet. The parton distribution functions (PDFs) are determined by scattering particle beams at various energies on hadron targets. Then, by measuring the total energy of the jet products one can determine the highest probability jet type: at RHIC energies gluon jets are dominant at  $p_T^{jet} < 5$  GeV/c; quark-gluon scattering creates jets for  $5 < p_T^{jet} < 30$  GeV/c; qq scattering is the most likely progenitor of jets with  $p_T > 30$  GeV/c [10].

There is much more information about particle production to be mined from the spectra of particles produced in collisions, whether produced in jet fragmentation or some other mechanism. At low  $p_T$ ,  $1 < p_T < 4$  GeV/c (the cut-off depends on the

particle), particle production is dominated by soft processes and can be described by an exponential function. At higher  $p_T$ , where fragmentation processes take over, the spectrum is best described by a power law [11], as illustrated in Figure 1.5. The shape of the spectrum reveals the on-set of the fragmentation (jet) regime, whether the spectrum is produced in elementary or heavy-ion collisions.

### The nuclear modification factor

A way to learn about particle production mechanisms in nuclear matter is to compare particle spectra measured in Au+Au collisions to those obtained from the data where a QGP is not expected, such as  $p + p$  and  $d + Au$  collisions. Do particle production mechanisms in Au+Au exhibit the properties of  $p + p$  collisions, scaled to reflect the geometry of projectiles with 197 times the number of nucleons? What, if any, are the ways in which particle spectra are modified by the medium? We use the nuclear modification factor,  $R_{AA}$ , to measure the medium effect on high  $p_T$  particle production. The nuclear modification factor is defined as follows (Eq. 1.5):

$$R_{AA}(p_T) = \frac{d^2 N^{AA}/dp_T d\eta}{\langle N_{bincoll} \rangle / \sigma_{pp} \cdot d^2 \sigma^{pp}/dp_T d\eta} \quad (1.5)$$

Here the numerator ( $d^2 N^{AA}/dp_T d\eta$ ) contains the A+A (Au+Au in this case) yield in a given  $p_T$  bin, and the denominator,  $\langle N_{bincoll} \rangle / \sigma_{pp} \cdot d^2 \sigma^{pp}/dp_T d\eta$ , contains a coefficient from the Glauber calculation [10], that scales the  $p + p$  yield,  $d^2 \sigma^{pp}/dp_T d\eta$ , by the number of binary collisions in the Au+Au data at a given centrality.

The  $R_{AA}$  ratio is sometimes referred to as the  $R_{AB}$  ratio when different species are involved in a collision. This is the case for deuteron on gold ( $d+Au$ ) collisions, which were measured in the 2003 RHIC run. These data are essential in understanding the effects of the medium on the particle spectra (final state effects) and on the energy loss in Au+Au collisions.

Figure 1.6a shows both the  $R_{AA}$  measurement for the most central Au+Au collisions (blue stars) and two separate  $R_{AB}$  measurements for  $d+Au$  data. The red circles represent the data taken in the top 20% most violent  $d+Au$  collisions (by most violent here we mean with most detected particles produced), while the green triangles

show the  $R_{AB}$  from the minimum bias  $d$ +Au collisions. The lines show uncertainties in measurement due to normalization. The dashed line at  $R_{AB} = 1$  guides the eye to the ratio expected if  $d$ +Au or Au+Au collisions were only a superposition of the appropriate number of  $p + p$  collisions.

There are two important features of this figure: first, we see that the Au+Au charged particle spectrum is significantly suppressed beyond 2.5 GeV/c. Models that include energy loss only via hadronic interactions cannot account for the suppression observed in Au+Au [12, 13, 14], as seen in Figure 1.7b. However, if partonic energy loss is included (energy loss via gluon radiation in the medium), the suppression can be explained [14, 15, 16, 17]. On the other hand the  $R_{AB}$  for  $d$ +Au data is not suppressed, and the function can be understood by introducing hadronic energy loss only [13], as seen in Figure 1.7b. In Figure 1.7 we see two theoretical calculations. One calculation (the blue shaded band) includes an initial state parton multiple scattering that results in the enhancement of the high- $p_T$  particle spectrum, which is called the Cronin effect [18]. This phenomenological effect is thought to be the mechanism behind the initial enhancement of the charged particle spectra in the  $p_T$  region between 1.5 and 2.5 GeV/c. In most models, it is usually added as a random Gaussian transverse boost to the projectile partons before hadronization [17]. The calculation without Cronin is plotted in magenta. As evident from Figure 1.7a, the Cronin effect must be included in calculations to correctly model a system with non-partonic degrees of freedom. Because it is an initial state effect, i.e., the re-scattering takes place before medium formation, it must be included in calculations describing most central Au+Au collisions as well.

### The $R_{CP}$ ratio

Calculating the  $R_{AA}$  requires determination of particle spectra in two different data sets, using two distinct data analysis methods. This introduces additional systematic error. Another way to measure the modification of the spectrum due to the presence of a medium is to calculate the so-called  $R_{CP}$  ratio, given in Eq. 1.6. In the denominator, instead of the  $p + p$  charged particle spectrum, the spectrum from peripheral (in this case 60-80% peripheral) Au+Au events is used. Both the numerator and the

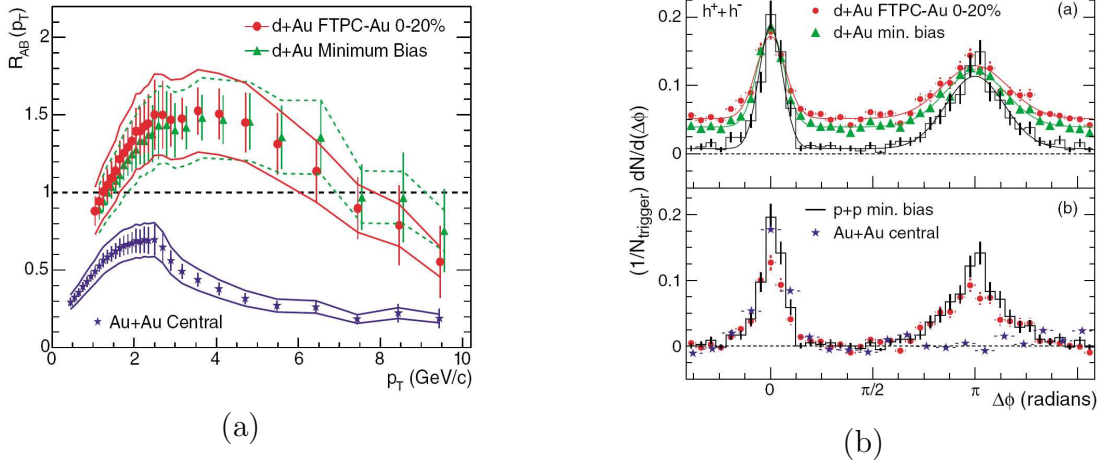


Figure 1.6: Evidence of energy loss due to the dense medium in central Au+Au collisions. (a)  $R_{AA}$ , the nuclear modification factor measured in the most central Au+Au (purple stars), minimum bias  $d$ +Au (green triangles), and 0-20% central  $d$ +Au (red circles) collisions at  $\sqrt{s_{NN}} = 200$  GeV. (b) Suppression of the away-side jet in the most central Au+Au collisions (blue stars), and no evidence for such suppression in minimum bias and 0-20% central  $d$ +Au events [14].

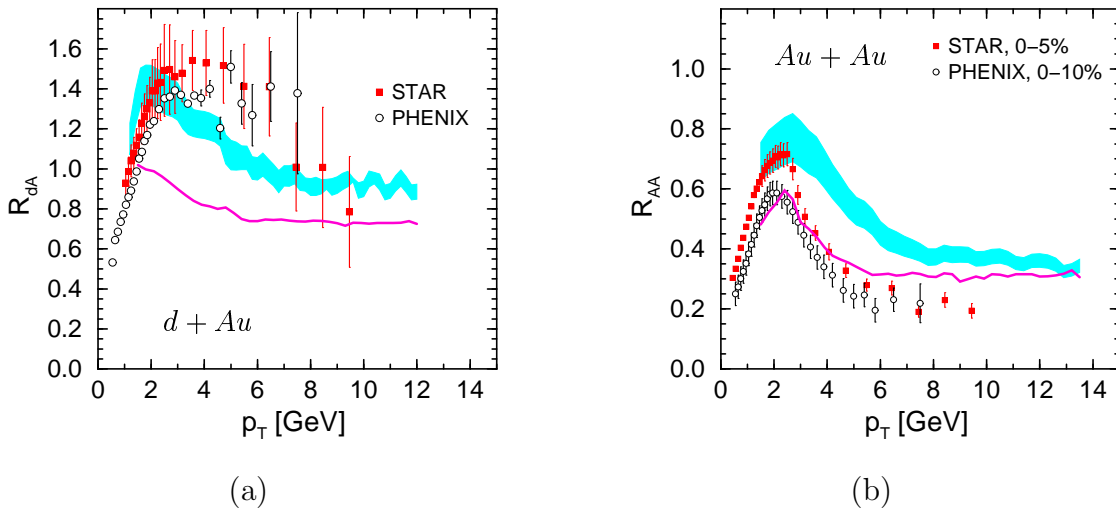


Figure 1.7: Theoretical calculations for  $R_{AA}$  which only include hadronic energy loss are represented by the blue band. The solid magenta line represents calculations with null Cronin effect. (a)  $d$ +Au data at  $\sqrt{s_{NN}} = 200$  GeV and (b) Au+Au data at  $\sqrt{s_{NN}} = 200$  GeV [13].

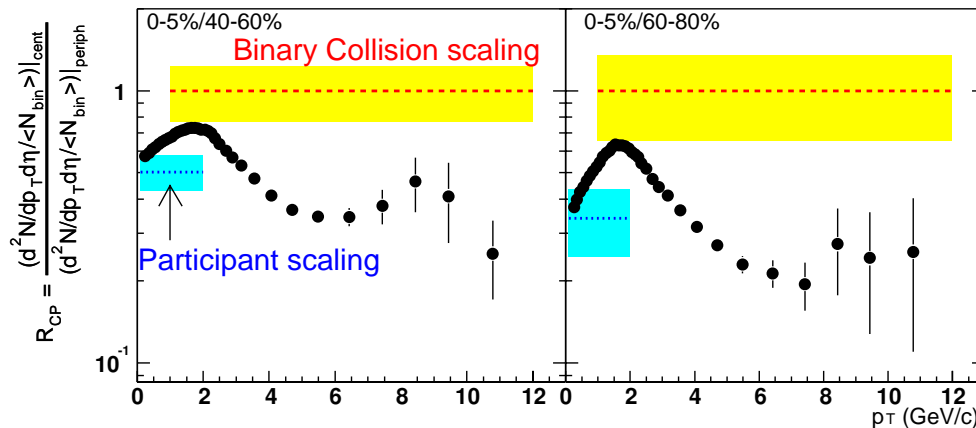


Figure 1.8: The  $R_{CP}$  as a function of  $p_T$  for  $(h^+ + h^-)/2$ . The panel on the left, normalized to 40-60% centrality Au+Au collisions, exhibits less suppression than the panel on the right, normalized to the 60-80% centrality data. Adopted from [17].

denominator are normalized by the number of binary collisions in each (given by the  $\langle T_{AA} \rangle$  Glauber coefficients). The correlated systematic errors cancel, and, moreover, this ratio is useful for particle species that have a limited spectrum measured in  $p+p$ .

$$R_{CP}(p_T) = \frac{\langle T_{AA} \rangle^{60-80\%} d^2 N^{AA} / dp_T d\eta}{\langle T_{AA} \rangle^{0-5\%} d^2 N^{AA} / dp_T d\eta} \quad (1.6)$$

The  $R_{CP}$  ratio calculated using two peripheral Au+Au centralities, 40-60% and 60-80% central, is shown in Figure 1.8. Both panels of the figure exhibit the pertinent features similar to those observed in  $R_{AA}$ : a strong suppression of the high  $p_T$  tail that can only be described by in-medium energy loss. However, because the Cronin rescattering is present in the peripheral collisions as well, the enhancement in the lower  $p_T$  part of the spectrum is less pronounced. The spectrum suppression is stronger in the right panel, where the more peripheral collisions are used as a reference. The high  $p_T$  suppression in this panel is on a par with that observed in  $p+p$ .

### Back-to-back jets

A more direct way to learn about jet production in Au+Au collisions is to study the azimuthal correlation functions of high  $p_T$  particles. A back-to-back jet has a characteristic double-cone shape: the particles produced via fragmentation are closely

aligned in azimuth. A back-to-back jet literally resembles two jets moving  $180^\circ$  in azimuth opposite one another. A jet can be characterized by its leading particle: the hadron that takes the most momentum from the fragmenting parton. Despite its characteristic shape, the jet cone is difficult to discern among hundreds of particles created during a heavy ion collision. Nevertheless, we can study the jets statistically over a large event sample. This is done by selecting leading particles in a certain  $p_T$  range, finding associated hadrons (by definition, the  $p_T$  of these particles must be less than that of the leading hadron), and calculating the difference in azimuthal angle between the two. Uncorrelated pairs would form a flat background, while pairs of particles that come from a jet would form a gaussian distribution around  $0^\circ$  (those on the same side with the leading particle) and  $180^\circ$  (on the side opposite to the leading particle).

At RHIC this has been done with unidentified charged particles in three collision systems:  $p + p$ ,  $d+\text{Au}$ , and  $\text{Au}+\text{Au}$ . The result is shown in Figure 1.6b. The top plot shows the correlation function obtained in  $d+\text{Au}$  collisions at  $\sqrt{s_{NN}} = 200$  GeV. As before, the red circles represent the data from the top 20% most violent  $d+\text{Au}$  collisions, while the green triangles show the data from all  $d+\text{Au}$  collisions. The black histogram, showing the shape of the correlation function in  $p + p$  collisions, is plotted for reference. The bottom panel shows the correlation function in the most central  $\text{Au}+\text{Au}$  collisions. Again the black histogram is the correlation function obtained in  $p + p$  collisions. The red circles again represent central  $d+\text{Au}$  data.

The message of the figure is simple and beautiful. Both sides of the jet are present (on the same-side of the leading particle and on the away-side) in the  $d+\text{Au}$  and  $p + p$  data. The away-side of the back-to-back jet is absent in the most central  $\text{Au}+\text{Au}$  data. Therefore, the away-side is suppressed by the medium.

This observed disappearance of the away-side jet tells us about the state of the medium (the suppression is very large, the medium must be very dense), but does not tell us about what happened to the suppressed hadrons, or how the hadrons that survived on the same side were produced. Further studies, especially with identified hadrons are needed to further our understanding of jet production and medium suppression. The disappearance of the away-side jet is only the foundation on which

more detailed studies, such as a study of multi-strange baryon correlations is based.

## Summary

The high  $p_T$  measurements with unidentified charged particles produced in heavy ion and  $p+p$  collisions at RHIC have made an important contribution to our understanding of the medium created in the most central Au+Au data.

Measurements of the nuclear modification factors along with the away-side suppression of the back-to-back jet have shown that the high  $p_T$  particle production is suppressed in Au+Au collisions. Moreover theoretical calculations have shown the suppression to be due to a medium that is 100 times more dense than ordinary cold nuclear matter [10]. However, this is only one piece of the QGP puzzle. Although we have a better understanding of the way high  $p_T$  hadrons behave in extreme conditions, we do not yet have a good quantitative understanding of particle formation in the intermediate  $p_T$  region, nor do we know much about the composition of the medium. Utilizing the variables described above, we can deepen our understanding of particle production by performing the analysis with larger data sets and with identified probes. This will be the topic of Sections 1.2 and 1.3, as well as the analysis that is the subject of this dissertation.

### 1.1.3 Other QGP signatures

There is no one smoking-gun signature that defines the production of a QGP, but rather a sum of effects. There are well-known predictions of behavior of heavy quarks, especially the  $c$ -quark, which is predicted to be Debye-screened from its pair  $\bar{c}$ -quark by the QGP, resulting in a  $J/\psi$  ( $c\bar{c}$ )<sup>2</sup> meson suppression. The excess  $c$ -quarks would bind to lighter quarks, producing “open charm” mesons. The yields for these can then be measured to ascertain the level of energy loss of  $c$ -quarks in the medium via  $R_{AA}$  or  $R_{CP}$ . The  $c$ -quark is thought to be so heavy that it would not be affected significantly by the medium (would not lose significant energy via gluon radiation). However, recent studies show that this is likely not the case [19, 20]. Radiative energy

---

<sup>2</sup>Also known as “hidden charm”

loss is insufficient to explain the suppression of single-electron spectrum obtained from open-charm decays [19].

Another measurement of the medium density can come from  $\gamma$ -jet coincidence measurements and direct photons, created via the  $q + \bar{q} \rightarrow \gamma + g$  (annihilation) and  $q + g \rightarrow \gamma + q$  (Compton) processes. Because  $\gamma$  rays are not affected by the strong force, they are not modified by the strongly-interacting medium. By detecting and measuring the energy of the  $\gamma$  produced via annihilation or Compton processes, we can measure the exact energy of the hard scattering. We can then use this to extract the energy loss of the away-side jet (whose parton initially had the same energy as the detected  $\gamma$ ) due to the medium. The results of this measurement are not yet available.

Yet other ways in which a QGP could manifest itself is the anomalies in the dilepton spectrum. In the QGP the dileptons would be created in a  $q + \bar{q} \rightarrow l^+ + l^-$  reaction [3]. Leptons cannot interact strongly. Thus, dilepton pairs are thought to carry information about their production conditions (the temperature of the plasma) past the final freeze-out, where they can be detected. Measuring an excess of dilepton pairs in the 1-4 GeV/ $c^2$  region of the dilepton invariant mass should indicate the temperature of the medium that produced them. The measurement is not trivial and the accuracy of the conclusions are highly dependent on the temperature of the plasma. The method seems to be valid for plasma temperatures above 300 MeV, as the QGP-formed dilepton yields will start to surpass the Drell-Yan yields in a narrow part of the dilepton spectrum. To date, there has been no conclusive anomalous measurement from RHIC in the central Au+Au collisions.

This concludes a brief outline of measurements that can be performed to study the QGP. These are, of course, non-exhaustive and are only tangential to the work presented in this dissertation. This overview is meant to show the backdrop against which the study of multi-strange baryons was done. Moreover, some of the experimental facilities described in this thesis were designed to measure some of the probes mentioned above. Thus, this section is designed to give a broader context to the analysis presented in this dissertation.

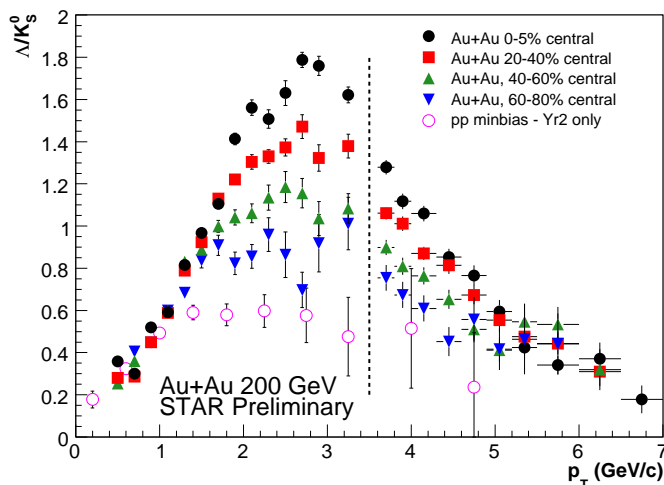


Figure 1.9:  $\Lambda/K_S^0$  ratio in four Au+Au collision centrality regions (closed symbols) and  $p+p$  collisions (open symbols). Data to the right of the dashed line were collected in 2001, to the left in 2004. All of the  $p+p$  data are from 2002 [21].

## 1.2 Strange hadron measurements at intermediate

### $p_T$

The strange quarks afford a particularly good opportunity to study particle production mechanisms. On the one hand, the  $s$ -quark mass is higher than that of the lightest,  $u$  and  $d$  quarks. On the other hand, it is significantly closer to the mass of these quarks than to the mass of the three heaviest quarks,  $c$ ,  $b$ , and  $t$ . In addition, because the  $s$  quark is not present in the constituent nucleons of the colliding nuclei, all of the strangeness observed has been produced in the collision. By using the characteristic decay topology of strange particles<sup>3</sup>, one can obtain high-purity samples of particles at higher  $p_T$  than available for lighter, non-strange hadrons.

$K_S^0$  and  $\Lambda$  spectra have been measured to  $p_T=7$  GeV/c in four Au+Au centrality bins<sup>4</sup>. Using these particle spectra, we can look at the baryon to meson ratio ( $\Lambda/K_S^0$ ) as a function of centrality. This is illustrated in Figure 1.9, where the ratio is plotted as a function of  $p_T$  for  $p+p$ , peripheral, mid-peripheral and central Au+Au collisions.

<sup>3</sup>The method is described in detail in Chapter 4

<sup>4</sup>For centrality definitions please see Appendix A

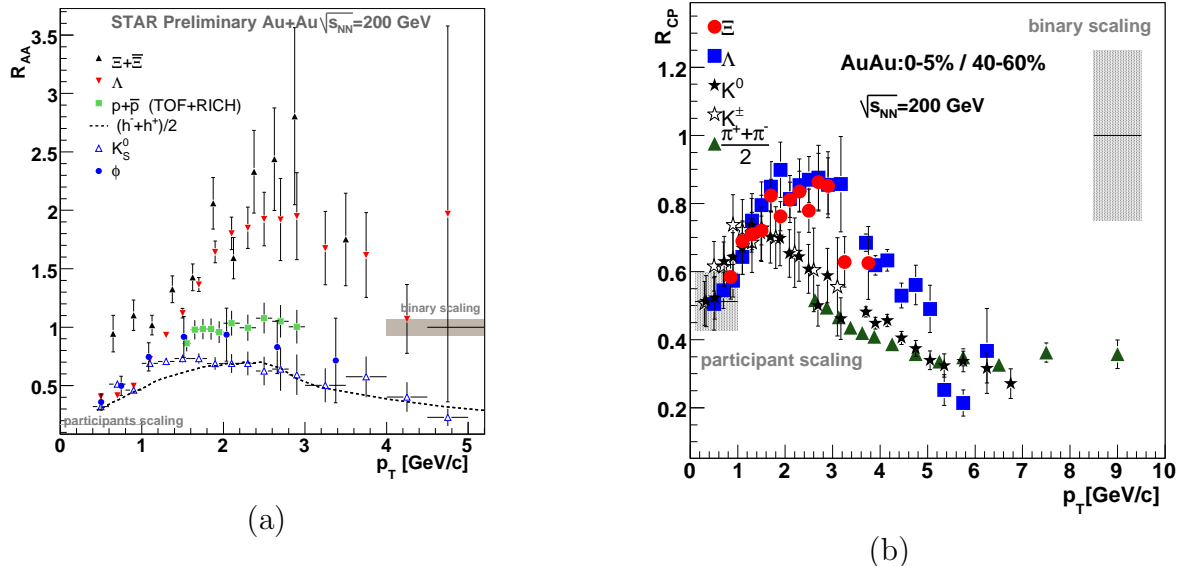


Figure 1.10: Nuclear modification factors for strange particles. (a)  $R_{AA}$ , the nuclear modification factor of strange particle spectra in 0-5% central Au+Au collisions at  $\sqrt{s_{NN}} = 200$  GeV with respect to  $p + p$  collisions at the same energy per nucleon. (b)  $R_{CP}$ , the nuclear modification factor of strange particles in 0-5% most central Au+Au collisions with respect to 40-60% Au+Au collisions at the same energy.

The most striking feature of the figure is the dominance of  $\Lambda$  baryon yields observed in the mid- $p_T$  region, between 2 and 3.5 GeV/c for non-peripheral Au+Au collisions, denoted by closed circles and squares in Figure 1.9. Moreover, baryons continue to somewhat dominate in the 40-60% central collisions, shown in Figure 1.9 as upward triangles. For a long time this dominance, which increases with centrality, was called the “baryon-meson puzzle,” as a similar behavior (but in a more limited  $p_T$  range) was observed for the  $p/\pi$  ratio [22]. However, recently we have gained more insight into understanding the origin of the enhancement. Although the model discussed below in the Theoretical framework section cannot describe the turn-over of the ratio quantitatively, it provides a qualitative understanding of the enhancement, which will be discussed below.

One important measurement performed using the strange particle spectra is the determination of the strange particle nuclear modification ratio, the  $R_{AA}$  [23]. The

initial results were surprising. Contrary to expectations of a suppression, not only were the strange particles not suppressed at intermediate  $p_T$ , the strange baryon ratio from central Au+Au collisions to those in  $p + p$  was enhanced by a factor of two, as seen in Figure 1.10a. However, when the  $R_{CP}$  of the strange particles was calculated (Figure 1.10b), it became clear that at least part of the enhancement in the  $R_{AA}$  is due to the canonical suppression of strangeness in  $p + p$  collisions. Because of the canonical suppression, the  $p + p$  collisions cannot serve as a true base-line for the nuclear modification factor for strange particles produced in Au+Au, as they “artificially” enhance the spectrum. Therefore the  $R_{CP}$ , the comparison of two sets of data with canonical suppression removed, is a better indicator of the true modification of the spectrum in the quark-gluon medium under study.

One notable feature of both the  $R_{AA}$  and the  $R_{CP}$  plots is the difference between strange mesons and baryons. Again, this can be understood within the framework of canonical suppression of strangeness. The “enhancement” – or removal of suppression – should be more pronounced for hadrons with the higher strangeness content. Thus there should be ordering of strange baryons: the smallest enhancement for  $\Lambda$ , the most enhancement for  $\Omega$  baryons. The  $p_T$  interval of the enhancement remained puzzling, as it was with the  $\Lambda^0/K_S^0$  ratio. The qualitative explanation of this “puzzle” seems to be similar.

Another variable measured at RHIC using strange particles at the intermediate  $p_T$  is a high  $p_T$  correlation function, a statistical jet measurement. The measurement uses  $\Lambda$  baryon or  $K_S^0$  meson as the leading particle to compute a correlation function in several centrality bins and over a variety of  $p_T$  ranges. Because this measurement is closely related to the subject of the present work, the results will be discussed in the concluding chapter together with the result of this author’s work. However, it is important to mention this measurement in the context of the intermediate  $p_T$  measurements. This is because the goal of the identified correlation measurement is no longer to establish the density of the medium via quantifying the suppression of the back-to-back jet, but to understand the modification of the fragmentation function of a jet that produces an  $s$ -quark. Because it is thought that the source of the correlation functions is known (jets!) the study of identified correlations introduces an additional

constraint on particle production models. The description and predictions from one such model will be presented in the next section.

### 1.3 Theoretical framework at intermediate $p_T$

When the momentum transfer is low, pQCD is not applicable, as the higher order corrections cannot be neglected in calculating cross-sections. Thus, it is important to establish in what  $p_T$  range of the spectrum the particles are produced via parton fragmentation, in order to understand to which part of the spectra the pQCD calculations *are* applicable. The bulk of particle production occurs below  $p_T < 1$  GeV/c. This is true for both baryons and mesons [24]. Also, it would appear that a meson is easier to make, and thus one would expect the meson yields to be dominant. Surprisingly, as we have seen in the previous section, there is a clear enhancement of baryon production at “intermediate”  $2 < p_T < 4$  GeV/c. Hence, it is especially important to understand particle production mechanisms in this region of the  $p_T$  spectra.

Several Recombination-Parton Coalescence models have been proposed to explain the physics governing this spectral region [25, 26, 27]. The underlying assumption for particle production in a Recombination Model is that in this “intermediate”  $p_T$  region particles are composed of a mixture of partons. Partons produced via fragmentation can “recombine” with partons produced in the medium to form a hadron. Partons produced “softly” by the fireball can coalesce into hadrons. A typical example of a recombination mechanism is illustrated in Figure 1.11. The part of the parton spectrum where the particles are most abundant, below  $p_T = 2$  GeV/c, can produce a  $p_T=4$  GeV/c meson by recombining two “soft” 2 GeV/c partons. Alternatively, the 4 GeV/c meson can be a product of a 6 GeV/c parton’s fragmentation. The same is true for a baryon, with one notable difference: a 4 GeV/c baryon would be formed by three 1.3 GeV/c partons. Because the parton spectrum is exponential, partons are much more abundant at 1.3 GeV/c (exponentially more so!) than at 2 GeV/c. Thus, it appears that when a thermal source is present, it is easier to form a 4 GeV/c baryon rather than a 4 GeV/c meson. The baryon enhancement puzzles discussed in the previous section can be qualitatively explained by simple consideration of the

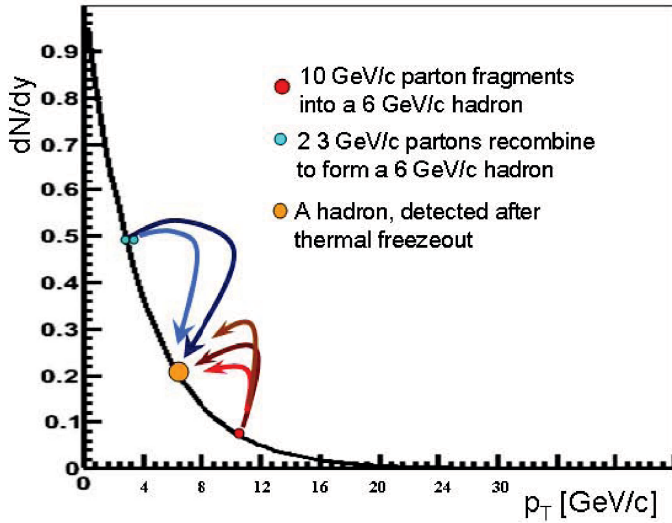
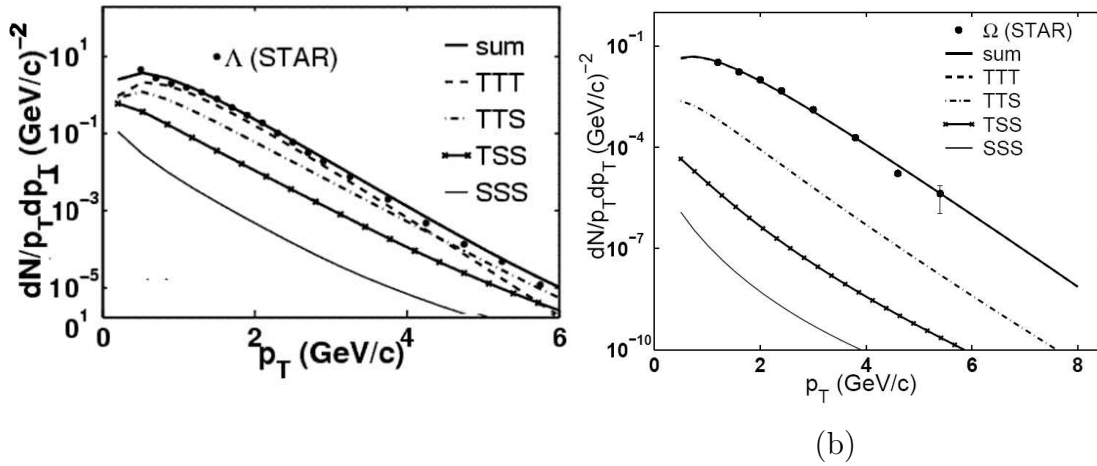


Figure 1.11: A cartoon illustrating possible particle production mechanisms. The blue arrows show two thermally produced partons recombining to form a 6 GeV/c meson. The red arrows represent a 10 GeV/c parton fragmenting to form a baryon of the same transverse momentum as the meson produced via recombination.



(a)

(b)

Figure 1.12: STAR  $\Lambda$  (a) and  $\Omega^\pm$  (b) spectra plotted on top of the University of Oregon Recombination Model spectral calculations. Dashed, dash-dotted, solid-dotted, and light solid lines represent contributions from baryons made via  $TTT$ ,  $TTS$ ,  $TSS$ , and  $SSS$  recombination respectively. See text for detail. Adapted from [28].

shape of the parton spectrum. Unfortunately, the quantitative analysis cannot yet fully describe the ratios shown in Figure 1.9 [22].

The Recombination Model from the University of Oregon calculates contributions from each of the two sources to particle spectra measured experimentally. In particular, calculations have been done for singly and multi-strange baryons. In this Recombination Model, thermal partons are referred to as  $T$ -partons, while the partons produced via fragmentation are called  $S$  (shower) partons. As a result, each baryon spectrum can be decomposed into  $TTT$  (thermal-thermal-thermal),  $TTS$  (thermal-thermal-shower),  $TSS$  (thermal-shower-shower), and  $SSS$  (shower-shower-shower) contributions.

The  $s$ -quark thermal ( $T_s$ ) and shower parton contributions ( $S_s$ ) are calculated via

$$T_s(p_1) = p_1 \frac{dN_s^{th}}{dp_1} = C_s p_1 e^{-p_1/T_s} \quad (1.7)$$

$$S_s(p_2) = \xi \sum_i \int_{k_0}^{\infty} dk k f_i(k) S_i^s(p_2/k) \quad (1.8)$$

where  $C_s$  and  $T_s$  are parameters, and  $S_i$  and  $S_i^s$  are determined from meson fragmentation functions [28].

The result of these calculations is impressive. Figure 1.12 presents the  $\Lambda$  and  $\Omega$  spectra published by the STAR Collaboration. The same figures feature spectra components, as well as the total spectrum obtained, using the University of Oregon Recombination Model. While one can clearly distinguish all four constituent recombination components for the  $\Lambda$  ( $uds$ ) spectrum, the  $TTT$  component of the  $\Omega$  ( $sss$ ) baryon spectrum is indistinguishable from (or identical to) the total. This result has led to a prediction of no jet-like correlation expected for  $\Omega$  baryons in the most central Au+Au collisions for  $p_T^\Omega < 8$  GeV/c.

The argument leading to this prediction is as follows. The strangeness production cross-section in a dense, hot medium is greatly increased, at least in the intermediate  $p_T$  region. However, the increase is entirely due to the thermalized medium. Thus, the fragmentation component (produced by the initial binary collisions) is swamped by the thermal component in this  $p_T$  region. This effect would be much more pronounced for  $s$ -quarks than for light quarks. This is because the  $s$ -quark mass introduces a higher jet energy threshold than the jets made of  $u$  and  $d$  quarks. If an  $\Omega$  correlation

exists, it should be compared to a correlation function of a baryon not made entirely of strange quarks ( $\Lambda$ ). If the  $\Omega$  signal is significantly suppressed with respect to the  $\Lambda$  signal, it would validate calculations published in [28]. If the signal exists and is comparable to that of  $\Lambda$ , the underlying basis for the calculation would need to be revised.

This verifiable prediction has been the main motivation for this dissertation.

## 1.4 Thesis outline

For this work, correlation functions between charged particles and multi-strange baryons were measured in three data sets: Au+Au,  $d$ +Au, and  $p + p$ , all at energies of  $\sqrt{s_{NN}} = 200$  GeV/ $c$ .

First, I will introduce the facilities used for data collection, then I will describe the methods and techniques used for obtaining the baryon and charged particle spectra and correlations. Simulations and preparatory procedures will also be described along with applied corrections and methods used to obtain these. Finally, I will present the results of my study and will put these in context of the Recombination Model and other experimental observations. The implications of the measurement to our understanding of the matter produced at RHIC will be discussed.

# Chapter 2

## Experimental Setup

### 2.1 RHIC

The data used for this thesis were obtained at a state of the art accelerator-collider complex, the Relativistic Heavy Ion Collider (RHIC), located at Brookhaven National Laboratory in Upton, NY. RHIC has been in operation since the summer of 2000. It spans 1.2 km in diameter, and was designed to run gold on gold (Au+Au) collisions with up to  $2 \times 10^{26} \text{ cm}^{-2}\text{s}^{-1}$  in luminosity. Since the beginning of operations the RHIC accelerator has surpassed the design luminosity by 100% [29].

A remarkable achievement in the field of high energy nuclear physics, RHIC was the first machine built with capability to collide mixed species. As designed, RHIC can collide ion species as light as protons and deuterons and (provided there is a suitable source) as heavy as uranium at a variety of energies. For Au-ion collisions the Au ion energies range from 9 to 100 GeV/nucleon, while for the proton-proton collisions the particle energy can go as high as 250 GeV [30]. Last, but not least, RHIC is designed to support an impressive polarized proton-proton spin program designed to determine gluon contributions to the proton spin, and requiring the collider to be equipped with Siberian Snakes and Spin Rotators [31] for this operation.

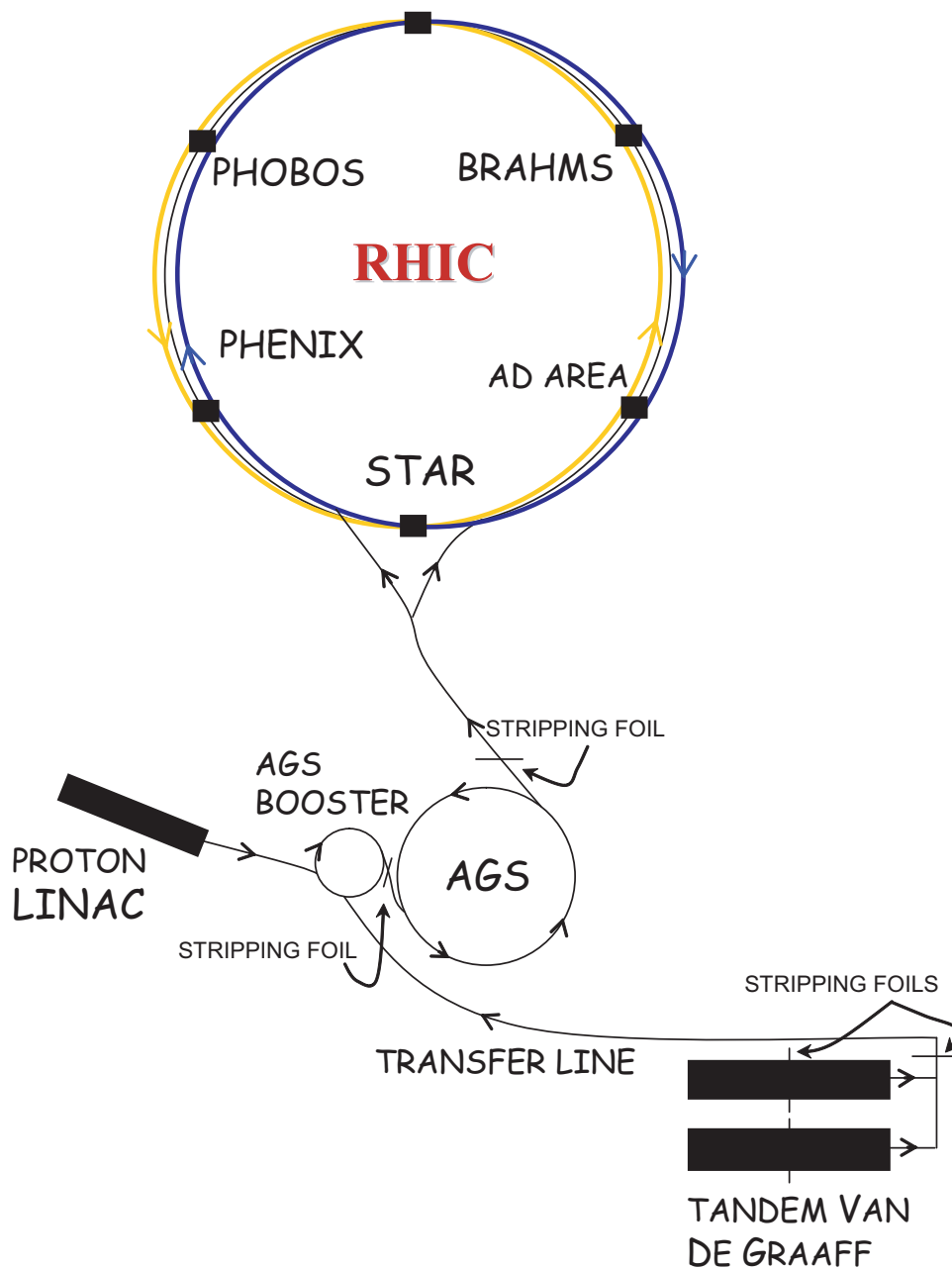


Figure 2.1: RHIC accelerator-collider complex. The ions are initially accelerated in the Van de Graaff tandem accelerators, pass the stripping foils and are injected into the transfer line. From there they pass into the Booster, are ionized further, enter the AGS, accelerated yet again, stripped of their final electrons as they exit the AGS and are steered into RHIC. The protons originate at the LINAC, and are accelerated from there in a manner similar to that of heavy ions.

### 2.1.1 Mechanics of particle acceleration

RHIC consists of two independent accelerator-storage rings with six interaction points and a system of superconducting magnets. Accelerating heavy ions is a complex process that unfolds in stages. Since RHIC uses superconductivity (most of the RHIC components operate at 4.2 K [32]), the RHIC ramp rate is relatively slow [30]. It takes a week to cool RHIC superconducting magnets from room to operating temperature. Moreover, the accelerator is not a stand-alone machine, it is part of a complex that includes other components – ion sources and initial accelerators (LINear ACcelerator (LINAC) for protons and Tandem Van de Graaff accelerators for heavier ions), electron-stripping foils, a Booster ring, and the Alternating Gradient Synchrotron (AGS). Before reaching RHIC, the atoms are ionized and pre-accelerated. A description of RHIC operation using Au atoms as an example follows:

The negatively charged ( $Q=-1$ )  $\text{Au}^{197}$  ions are produced in a source and accelerated into and through the Tandem Van de Graaff accelerator, which has a terminal voltage of +14MV. At the terminal the ions pass through stripping foils, losing their negative charge and acquiring a positive charge  $Q_T$ , which for gold ions is +12 units. The ions are accelerated from the terminal to ground potential, increasing their energy by 168 MeV (at this point the energy of each Au ion is about 1 MeV per nucleon). As the ions exit the Van de Graaff, they are stripped further and pass into the Booster via a transfer line. In the Booster the ions are bunched into six bunches, accelerated further, and, as they exit the Booster, stripped of all except the K-shell electrons. After this, the Alternating Gradient Synchrotron (AGS) receives the bunches from the Booster, re-bunches the ions (each AGS bunch is equivalent to six Booster bunches), accelerates, and transports them to RHIC with energy of 8.86 GeV per nucleon. Before entering RHIC, however, the ions are stripped of the remaining electrons. The bunches can then be stored and further accelerated in RHIC. A second Tandem Van de Graaff accelerator is available to provide a second species for asymmetrical collisions.

For the injection of protons the proton Linear Accelerator (LINAC) is used. For the polarized proton program, the challenge is to keep the beam polarized through out the acceleration process. To maintain the desired polarization, two polarimeters

and one partial siberian snake are installed en route to RHIC. From their source in the LINAC, the protons are fed into the Booster, then into the AGS. From there, at 25 GeV per particle, the beam is transferred to RHIC. Both the ion and proton injection processes are illustrated in Figure 2.1. At the end of the heavy ion injection, each RHIC ring holds a total of  $6 \times 10^{10}$  particles. When injected with light ions, this number may be up to two orders of magnitude larger [30].

Once inside RHIC, beams travel inside two rings in opposite directions. One ring is called “blue” for reference, in it the beam travels in the clockwise direction as viewed from above. The other ring is often referred to as the “yellow” ring. There the beam moves in the counter-clockwise direction.

### 2.1.2 Interaction areas

There are six interaction regions along the RHIC perimeter. Four of these are used by experiments, the fifth is used by the collider-accelerator department for beam tests and operations, and the sixth is unoccupied. The four experiments at RHIC are the larger Solenoidal Tracker At RHIC (STAR) and Pioneering High Energy Nuclear Interaction eXperiment (PHENIX), and the smaller PHOBOS and Broad RAnge Hadron Magnetic Spectrometer (BRAHMS). The STAR detector will be described in detail below, while here it is worth mentioning the main features of the other detectors that participate in the RHIC heavy ion program.

#### PHENIX

PHENIX is a detector specifically designed to measure electromagnetic probes, i.e., electrons, muons, and photons, all measured by fast detectors that are capable of observing hundreds of heavy ion events per second. The physics goal of the PHENIX heavy ion program is to study the formation of the QGP by measuring rare probes. The rate of PHENIX data-taking is high (10 kHz [33]), since it was hoped that a high-statistics measurement will include a sufficient fraction of rare processes. PHENIX consists of two large central arms, positioned symmetrically on opposite sides of the

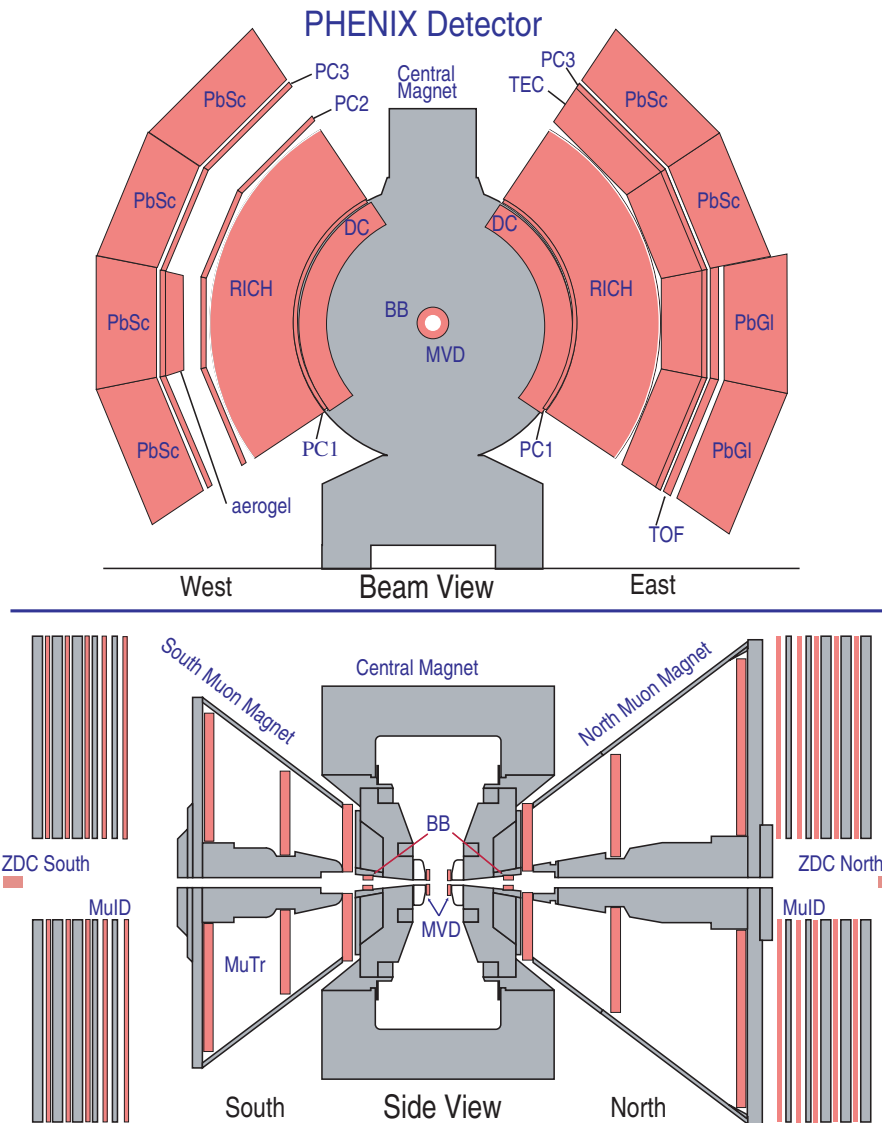


Figure 2.2: A beam (top figure) and side view (bottom figure) of the PHENIX detector.

beam line at three and nine o'clock respectively. The central arms cover the mid-rapidity region and subtend a total of  $180^\circ$  in azimuth, each arm covering  $90^\circ$ , as

seen in the top part of Figure 2.2. As seen in the bottom part of the same figure, in addition to central arms, there are two muon forward spectrometers, covering  $1.1 < |\eta| < 2.2$ . PHENIX is well equipped with two types of high-granularity electromagnetic calorimeters, denoted as PbSc (lead-silicon) and PbGl (lead-glass) in Figure 2.2. These are used for reconstructing  $\pi^0$  and  $\eta$  mesons. In the central arms particle identification is performed using the Ring Imaging CHerenkov (RICH) ( $e^\pm$ ,  $\pi$  up to  $p_T=4$  GeV/c) and the Time of Flight (TOF) ( $\pi^\pm$ ,  $K^\pm$  up to  $p_T=1.5$  GeV/c,  $p^\pm$  up to 3.5 GeV/c) detectors. The forward arms are equipped with muon spectrometers, which consist of a muon tracker (several planes of drift chambers) and a muon identifier (steel absorber layers interlaced with streamer tubes of Iarocci type). The primary function of the muon arms is identification of  $J/\psi$  via its  $J/\psi \rightarrow \mu^- \mu^+$  decay channel.

## PHOBOS

From its inception, the main goal of PHOBOS was to measure everything possible in an inelastic collision in order to detect “special events” – events where QGP may have been formed. Also, the experiment was designed to measure particles with as small  $p_T$  as possible, down to 10 MeV/c. This was done in order to analyze the entire particle-production phase space and to measure collective phenomenon, believed to be better pronounced in the low  $p_T$  region of the particle spectrum. As a result, the detector is equipped with fast silicon pad detectors and a TOF detector. Main triggering is provided by paddle counters (each made up of 16 scintillator detectors located around the beam pipe at  $3.2 < \eta < 4.5$ ) and the Zero Degree Calorimeters (ZDCs). PHOBOS ZDCs are identical to those of STAR, and are described in the STAR triggering detectors section below.

The PHOBOS pseudorapidity coverage is a patchwork of Silicon detectors that extends to 5.4 units in both direction, as shown in Figure 2.3. The Ring detector covers the  $3.2 < |\eta| < 5.4$  region, the Octagon detector has a limited  $\phi$  coverage, but an extensive coverage in pseudo-rapidity  $|\eta| < 3.2$ , while the Inner Vertex detectors cover only about  $45^\circ$  each in  $\phi$ , and  $|\eta| < 1.5$ , seen in Figure 2.3. Particle ( $\pi$ ,  $K$ ,  $p$ ) identification is performed by using the energy loss of the charged tracks as

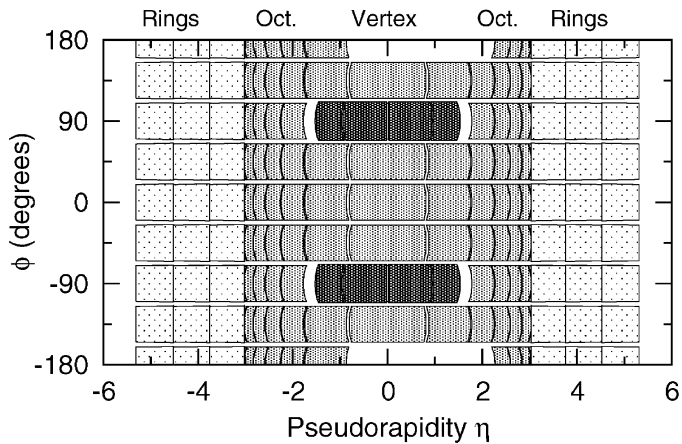


Figure 2.3: The geometrical acceptances of the PHOBOS Silicon detectors. The Ring detector (light), the Octagon (medium) and the Inner Vertex detector (black) [34].

they traverse the silicon detectors in a double-dipole magnetic field. The particle ID information is supplemented by the TOF detectors, which extend the momentum identification capabilities to a higher  $p_T$  region.

The PHOBOS Collaboration has successfully carried out measurements of particle multiplicities, particle/anti-particle ratios, and collective flow [34]. At present, the PHOBOS experiment has completed operation.

## BRAHMS

The BRAHMS experiment is designed to measure particle spectra over a large pseudorapidity range, and can perform limited particle identification ( $p^\pm$ ,  $K^\pm$ ,  $\pi^\pm$ ). BRAHMS has two separate movable spectrometer arms for high and low transverse momentum particles, and is best suited for measuring transverse momentum and rapidity distributions. Its physics goals focus on investigating stopping, particle ratios, and the chemical equilibration of events [35].

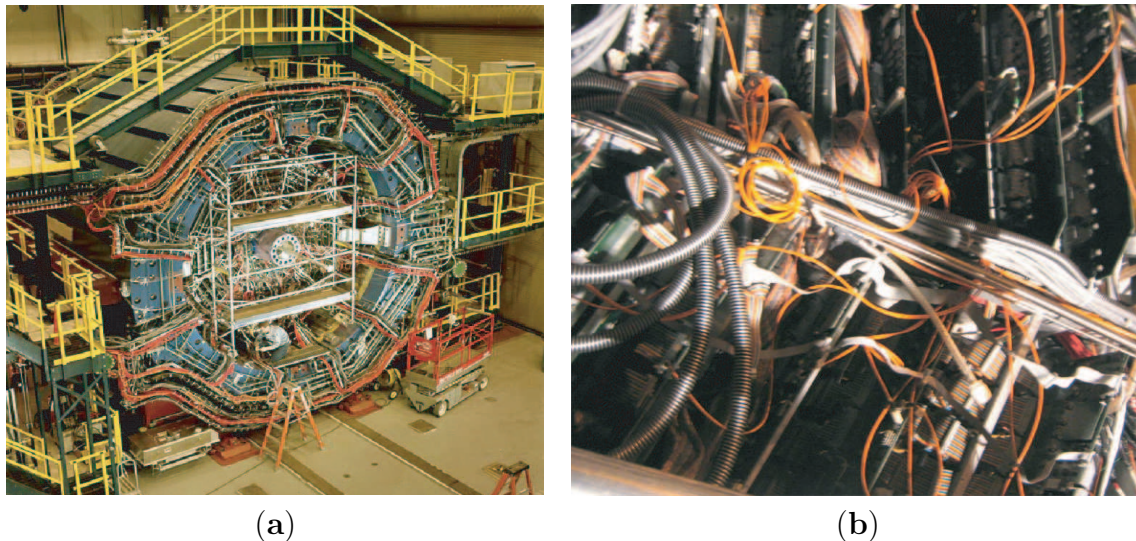


Figure 2.4: Photographs of STAR: (a) The STAR detector with one of its endcaps removed. The large blue structure visible under the utility wires is the STAR magnet outer ring. The TPC endcap is just inside the blue ring. There is aluminum scaffolding in front of the TPC face that is not part of the detector. (b) A close-up of TPC read-out boards and cabling.

## 2.2 STAR

The STAR detector was built to measure a variety of probes, but primarily to look for QGP signatures, available through measuring hadrons. Thus, it is a large acceptance detector, with a variety of tools available to investigate a new state of matter formed at RHIC. STAR's most powerful tool is the Time Projection Chamber (TPC), which covers  $360^\circ$  in azimuth, and  $|\eta| < 1.5$ . The TPC tracks charged particles moving through its volume, and thus enables the topological reconstruction of  $K_S^0$ ,  $K^\pm$ ,  $\Lambda^0$ , and the  $\Xi$  and  $\Omega$  baryons via their charged decay products. This has made possible a variety of unique analyses using strange particles. For reference, a photograph of the STAR detector is shown in Figure 2.4a and a close-up of a TPC read-out board in Figure 2.4b.

In 2000, when RHIC was turned on, STAR consisted of its large acceptance Time Projection Chamber (TPC), two Zero Degree Calorimeters (ZDCs) and the Central Trigger Barrel (CTB), shown in Figure 2.5. As time progressed, new detectors were

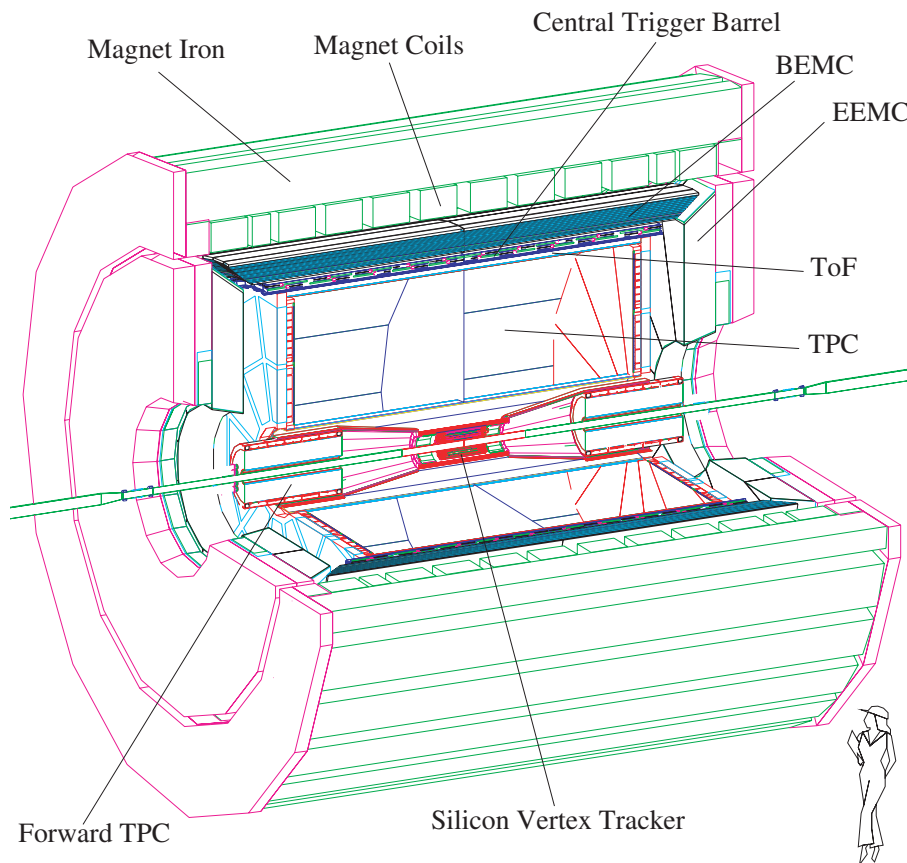


Figure 2.5: A schematic representation of the STAR detector.

added. In 2001, for the first  $p+p$  run, STAR added two Beam-Beam Counters (BBCs) (not shown in Figure 2.5) and a prototype Time Of Flight (TOF) detector. The 2003 run included the Silicon Vertex Tracker (SVT), and an additional silicon tracking layer called the Silicon Strip Detector (SSD) (not shown), a fraction of the Barrel Electromagnetic Calorimeter (BEMC), and two Forward Time Projection Chambers (FTPCs), also shown in Figure 2.5. By 2005 the half of the BEMC was installed, as well as the EMC endcap (EEMC), and two Photon Multiplicity Detectors (PMDs), not shown in Figure 2.5. Because of these additions, the STAR detector is competitive with PHENIX in ability to investigate open and hidden charm and quarkonia. In addition, there has been a measurement of the neutral pion spectrum, while a direct

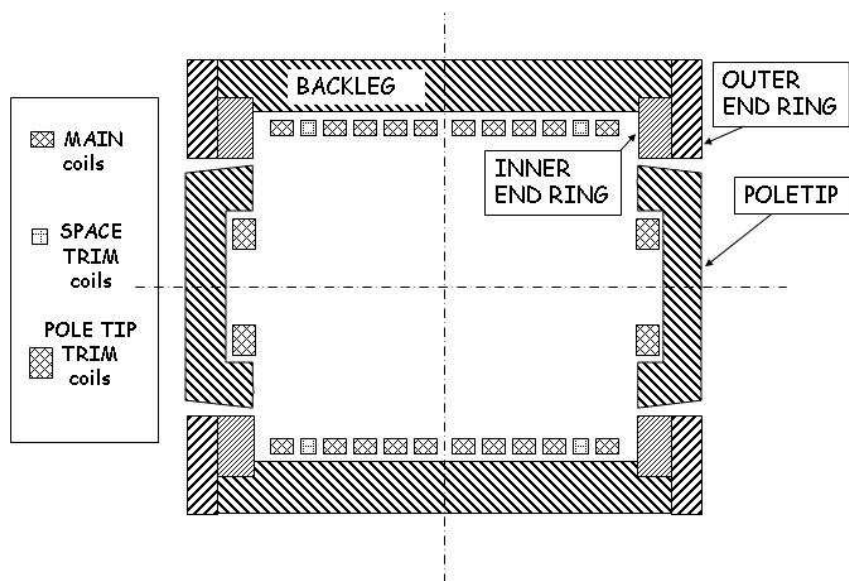


Figure 2.6: Schematic representation of a longitudinal cross-section of the STAR magnet.

photon analysis is currently in progress.

### 2.2.1 The STAR Magnet

The key to STAR tracking is the quality of its magnet. The magnetic field curves the paths of charged particles, which makes it possible to identify low momentum particles. STAR has a solenoidal magnet, which consists of three types of aluminum coils: Main, Space Trim and the Poletip, powered by five separate power supplies. The coils are mounted on the cylindrical steel frame of the magnet, which acts as a return flux for the magnetic field and as support for the entire STAR detector. The steel and the coils are arranged as seen in Figure 2.6 and weigh 1100 tons. The number and the arrangement of the coils is designed to provide as uniform a field as possible throughout the entire volume of STAR. Extra care is taken to map the STAR magnetic field precisely for use in tracking. The field map is shown in Figure 2.7. The greatest variation of the magnetic field occurs at the outermost radius of the STAR Time Projection Chamber (see below), at 200 cm. There the field distortions

reach a maximum of 40 Gauss. The STAR detector operational magnetic field varies from 0.25 to 0.5 Tesla (1T = 10,000 Gauss). The data used in this work was obtained at  $B = 0.5$  Tesla. Thus, a field variation of 40 Gauss is less than 1%, and is negligible for this work.

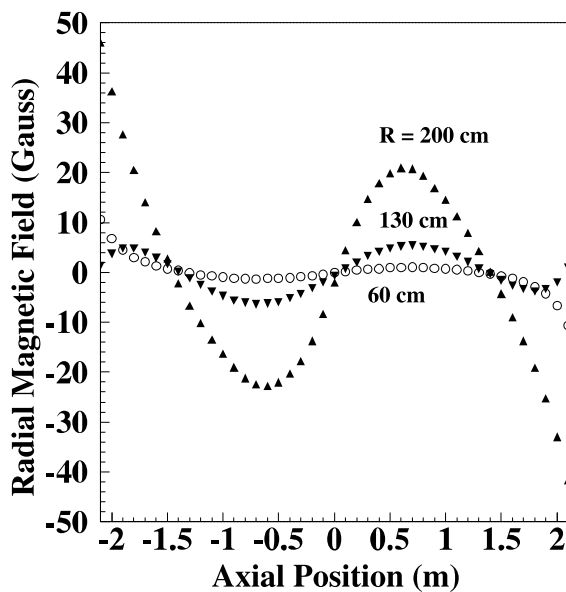


Figure 2.7: Measurement of the radial component of the STAR magnetic field, as a function of axial ( $z$ ) position at three radii taken at  $\phi = 0^\circ$

## 2.2.2 Tracking Detectors

STAR's analysis is strongest when its excellent tracking capabilities at mid and forward rapidities are used. There are three tracking detectors in STAR: the TPC, SVT and the FTPC. Only the first two were used in the analyses of this thesis.

### Time Projection Chamber

The STAR's Time Projection Chamber (TPC) is sometimes described as a four-dimensional digital camera. It creates a snapshot of the collision by recording the the trajectories and energy loss per unit length of charged particles traversing its volume.

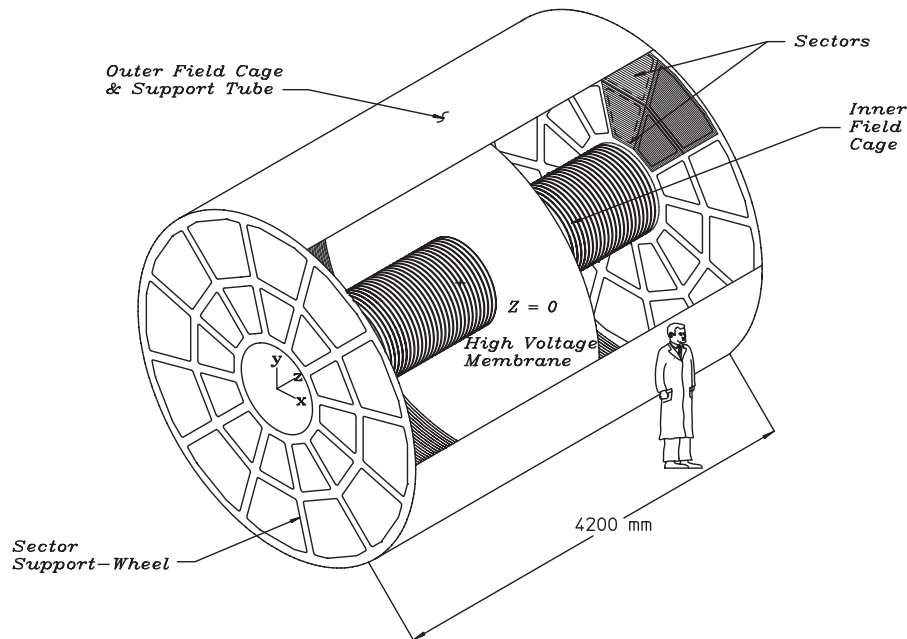


Figure 2.8: The layout of the Time Projection Chamber.

The TPC is 4 m in diameter, 4.2 m in length cylinder, divided by a high-voltage membrane and filled with a 10% methane and 90% argon gas admixture at a pressure slightly higher than atmospheric. There are readout pads at both ends of the cylinder, covering radial distance from the beam line center ( $r$ )  $50 < r < 200$  cm. A schematic diagram of the detector is seen in Figure 2.8, where the central high voltage membrane, the sector support-wheel and the inner and outer cylinders are designated. The TPC is positioned inside the magnetic field of the STAR magnet, discussed above.

There are several main features of this TPC that make it such an excellent tracking device.

- A uniform, medium-strength magnetic field curls charged particle paths into helices allowing for precise momentum reconstruction of each particle traversing the TPC volume.

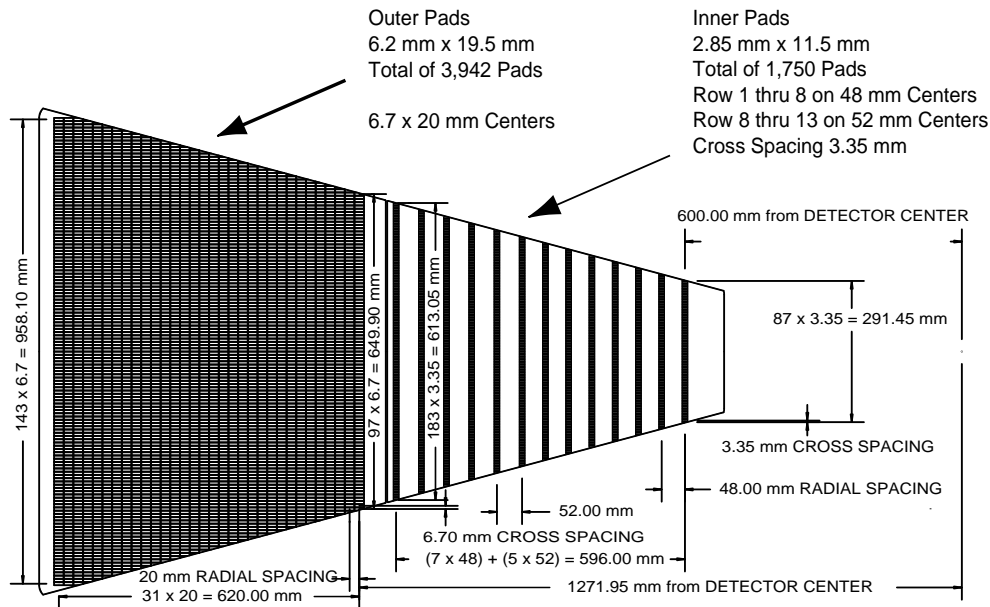


Figure 2.9: The layout of a TPC sector and readout pad.

- The central membrane acting as a Cathode is held at  $-28$  kV. The TPC endcaps are held at ground voltage, enabling ionizing electrons to drift to read-out pads on the endcaps, so that the energy loss per unit length of particles traversing the TPC volume can be recorded. Using the energy loss information, as well as the spatial position of charge deposits at the endcaps, one can perform particle identification as described in the section below.
- The TPC provides full azimuthal coverage and good rapidity coverage ( $|\eta| < 1.8$ ), allowing a sufficient acceptance for a variety of analyses.

Although there are many advantages of the TPC, there are certain shortcomings. The electron drift speed is slow –  $5.45$  cm/ $\mu$ s (it takes about  $40$   $\mu$ s for the electrons to drift to the TPC endcaps), and at high luminosities this leads to pile-up of events. The pile-up conditions are manageable for high-multiplicity events, where the primary vertex can be reconstructed and the tracks sorted out, however, in low-multiplicity collisions pile-up can become a problem. The slow drift speed also leads to a low event rate –  $0.1$  kHz for STAR as compared to  $10$  kHz for PHENIX.

The basis of the TPC operation principle is as follows:

1. After the collision occurs, particles emanate from the interaction point. Those that are charged, ionize the gas in the detector volume along their trajectories, as they traverse the TPC.
2. Electrons from the ionization drift to the anodes in the two TPC endcaps. There the signal is read out by the Multi-Wire Proportional Chambers (MWPCs), positioned before the read-out pads. The read-out process unfolds as follows. First, the ionization electrons pass the TPC gating and the shielding grid, both held at ground potential with respect to the central membrane for triggered events. If the event was not triggered, the gating grid is closed. Then the drift electrons are accelerated toward the anode wires, avalanching in the process (one drift electron can create up to 3000 avalanche electrons). The avalanche clouds are detected by the TPC read-out pads.
3. The two TPC endcap readouts consist each of a twelve-sector wheel. Each wheel contains forty-five padrows, 13 on the inner subsector, equipped with smaller pads ( $2.85 \times 11.5$  mm) and 32 rows of larger ( $6.20 \times 19.5$  mm) pads on the outer subsector, as illustrated in Figure 2.9.
4. Several steps are involved to convert track ionization in the TPC gas to particle trajectories. First ionization clusters are found, separately in  $x$ ,  $y$ , and  $z$  space [36]. The  $x$  and  $y$  positions of a hit are found by fitting a gaussian to the distribution of pixel clusters located on a given pad. To measure the  $z$  position of a hit, one needs to know the distance traversed by the electron cloud and the drift velocity at the time of drift. The drift velocity is calculated using calibration data available from daily laser runs, while the distance drifted by the electron cloud is calculated by measuring the time of arrival of the electrons on the pad in “time buckets” and then weighting the average of these by the number of electrons collected in each bucket. [36]. A representation of a TPC cluster is shown in Figure 2.10 along with the STAR coordinates.
5. The track finding algorithm is used to associate TPC clusters (hits) with particle trajectories, tracks, as explained in Chapter 3.

6. Once the track is found, the total  $dE/dx$  of the particle can be calculated. The total energy loss is found by using all padrows (up to 45) traversed by the particle. The padrow clusters are fit using a top-30% truncated gaussian. The length over which the energy loss occurred is calculated taking into account the dip<sup>1</sup> and crossing<sup>2</sup> angles of the track. The momentum of the track can be calculated via the simple  $p = qrB$ , where  $p$  is the total momentum,  $q$  charge of the particle (assumed to be either +1 or -1 depending on the direction of track's curvature),  $r$  radius of the helix and  $B$  is the magnitude of the magnetic field. Using the  $dE/dx$  information and the total momentum of the track, an identification of particles at low momentum (where the majority is produced), is possible using the Bethe-Bloch curves, as seen in Figure 2.11. The curves are generated using the Bethe-Bloch formula [1],

$$-dE/dx = Kz^2 \frac{Z}{A} \frac{1}{\beta^2} \left[ \frac{1}{2} \ln \frac{2m_e c^2 \beta^2 \gamma^2 T_{max}}{I_2} - \beta^2 - \frac{\delta}{2} \right] \quad (2.1)$$

where  $Z$  is the particle charge,  $\beta = v/c$  is the particle velocity,  $A$  and  $z$  are respectively the atomic mass and number of the absorbing material,  $T_{max}$  is the maximum energy that can be transferred to a single electron in one collision,  $I$  is the mean excitation energy, and  $K$  is a constant, defined as  $4\pi N_A r_e^2 m_e c^2 = 0.3071 g^{-1} cm^2$  ( $N_A$  here is the Avogadro number, and  $r_e$  is the classical electron radius). The other variables used in Eq. 2.1 are  $m_e$ , which stands for the mass of the electron,  $\gamma = \frac{1}{\sqrt{1-v^2/c^2}}$ , and  $\delta$ , the density effect correction to ionization energy loss [1].

## Silicon Vertex Tracker

In order to improve the tracking of low transverse-momentum (below 150 MeV/c) particles and detection of short-lived hadrons such as strange baryons and  $K_S^0$ , the STAR detector is equipped with a tracker that sits close to the beam pipe and has high resolution, 25  $\mu m$  for space points and a two-track resolution of 500  $\mu m$ . The

---

<sup>1</sup>The angle between particle momentum and the direction of the electron drift.

<sup>2</sup>The angle between particle momentum and the read-out plane.

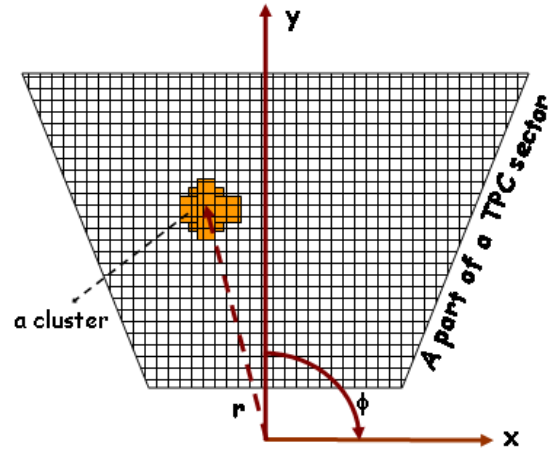


Figure 2.10: A schematic representation of a TPC cluster in STAR coordinates. The position of the cluster is determined by a truncated mean of a gaussian in  $x$  and  $y$  space.

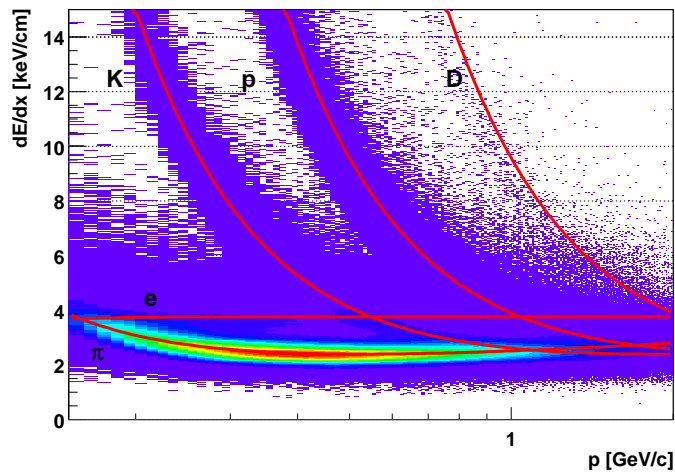


Figure 2.11: Loss of energy per unit length ( $dE/dx$ ) as a function of total momentum of tracks found in the TPC. Particle identification is done using the Bethe-Bloch curves as discussed in text.

Silicon Vertex Tracker (SVT) consists of three cylinder layers of silicon drift detectors with their inner boundaries at  $r = 6.37, 10.38,$  and  $14.19$  cm from the center of the

beam pipe. In addition, there is a Silicon Strip Detector (SSD) barrel that is located at  $r = 23$  cm, and which acts as a fourth inner tracking layer. These layers provide full azimuthal coverage and extend over  $|\eta| < 1$  in pseudorapidity.

The SVT consists of 216 p-type  $6.3 \text{ cm} \times 6.3 \text{ cm} \times 280 \text{ }\mu\text{m}$  silicon wafers [37]. Each wafer is divided into two halves by a central cathode to minimize the drift distance for the electrons. The electrons drift to the nearest anode, located at opposite ends of the silicon wafer. There are 240 anodes in each drift direction. The electron drift speed at the maximum applied anode voltage of 1500 V (which corresponds to a field of approximately 500 V/cm) is  $6.75 \text{ }\mu\text{m/ns}$ . This results in a maximum drift time of  $4.5 \text{ }\mu\text{s}$  [37].

Initially, the SVT was expected to improve the efficiency of  $K_S^0$  detection in order to allow  $K_S^0$  Hanbury-Brown-Twiss interferometry (HBT). With the first collisions at RHIC, it was recognized immediately that the predicted event multiplicities were overestimated by up to an order of magnitude [38, 39]. Also the TPC performed better than most expected, and the 10%  $K_S^0$  detection efficiency that was thought to be achievable only with SVT was reached by using the TPC tracking exclusively [39]. Nevertheless, the SVT slightly improves the signal-to-noise ratio for  $K_S^0$ ,  $\Lambda^0$ , and multi-strange baryons. This makes it very useful in analyses where raw clean counts of detected particles are essential. The azimuthal correlation measurement is one such analysis.

### 2.2.3 Calorimetry

STAR is equipped with two electro-magnetic calorimeters. One completely surrounds the outside of the cylinder of the TPC, and is called “the Barrel EMC,” or “BEMC,” the other is mounted at the East end of the TPC and is referred to as the Endcap EMC Calorimeter, or the EEMC. Because the endcap calorimeter was not used in this analysis, its description will be omitted.

The BEMC is made up of 120 calorimeter modules. Each module subtends  $6^\circ$  in  $\Delta\phi$  and spans 1 unit of pseudorapidity (either  $0 < \eta < 1$  or  $-1 < \eta < 0$ ). Each module consists of 40 towers, which in turn consists of three sub-detectors each. First, there

are the calorimeter towers, made of sandwiched scintillator material and lead. Then there are two shower-maximum detectors, each measuring the energy deposition in its own direction: one in  $\phi$ , the other in  $\eta$ . Correspondingly, one detector is called SMD- $\phi$ , the other – SMD- $\eta$ . These are located about 15 cm from the front plate of the BEMC. Each tower is  $\Delta\eta \times \Delta\phi = 0.05 \times 0.05$  in size, i.e., at  $\eta = 0$  the tower size is  $10 \times 10$  cm<sup>2</sup>, but it increases as  $\eta$  increases. Each SMD is a wire-proportional counter-strip readout detector that uses a gas amplification of approximately 3000 [40].

In conjunction with TPC tracking, the BEMC is effectively used to identify electrons (including single electrons that result from heavy quark decay), neutral pions, and photons.

## 2.2.4 Triggering detectors

STAR uses several fast detectors for triggering. As a result, the STAR trigger is very robust, allowing to trigger on rare probes, such as charmonium and bottomonium probes,  $J/\psi$  and  $\Upsilon$ , as well as on a broad range of collision energies and sizes.

### Zero Degree Calorimeters

One way to determine the centrality of a collision quickly is to look at the remainder of that collision, i.e., particles left intact after each event. One way to do this is to collect and calculate the energy deposits of neutrons, traveling at beam's rapidity. Neutrons are not affected by the magnetic field of the detector and because their rapidities are so forward, we know they were not produced during the collision. Each experiment at RHIC is outfitted with two Zero Degree Calorimeters (ZDCs), located downstream on both ends of the detector, which are designed to catch and count these neutrons. At STAR the ZDCs are located 18m west and east of the interaction point at the center of the detector, as shown in Figure 2.12. The ZDCs are small, only 10 cm wide, hadron calorimeters. Each calorimeter consists of three modules made of tungsten and overlaid with fibers through which the signal is collected. At STAR, as at other RHIC experiments, they are used as triggering detectors, because

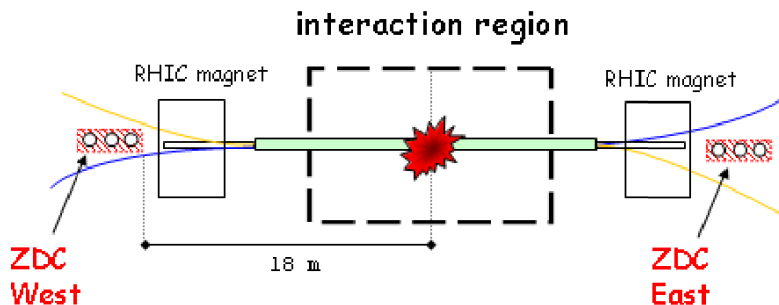


Figure 2.12: The position of ZDCs with respect to the interaction area. The figure is not drawn to scale. The neutrons travel down the beam pipe extension and are unaffected by the RHIC columating magnets.

they allow an on-line, albeit approximate, determination of the event's centrality.

### Central Trigger Barrel

Another way to determine the centrality of the collision quickly and without resorting to the entire event reconstruction, is to count the number of charged particles leaving the collision region. This is easily done by surrounding the detector with scintillator material. The Central Trigger Barrel (CTB) slats cover almost the complete  $2\pi$  surface area of the TPC's outer cylinder. There are 240 scintillator slats, each consisting of a radiator, a light guide, and a photomultiplier tube [41]. The slats have a near 100% efficiency. The centrality of the collision determination may be done on-line by just using the CTB and the ZDC information, as seen in Figure 2.13. Small deposits in the ZDC and large counts in the CTB correspond to small impact parameters, i.e., most central events, while events with few CTB and high ZDC counts tend to correspond to peripheral events, where the impact parameter is large.

For the azimuthal correlations measurement, presented in chapters 3 and 4, the CTB has also been used as a tracking detector to help avoid pile-up of tracks in the  $p + p$  collisions. The method was first developed by Jonathan Gans [17]. In order to ensure that a given particle originated within the same event for which we have

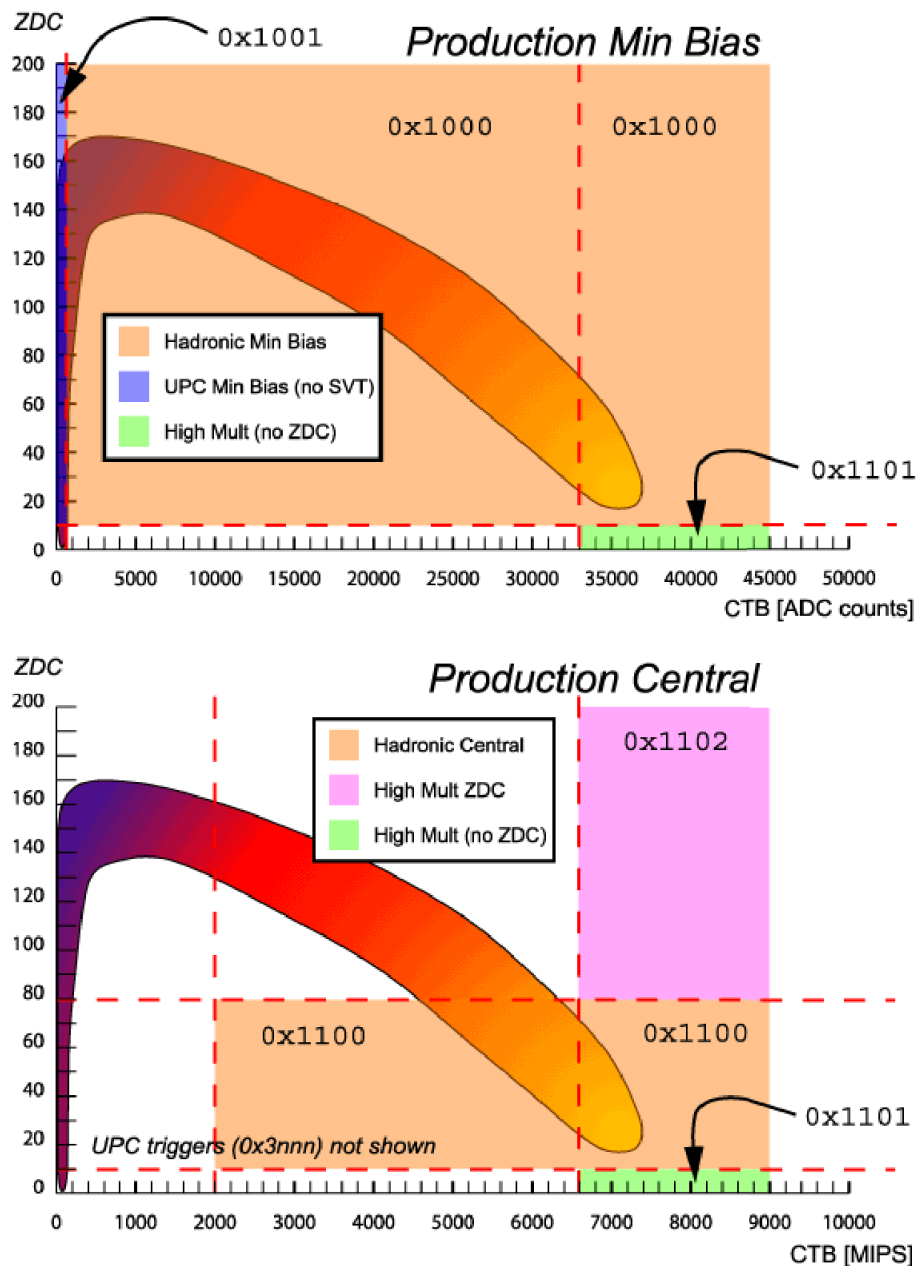


Figure 2.13: Trigger definitions in Au+Au collisions at  $\sqrt{s_{NN}} = 200$  GeV presented as a function of ZDC vs. CTB counts.  $0 \times 1000$ ,  $0 \times 1001$ ,  $0 \times 1101$ , and  $0 \times 1102$  correspond to various trigger IDs in the STAR software.  $0 \times 1000$  corresponds to the minimum bias trigger. All collisions that left ZDC deposits above 10 units and a CTB count of 500 or above are recorded as minimum bias collisions. Collisions with low ZDC counts, but high CTB counts were triggered as “central,” and correspond to trigger ID  $0 \times 1100$ . Other trigger set-ups, such as the Ultra-Peripheral event trigger, are not used in this work and therefore are omitted.

a primary vertex, the particle's exit from the detector can be pin-pointed using the CTB. This method works only with particles of sufficient momentum (the cut-off to reach the CTB is 160 MeV/c) and with sufficiently low multiplicity (because of high granularity of the CTB) [17]. Because the analysis deals with the intermediate  $p_T$  region, all tracks used in the analysis were eligible for CTB matching.

### **Beam-Beam Counters**

The STAR detector is equipped with two honey-comb-like structures made up entirely of photomultiplier tubes at each of the forward regions. These comprise the STAR Beam-Beam counters (BBC), used to trigger in events where the use of ZDCs is impossible or impractical due to the low neutron content of the colliding nuclei, as is the case in the  $p+p$  collisions. The inner part of each BBC is composed of small inner tiles made of scintillator material. BBCs can also be used as vertexing detectors. By comparing the arrival time of collision remnants to each of the BBC faces, one can determine the  $z$  position of the collision itself. Unfortunately, due to its low timing resolution (1 ns), the spatial resolution of the event vertex determination is also low – only about 60 cm [17].

### **Barrel Electro-Magnetic Calorimeter Towers**

The STAR BEMC was described in detail above. As a triggering detector it is used to select events which produce particles with energy above the set threshold, thus selecting events with jets. It is also used to select events with certain rare probes: for instance, the threshold can be set on adjacent towers to select closely associated high  $p_T$  electron or muon pairs, which might be a product of  $J/\psi$  decay. To trigger the recording of an event, there is no need for full reconstruction of particle energy, it is enough that an above-threshold energy deposit is left in one (or in case of rare probes – several) of the towers.

### 2.2.5 STAR Data Acquisition System

The STAR Data Acquisition System (DAQ) starts with the STAR triggering system. It is organized in four levels. Level 0 trigger is the fastest, operating using the ZDC, CTB, BBC, MWC, and the BEMC detector setups. While the data that passed Level 0 is being digitized and written out, a subset of the data is analyzed by the Level 1 trigger, and if it passes the pre-set trigger condition, Level 2 trigger takes over. Then some of the data is passed to Level 3, the on-line reconstruction software, which includes displaying the reconstructed event in real time, so it can be inspected visually. At any point as the event passes through the triggering system, the event can be rejected. If it is accepted, however, it is written out onto the disks of the High Performance Storage System (HPSS) facility. In the meantime, to optimize the data taking time, several events at a time are juggled between the various trigger levels.

Before being recorded, each event is received from detector Front End Electronics (FEEs) via the optical fibers by the multiple receiver boards (there are several for each detector, 144 for just the TPC). Each board has its own separate optical fiber feeding the data. The boards are organized in VME crates, controlled by the Detector Broker CPU (DET). The TPC is serviced by 12 such DETs, the SVT and the FTPC has two each, while other detectors are serviced by one DET each [42]. The VME crates and the DETs are interconnected via a Myrinet networking system, which is the one responsible for sending the data to HPSS.

In 2004 the TPC FEEs were upgraded to handle the data 100 times faster. A future upgrade, including moving from TPC pixel to cluster read-outs is planned in the near future.

# Chapter 3

## Data Reconstruction and Simulations

### 3.1 Event Reconstruction

There were three data sets used in the analysis,  $p + p$ ,  $d+Au$  and  $Au+Au$ , all at  $\sqrt{s_{NN}} = 200$  GeV. Each of these data sets presented a different challenge due to the differing geometries and number of participating nucleons. For instance, the  $p + p$  data were challenging because the low multiplicity events made the reconstruction of a precise event vertex difficult and the correlation measurement statistics-hungry. The central  $Au + Au$  data, with the hundreds of tracks per event, were challenging for the exact opposite reason: the background is very high.

The  $p + p$  data were of two types: minimum bias triggered and triggered using the STAR BEMC.

Obtaining the components used for correlations is a multi-step process, and to be consistent and clear I would like to start from the basics of track and vertex reconstruction, and work my way up to the multi-strange baryon finding.

### 3.1.1 Tracking and Track Selection

The trajectories of charged particles that originate in the collision region and then traverse the TPC volume, are reconstructed using the information collected at each TPC pixel and (if available) SVT-SSD strip, the so-called “ionization points”. As described in detail in Chapter 2, the particles passing through the detector ionize the gas mixture that fills the TPC and the freed electrons drift to the detector end-caps, where the total signal, deposited at TPC padrow crossings, is divided between (usually) several detector pixels. In each pixel the observed signal is amplified and recorded, after it passes through the analog-to-digital (ADC) converter, which gives it a value between 0 and 512 (9-bit resolution ADC). At the end of the TPC digitization and read-out process, each ionization point has a time stamp, coordinate position, and an ADC value associated with it. Then, to determine the total energy deposited by the ionization electron, pixel information must be clustered, i.e., the pixel data passes through the STAR cluster-finding software. The clustering algorithm searches for ionization points, which contain ADC values above threshold and that are close together in three dimensions (one time and two space dimensions – the fourth, the z-coordinate, is derived from its time “coordinate”). All ionization points collected in a cluster are marked as used, and the search for clusters continues until all points with ADC value above a given threshold are exhausted. Each cluster forms a TPC hit.

Once the clusters are constructed, the identification of the entire particle path, its *track*, can proceed. The algorithm starts with the TPC pads farthest away from the detector center, and works its way inward. Each TPC row can only account for one hit of the track. Thus the maximum number of hits associated with each track is 45. The algorithm identifies points that lie close together in space and calculates the extrapolated curve. With each hit point added to the track, the extrapolated curve is refit. The outliers are removed and the points added to the track are marked as used. All possible segments using the given set of points are looped over and in the end of the loop summed. The extrapolation takes into account the fact that a charged track can be described by a helix within the TPC volume, since the STAR magnetic field is uniform. The helix can be parameterized as a function of the track length, and

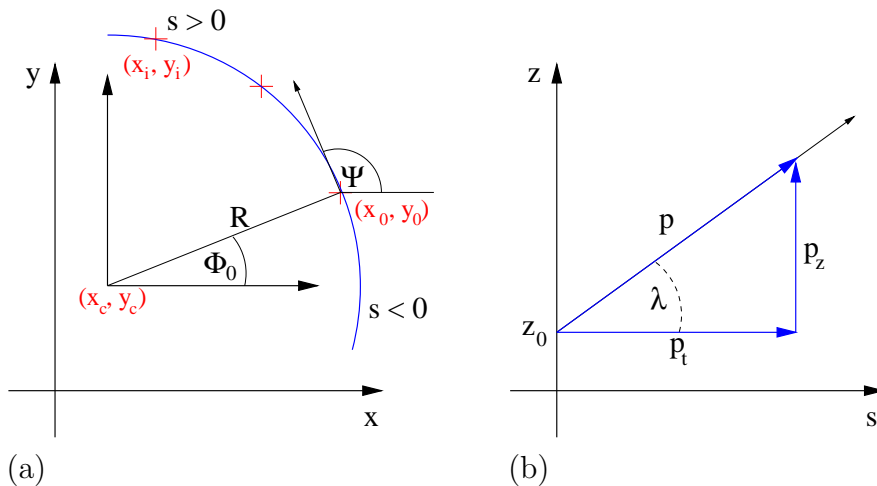


Figure 3.1: Visualization of the helix in two projections: (a) shows the projection of the helix in the  $xy$  plane, (b) shows the projection of the helix in the  $sz$  plane. The meaning of  $s$ ,  $\lambda$ ,  $\Psi$  and  $R$  is given in the text.

described in Cartesian coordinates as [43]

$$x(s) = x_0 + \frac{1}{\kappa} [\cos(\Psi_0 + hs\kappa \cos \lambda) - \cos \Phi_0] \quad (3.1)$$

$$y(s) = y_0 + \frac{1}{\kappa} [\sin(\Psi_0 + hs\kappa \sin \lambda) - \sin \Phi_0] \quad (3.2)$$

$$z(s) = z_0 + s \sin \lambda \quad (3.3)$$

where  $s$  is the path along the helix, as illustrated in Figure 3.1a,  $\lambda$  is the dip angle (Figure 3.1b),  $\kappa$  is the curvature ( $1/R$ ),  $\Phi = \Psi + \pi/2$ , and  $\Psi(s)$  is the azimuthal angle of the track direction at the starting point of the helix, and  $h$  is  $\pm 1$ , i.e., the rotation of the projected helix in the  $xy$  plane, which depends on the sign of the product of magnetic field  $B$  and particle charge  $q$ .

In the  $xy$  plane the helix projection is nearly an arc of a circle. In any of the planes parallel to the  $z$ -axis, the track trajectory is a section of a sinusoidal curve, which can be approximated by a straight line. A track with higher momentum (e.g.,  $p_T > 3$  GeV/c) has a relatively small curvature and to a naked eye looks like a straight line. Tracks with lower  $p_T$  (which are a majority of those seen in STAR) are visibly curved.

However, at this point the tracks found by the algorithm (all called “global” tracks, as no information other than their TPC hits were used in track-finding) are not yet usable for physics analysis. The tracks are refit using a Kalman filter algorithm [44].

The track passes through the Kalman filter three times. In the first pass, calculation of the proximity of points to the fitted curve is calculated. On the second pass, all the distortions due to the field non-uniformities, average energy loss and multiple scattering of the electrons in the material are taken into account. On the third pass of the filter, the track is smoothed and the least  $\chi^2$  fit is used to calculate the optimal particle trajectory.

### 3.1.2 Event Vertexing and Primary Track Finding

The next step in establishing the event geometry is recreating the coordinates of the space-point where the collision took place: finding the *primary vertex* of the event, i.e., the physical coordinates of the beam-crossing.

The beam-line dimensions (4 cm in diameter) and the physics of beam acceleration restrict the position of the primary vertex in the transverse direction, thus the main challenge is to locate the interaction point's  $z$  coordinate. The vertex is found by using the tracks reconstructed in a given event and then calculating a common point closest to all reconstructed tracks except for the outliers.

The TPC's inner radius permits tracking starting only at 50 cm from the beam-line. Therefore, the first step in the vertex-finding procedure is to extend the track helices beyond the TPC inner radius, to a distance as close as possible to the beam line. The helix segments close to the beam line are approximated by straight lines and the Least Squares Method is used to calculate the actual primary vertex location [45].

When the collisions occur at lower luminosities and the events contain hundreds of tracks, finding the vertex is a relatively straight forward procedure. The picture changes when the mean event multiplicities fall into the single digits, and the luminosities are high, as is the case in  $p + p$  collisions. The result is what is referred to as “pile-up” events – several collisions with multiple vertices, recorded by the detector as one. For a correlation study it is important to ensure that both particles being correlated originate from the same event. In order to do that, CTB matching is employed, i.e., only tracks that can be projected from the TPC to CTB radius and

	<i>Quark Content</i>	<i>Mass</i> [GeV/ $c^2$ ]	$c\tau$ [cm]	<i>Decay Mode</i>	$\Gamma_i/\Gamma$ [%]
$\Xi^-$	$dss$	1.321	4.91	$\Lambda^0\pi^-$	99.89
$\Xi^+$	$\overline{dss}$	1.321	4.91	$\overline{\Lambda^0}\pi^+$	99.89
$\Omega^-$	$sss$	1.673	2.461	$\Lambda^0K^-$	67.8
$\Omega^+$	$\overline{sss}$	1.673	2.461	$\overline{\Lambda^0}K^+$	67.8

Table 3.1: Selected properties of the multi-strange baryons and their decays

matched with a CTB hit are used in vertex reconstruction [17]. Similarly, to ensure that both particles used in a correlation come from the same event, all tracks involved in particle reconstruction are matched to the CTB in the same manner.

In each data-set the  $z$ -coordinate range of the usable events was different. In  $p + p$  data the CTB matching allowed for a wide latitude in vertex selection, and thus in that data set we took  $|z_{vertex}| < 100$  cm; in  $d$ +Au data the  $z$  coordinate of the vertex was restricted to  $z < |50|$  cm; in Au+Au  $|z| < 25$  cm, to conform to the track efficiency measurement, done for that interval. If the vertex was not found, in all three data sets the events were rejected.

### Primary tracks

Thus far the reconstructed tracks were global, i.e., although all tracks were used in primary vertex reconstruction, there was no requirement that they all pass through the vertex. However, because we are interested in the processes that take place before the medium formation, i.e., initial state processes, we insist that both correlation partners come from the primary vertex. Thus, the charged tracks that are used to construct correlations with  $\Omega$  and  $\Xi$  baryons are marked as “primary” by the STAR reconstruction software. This means that the track’s fit points include an extra hit – the primary vertex. In addition, the STAR software labels the track as “primary” if the distance of closest approach ( $dca$ ) of the tracks to the primary vertex is less than 3 cm. In this study only tracks with  $dca < 1$  cm were used.

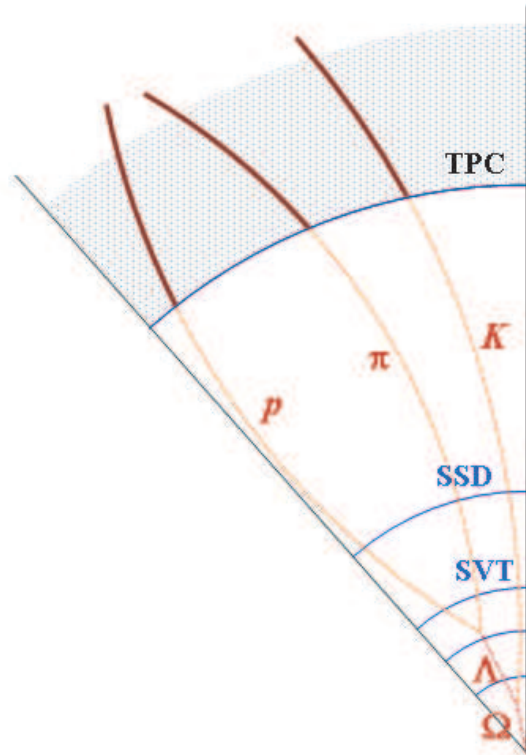


Figure 3.2: Tracks seen in the TPC.

### 3.2 $\Xi$ and $\Omega$ Baryon Reconstruction

This section will deal with reconstruction of the properties of multi-strange baryons used in the analysis. Although both  $\Omega^\pm$  and  $\Xi^\pm$  baryons are charged particles, and their lifetimes are measured in  $\text{cm}/c$  (see Table 3.1), they cannot be seen in the detector directly, since the inner radius of the TPC is 50 cm. There is more than one technique to obtain particle characteristics such as yields, temperature, and momentum distribution. However, for this analysis we require the reconstruction of the baryon itself, on a particle-by-particle basis. Therefore, the only suitable method is the particle path reconstruction using the multi-strange decay topology.

Both  $\Omega$  and charged  $\Xi$  baryons leave a signature decay structure: a three-track

“cascade” topology, as seen on Figure 3.2. Any multi-strange baryon decays into a charged meson and a neutral  $\Lambda^0$  baryon, which in turn decays into a pion and a proton, hence the “cascade” label. The track information for the multi-strange particle decay is carried by the three daughter tracks, shown in Figure 3.2 as solid lines. Thus, reconstruction of a multi-strange baryon involves a step-by-step reconstruction of a multilateral vertex, first finding a suitable  $\Lambda$  baryon candidate, and then finding a matching meson.

The procedure starts with reconstruction of the event vertex and primary and global tracks, as described above. The reconstruction is a part of a centralized software scheme, which includes many subroutines to prepare the data on tape for physics analysis. One such subroutine is the reconstruction of the secondary vertex candidates. The software that does this is called the Secondary Vertex Finder. It loops over a collection of tracks in a given event, selecting pairs that pass the predefined criteria. This criteria is commonly referred to as the “reconstruction-level cuts.” These are designed to allow maximum flexibility of subsequent physics analysis, while removing a significant amount of noise that otherwise would be cluttering the limited computing disk space. The cuts at this level are made on the maximum impact parameter of the would-be reconstructed cascade particle with respect to the primary vertex, the distance of closest approach (*dca*) of the particle daughters ( $\Lambda$  and a charged meson), the minimum decay length of the particle, calculated from the primary vertex, and the difference between the invariant mass of the lambda daughter and that listed in the particle data book. The numerical values of these cuts for three different data sets are listed in Table 3.2. In addition, each of the three tracks involved in the cascade reconstruction process is required to include at least 11 TPC hit points.

Examining Table 3.2, we see that the cuts are more relaxed for data sets with lower average multiplicities. Note that the cuts are applied to a vertex type class, not to a particular particle. At this level, cuts for  $\Omega$  and  $\Xi$  baryons are the same.

In STAR, data usable for physics analysis is stored in predefined data structures, called “MuDSTs” (stands for “micro data storage tapes”). For the analysis in  $p + p$  and  $d + \text{Au}$  data sets, further selection criteria on all correlation candidates was applied directly to MuDSTs. However, in Au+Au year 04 data, where the event and the data

Cut Variable	$p + p$	$d + \text{Au}$	<b>Au+Au</b>
Cascade daug. $dca$	$< 1.2$ cm	$< 1.2$ cm	$< 0.8$ cm
$dca$ Cascade to PVx	no cut	no cut	$< 0.8$ cm
dl Cascade	no cut	$> 2.0$ cm	$> 2.0$ cm
dl $\Lambda$	$> 0.5$ cm	$> 4.0$ cm	$> 5.0$ cm
$\Lambda$ mass cut	$< 0.01$ GeV/ $c^2$	$< 0.01$ GeV/ $c^2$	$< 0.01$ GeV/ $c^2$
$dca$ $\Lambda$ $\pi$ daug. to PVx	no cut	no cut	$> 2.0$ cm

Table 3.2: Reconstruction level cuts on cascade-type vertices.

sample size are very large (and examining every event of the data takes several days), the analysis procedure was slightly modified as follows. There were two levels of data filtering. In the first pass, all of centrally triggered (see Appendix A) Au+Au data was considered, however only selected information from a subset of events was recorded in a different, customized data structure. The criteria was as follows:

1. The event had a valid primary vertex within a specified range.
2. The event had the predefined charged particle multiplicity.
3. The event had to contain at least one cascade candidate that passed the predefined set of parameters.

If the event passed all of the aforementioned criteria, the event-specific information, the eligible cascade candidates, and all charged tracks above a certain momentum threshold were saved. All of the subsequent analysis utilized these new, smaller data structures. This allowed a significant reduction in the time for the subsequent physics analysis. Thus, when we turn to the selection criteria for the multi-strange baryons in Au+Au collisions, two sets of cuts will be presented: the filtering level cuts and the cuts used for the final analysis.

### 3.2.1 $\Xi$ baryons

Over 99% of the  $\Xi$  baryons decay into a  $\Lambda^0$  baryon and a charged pion. For ease of terminology we call the  $\Lambda^0$  and the other pion *cascade decay daughters*, the pion being the *bachelor* meson. As the  $\Lambda$  baryon is neutral, the track itself is not seen by

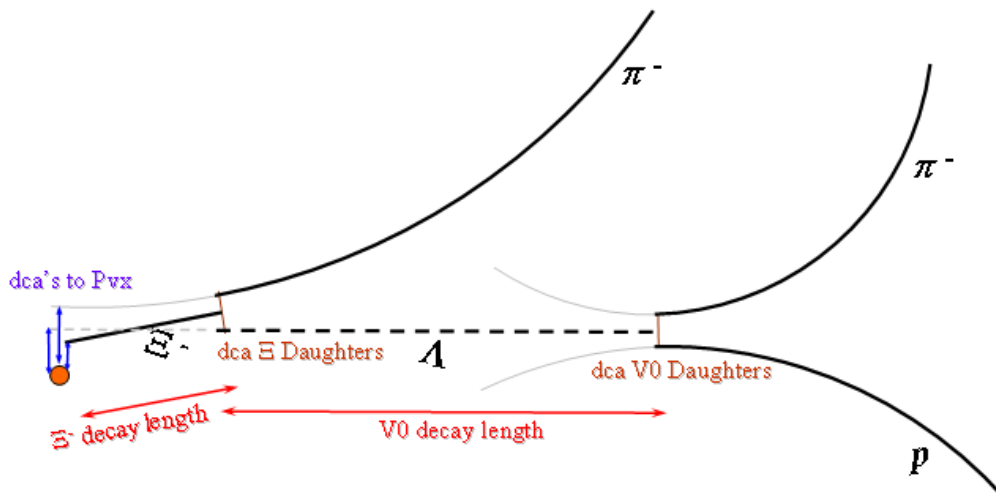


Figure 3.3: The topology of a cascade decay, where the weak decay of a  $\Xi^-$  baryon is taken as an example. The charged tracks are represented in the figure by solid lines, and the neutral  $\Lambda$  track – by a dashed line. The vertex type is called a “cascade” because of the multi-stage decay process. All seven geometrical variables used for  $\Xi^-$  topological reconstruction are represented.

the TPC. Instead  $\Lambda^0$  decay products are used for the  $\Lambda$  baryon track reconstruction. 63.9% of  $\Lambda$  baryons decay into a pion and a proton (we call these *lambda daughters*). The topology of the decay is V-shaped, the particle that the decay vertex came from is neutral, and therefore invisible in the TPC. Thus, this type of a vertex is called a “V0”. Another example of a V0 vertex would be a vertex left after the decay of  $K_S^0$  meson into  $\pi^+$  and  $\pi^-$ .

The three resultant particles, two pions and a proton, are then separately reconstructed in the TPC, as described in the tracking section. A  $\Lambda$  decay is reconstructed from its daughters. But first, one needs to identify the tracks that compose a given

V0 decay vertex. This is done using the Bethe-Bloch curves that use the energy-loss information gathered by the TPC.

Then, particle selection is made based on six out of seven possible topological criteria, described in Figure 3.3, three track criteria, and a cleaner cut around the  $\Lambda$  daughter mass. The three track quality criteria are the number of fit points used to make a track (there are three because there are three tracks involved in the  $\Xi$  reconstruction). The possible topological criteria were:

1. Distance of closest approach of the  $\Xi$  baryon to the primary vertex (*dca*  $\Xi$  to PV).
2. Distance of closest approach of the  $\Lambda$  daughter to the primary vertex (*dca*  $\Lambda$  to PV).
3. Distance of closest approach of the bachelor  $\pi$  to the primary vertex (*dca* Bach. to PV).
4.  $\Xi$  baryon decay length.
5.  $\Lambda$  daughter decay length.
6. Distance of closest approach between  $\Xi$  daughters,  $\Lambda$  and the bachelor pion.
7. Distance of closest approach between  $\Lambda$  daughters, the proton and the  $\Lambda$  daughter pion.

The bachelor *dca* to the primary vertex criteria was not used, as it was found that a sufficiently pure  $\Xi$  signal was possible without it.

### 3.2.2 $\Omega$ Baryons

The process of reconstructing  $\Omega$  baryons is similar to that of the charged  $\Xi$  baryons. However in this case, the particles selected for vertex reconstruction are a pion, a proton ( $\Lambda^0$  decay daughters), and a charged kaon (i.e., the *bachelor meson*). The identification process of a  $\Lambda$  baryon is the same as that of the  $\Lambda$  in the  $\Xi$  baryon

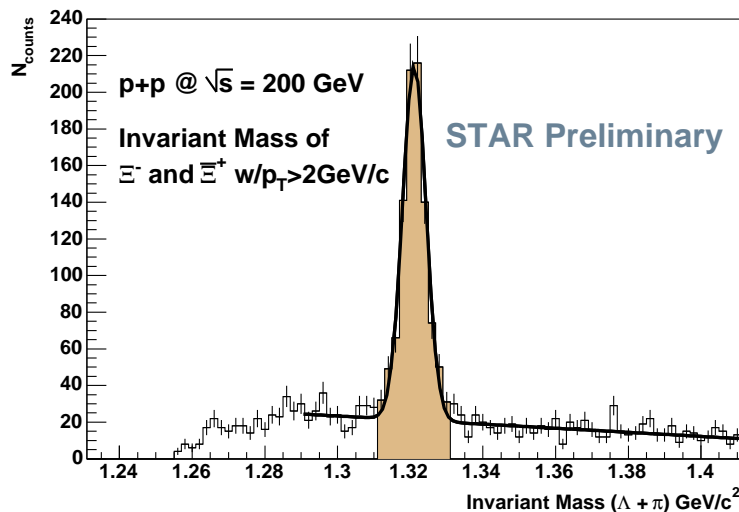


Figure 3.4: The invariant mass of  $\Xi^-$  and  $\Xi^+$  baryons (with  $p_T > 2$  GeV/c) in  $\sqrt{s} = 200$  GeV minimum bias  $p + p$  data.

decay. The selections applied to identify an  $\Omega$  baryon signal are, however, more stringent.

Because both the  $p + p$  and  $d+Au$  data sets had barely enough  $\Xi$  baryon candidates for a correlation study, no  $\Omega$  baryon correlations were attempted, and thus no reconstruction of the  $\Omega$  candidates in those two data sets was done. In Au+Au data the situation was different, and enough  $\Omega$  baryon candidates were produced in order to see a correlation.

### 3.3 $\Xi$ and $\Omega$ baryons correlation candidates

#### 3.3.1 $p + p$

Loose geometrical and  $\Lambda$  mass cuts (Table 3.3) were applied to find both the  $\Xi^-$  and its antiparticle in the minimum bias  $p+p$  data set. The looseness of the cuts for the selected  $p_T$  range (2 GeV/c and above) allows for a 10% increase in reconstruction efficiency compared to cuts applied to the entire  $\Xi$   $p_T$  range [46]. The drawback of loosening the selections is the slight increase in background (B) under the signal (S)

Cut Parameter	Cut Value
$dca \Xi$ to PVx	$< 2.0$
$dca$ bach. to PVx	$> 0.6$
$dca \Lambda$ to PVx	$> 0.1$ and $< 1.5$
$dca$ p and $\pi$ to PVx	$> 0.6$
$dca$ p to $\pi$ -daug.	$< 1.0$
$dl \Xi$	$2 - 20$ cm
$dl \Lambda$	$3 - 300$ cm
mass $\Lambda$	$\pm 0.005$ GeV/ $c^2$
nHits bach.	$\Rightarrow 15$
nHits p	$\Rightarrow 30$
nHits $\pi$	$\Rightarrow 15$
N. $\sigma_{dE/dx}$ bach.	3
N. $\sigma_{dE/dx}$ p	3
N. $\sigma_{dE/dx}$ $\pi$ -daug.	3

Table 3.3: Selection parameters for  $\Xi^-$  and  $\Xi^+$  baryons with ( $p_T > 2$  GeV) in  $\sqrt{s} = 200$  GeV  $p + p$  minimum bias data.  $dca$  stands for “distance of closest approach”,  $dl$  stands for “decay length,” “bach.” stands for *bachelor*, “daug.” for “daughter,” and “PVx” is the abbreviation of “primary vertex.”

peak, as seen in Figure 3.4. The S/B for the resultant peak is found to be 4.6.

A tight cut around the  $\Xi$  mass peak between  $1.312$  GeV/ $c^2$  and  $1.330$  GeV/ $c^2$  selects the  $\Xi$  candidates for correlation. Fitting the signal with a Gaussian and a constant background yields  $S = 772 \pm 31$  and  $B = 168 \pm 23$ . Since the number of counts in the selected mass region varies slightly from fit values, the actual number of trigger particles was 972. Only 232 of these were correlated, as for the others there were no suitable correlation candidates in the same event.

### 3.3.2 $d+Au$

In  $d+Au$  data the collisions are no longer nucleon-on-nucleon, but rather nucleus-on-nucleus. Therefore, nuclear effects, such as the Cronin effect, initial state shadowing, and re-scattering are present. The  $d+Au$  collision environment is not as clean as in  $p+p$  collisions; however, the event multiplicity is higher and the  $\Xi$  statistics are much more abundant.

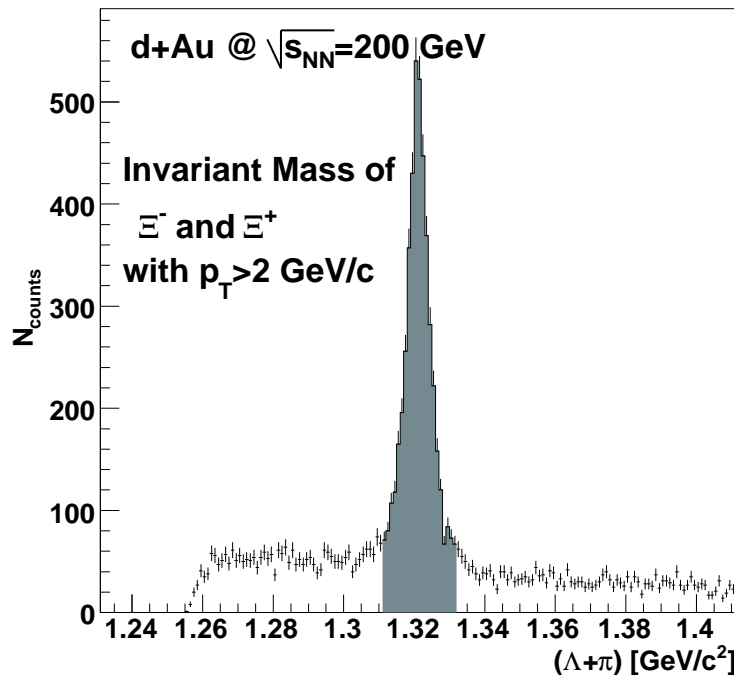


Figure 3.5: The invariant mass of  $\Xi^-$  and  $\Xi^+$  baryons (with  $p_T > 2$  GeV/c) in  $\sqrt{s_{NN}} = 200$  GeV  $d+Au$  data.

Applying a tighter set of cuts than the one used in the  $p+p$  data set (Table 3.4), a mass peak with 4986 correlation candidates is obtained, both  $\Xi^-$  and  $\Xi^+$  baryons, as shown in Figure 3.5. Using the bin method counting (the background on both sides of the peak is normalized and subtracted from the peak range), we find the signal to noise ratio in this data is 3.2.

### 3.3.3 Au+Au

#### a. $\Xi$

$\Xi$  baryon and  $\Lambda$  daughter decay length are highly correlated and dependent on the parent particle momentum. Therefore, a correlated decay length cut was applied, following the method described in detail in Reference [47]. The cut parameters are defined in Table 3.5.

The invariant mass of trigger candidates with  $2.5 < p_T < 4.5$  GeV/c selected for

Cut Parameter	Cut Value
$dca$ $\Xi$ to PVx	$< 0.6$
$dca$ bach. to PVx	$> 0.25$
$dca$ $\Lambda$ to PVx	$> 0.1$ and $< 1.5$
$dca$ p and $\pi$ to PVx	$> 0.7$
$dca$ p to $\pi$ -daug.	$< 1.0$
$dl$ $\Xi$	$2.4 - 20$ cm
$dl$ $\Lambda$	$2.5 - 35$ cm
mass $\Lambda$	$\pm 0.005$ GeV/c <sup>2</sup>
nHits bach.	$\Rightarrow 15$
nHits p	$\Rightarrow 30$
nHits $\pi$	$\Rightarrow 15$
N. $\sigma_{dE/dx}$ bach.	3
N. $\sigma_{dE/dx}$ p	3
N. $\sigma_{dE/dx}$ $\pi$ -daug.	3

Table 3.4: Selection parameters for  $\Xi^-$  and  $\Xi^+$  baryons with  $p_T > 2.0$  GeV/c in  $\sqrt{s_{NN}}$  d+Au data.  $dca$  stands for “distance of closest approach”,  $dl$  stands for “decay length,” “bach.” stands for *bachelor*, “daug.” for “daughter,” and “PVx” is the abbreviation of “primary vertex.”

correlations is shown in Figure 3.6. The colored band denotes the invariant mass region where the particles were selected for correlations. The same cuts were applied to all five  $p_T$  trigger ranges, where a correlation signal was obtained (see Chapter 4).

## b. $\Omega$

In order to see the  $\Omega$  signal, more stringent selections than those used for  $\Xi$  baryons, must be applied. The signal in 0-10% central Au+Au collisions (at  $|\eta| < 0.75$ ), as barely visible after the initial filtering, is shown in Figure 3.7. The blue band denotes the invariant mass region where an  $\Omega$  mass peak is expected.

We then apply cuts optimized to gain as much  $\Omega$  baryon signal as possible, while keeping the background under 30%. The cuts are listed in Table 3.6. Once again, we used a correlated cut to reduce the background in the most optimal way possible. The  $dca$  of the daughter  $\Lambda$  is closely related to the  $dca$  of the parent  $\Omega$ . The decay

Cut Parameter	Cut Value
$dca \Xi^-$ to PVx	$< 0.4$
$dca$ bach. to PVx	$> 1.5$
$dca \Lambda$ to PVx	$> 0.1$
$dca \Lambda$ to bach.	$< 0.7$
$dca$ p to $\pi$ -daug.	$< 0.7$
$dl \Xi^-$	$\Rightarrow 5$
$dl \Lambda$	$> 23 - 4 \times dl \Xi^-$
mass $\Lambda$	$\pm 0.007 \text{ GeV}/c^2$
nHits bach.	$\Rightarrow 25$
nHits p	$\Rightarrow 25$
nHits $\pi$	$\Rightarrow 25$
N. $\sigma_{dE/dx}$ bach.	3
N. $\sigma_{dE/dx}$ p	3
N. $\sigma_{dE/dx}$ $\pi$ -daug.	3

Table 3.5: Selection parameters for  $\Xi^-$  and  $\Xi^+$  baryons in  $\sqrt{s_{NN}} = 200 \text{ GeV}$  0-10% central Au+Au data.  $dca$  stands for “distance of closest approach”,  $dl$  stands for “decay length,” “bach.” stands for *bachelor*, “daug.” for “daughter,” and “PVx” is the abbreviation of “primary vertex.”

daughter cannot be closer to the vertex than the parent particle. Thus, using the technique developed in Reference [48], we use

$$dca \Lambda = c_1 + c_2 \sqrt{dca \Omega} \quad (3.4)$$

to cut away the extraneous background, shown under the curve in Figure 3.8.

Finally, we obtain a 65% pure signal with 4571 correlation candidates, shown in Figure 3.9, which we then use to construct a correlation. Once again, the blue band denotes the boundaries of the signal, accepted for triggering.

### 3.4 Constructing a correlation function

The correlation function is made up of as many correlated pairs as the data set allows. The pair is made of *trigger* and *associated* particles. In our study the *trigger* particle is the multi-strange baryon: its presence in the event in a certain  $p_T$  range of the

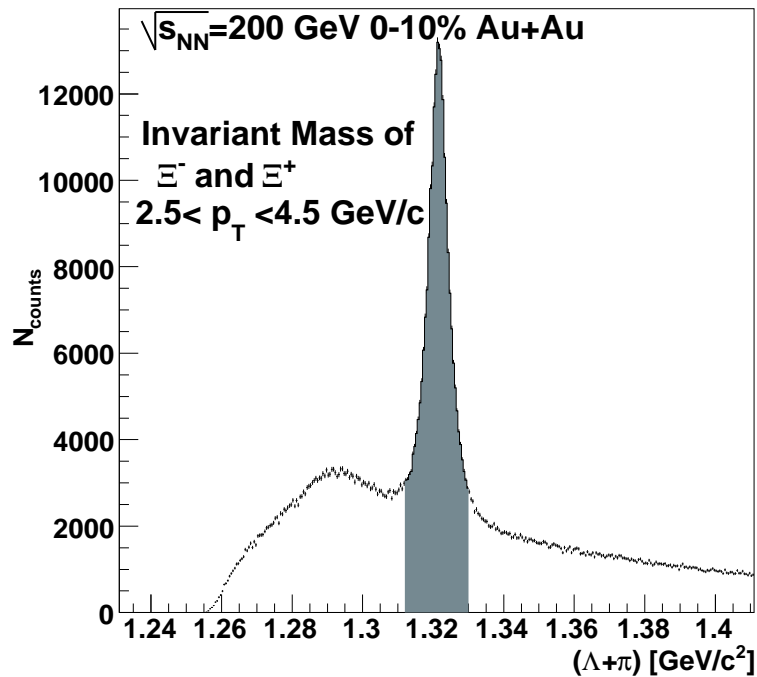


Figure 3.6: The  $\Xi$  baryon invariant mass peak in  $\sqrt{s_{NN}} = 200$  GeV 0-10% central Au+Au collisions used for correlations measured with  $2.5 < p_T\text{-trigger} < 4.5$  GeV.

single particle spectrum triggers the search for the *associated* partner. The trigger particle is assumed to be the leading particle of a jet, thus its  $p_T$  is always higher than that of the associated particle. In order to make comparisons across different data sets and various particle species, we normalize each of the correlation functions by the appropriate number of triggers. It is important to keep in mind that there are cases in low-multiplicity events where a correlation partner is not always available for every trigger particle, and thus the number of correlation pairs can be smaller than the number of triggers. It is also possible that in high multiplicity environments the number of tracks associated with each trigger is very high, and the ratio of trigger particles to associated ones is much less than 1.

Now that we have established what a trigger and an associated particle are, we proceed to describing how to construct a correlation function by computing the individual  $\Delta\phi$  values.

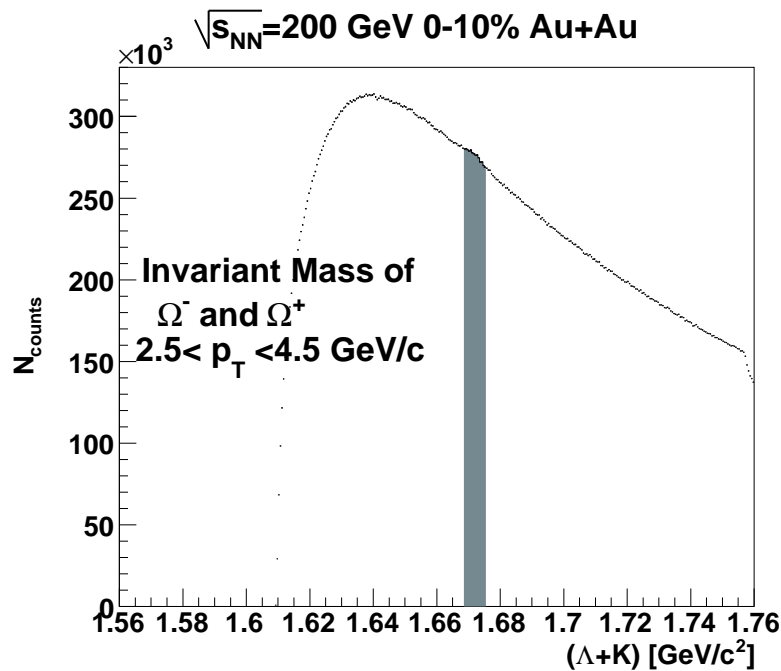


Figure 3.7:  $\Omega$  baryon (at  $2.5 < p_{+T} < 4.5$  GeV/c) signal in Au+Au central data after the initial filtering cuts.

- First, we check that both the trigger and the associated particles fall within the specified  $p_T$  range.
- The trigger baryon must be a primary, i.e., the projection of its helix to the primary vertex must pass within the resolution of the vertex position. The associated charged track also must be a primary, i.e., include the primary track as one of its fit points and have its helix projection within 1 cm of the primary vertex.
- In the case of  $p + p$  or  $d + \text{Au}$  events, baryon daughter tracks and the associated track are traced to the appropriate CTB hits.
- We must ensure that the associated particle is not a daughter track of the trigger baryon. This is done by comparing the track identification numbers (track IDs) and rejecting the associated track if its ID matched with any of the daughter

Cut Parameter	Cut value
mass of $\Xi$	1.311-1.331
$dca$ $\Omega$ to PVx	$< 0.6$
$dca$ Bach to PVx	$> 0.1 + 1.6 \times \sqrt{dca\Omega \text{ to } PV}$
$dca$ $\Lambda$ to PVx	$> 0.1 + 1.8 \times \sqrt{dca\Omega \text{ to } PV}$
$dca$ $\Lambda$ to $K^\pm$	$< 0.5$
$dca$ $\pi$ to $p$	$< 0.3$
$dl$ $\Omega$	3.2
$dl$ $\Lambda$	3.2
mass of $\Lambda$	$\pm 0.007 \text{ GeV}/c^2$
Hits bach.	$\Rightarrow 30$
N. Hits baryon	$\Rightarrow 30$
N. Hits daug. meson	$\Rightarrow 25$
N. $\sigma_{dE/dx}$ bach.	3
N. $\sigma_{dE/dx}$ baryon	3
N. $\sigma_{dE/dx}$ daug. meson	3

Table 3.6: Omega cut parameters used to obtain the particles in the Au+Au correlation function.  $dca$  stands for “distance of closest approach”,  $dl$  stands for “decay length,” “bach.” stands for *bachelor*, “daug.” for “daughter,” and “PVx” is the abbreviation of “primary vertex.”

track IDs.

- The helix of the trigger baryon is calculated and projected to the primary vertex. The  $p_T$  and the angle of the helix at the primary vertex are calculated and recorded.
- The  $p_T$ -directional angle of the associated track at the primary vertex is calculated.
- The STAR coordinate system stores the  $\phi$  coordinate of tracks as a number between  $+\pi$  and  $-\pi$ . In order to calculate a the difference between the trigger and associated angle that would span an interval of  $2\pi$ , both angles are mapped into an interval between 0 and  $2\pi$ .
- The difference between the associated and the trigger particle angles at primary vertex is calculated.

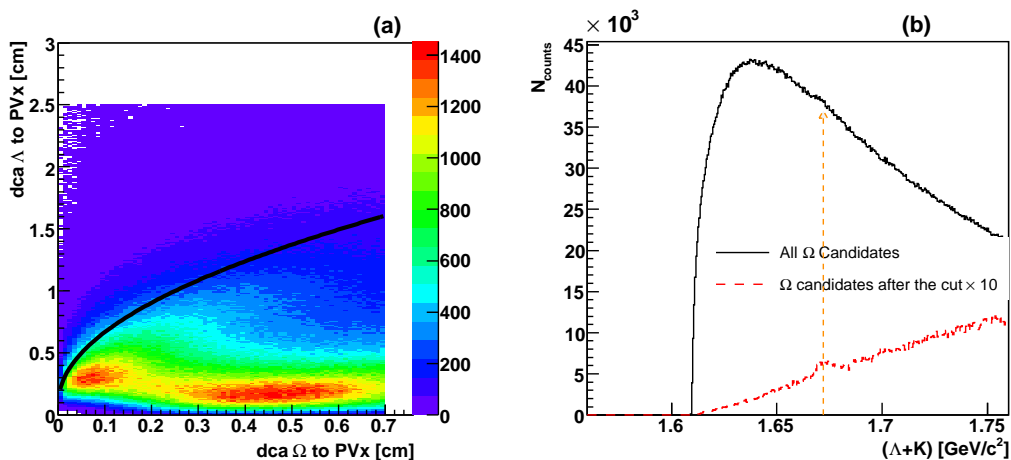


Figure 3.8: (a) Correlated background of  $\Omega$  baryons. The  $x$ -axis show the  $dca$  of the  $\Omega$  baryon to the primary vertex, while the  $y$ -axis show that for the  $\Lambda$  daughter. The  $\Omega$  baryon signal is located above the black curve, most of the signal below the curve is noise. (b) The black curves shows the  $\Omega$  signal before analysis-level cuts. The red dashed curve shows the  $\Omega$  signal after the correlated cut is applied. The dashed orange arrow guides the eye to the PDG [1] value of the  $\Omega$  invariant mass.

- The result is converted back into the  $-\pi$  to  $+\pi$  system.

This process is illustrated in Figure 3.10. The grey solid curve represents the  $\Xi$  baryon, while the green curves represent the daughter tracks seen in the TPC volume (the inner radius of the TPC corresponds to the dotted grey circle). The associated track is represented by a burgundy curve. The directions of azimuthal angles of the trigger and associated particles at the primary vertex are marked by dotted black arrows. Finally,  $\Delta\phi$  is denoted by the red dotted arc.

## 3.5 Correcting for detector acceptance

### 3.5.1 Mixed events correction

No detector has perfect acceptance, and STAR is no exception. Although the TPC is spherically symmetric, its acceptance in azimuth is not, as seen on Figure 3.11, which shows the azimuthal angle  $\phi$  and pseudo-rapidity  $\eta$  distributions of charged

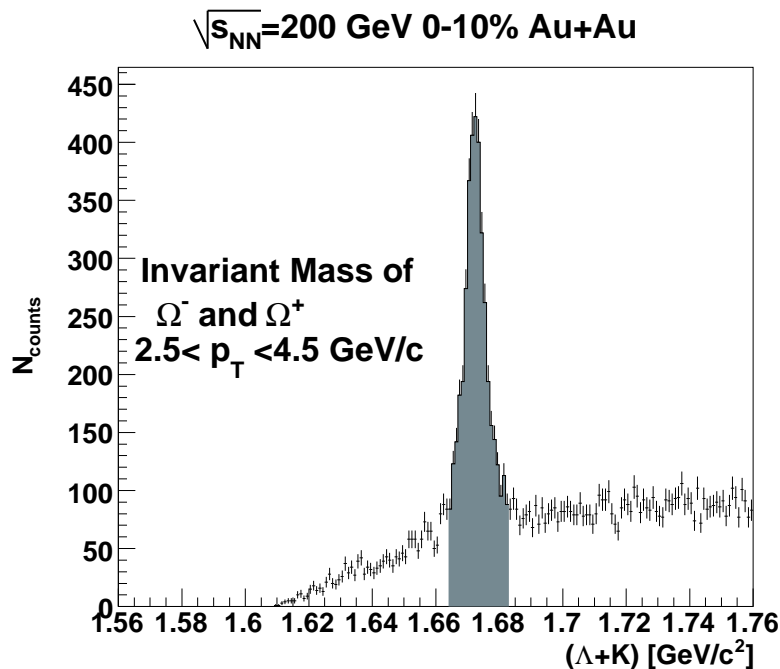


Figure 3.9: The final  $\Omega$  baryon invariant mass peak in  $\sqrt{s_{NN}} = 200$  GeV 0-10% central Au+Au collisions used for correlations.

tracks with transverse momentum  $p_T > 1.5$  GeV/c. Information is lost as tracks cross the sector boundaries, and correlation pairs are lost due to this sector-boundary crossing as well. The acceptance in  $\eta$  is also limited and thus non-uniform for detected correlation pairs. The acceptance of pairs with large differences in pseudo-rapidity is different (more limited) than the acceptance of pairs with smaller  $\Delta\eta$ . The result of the limited  $\phi$  acceptance is the jagged shape of the azimuthal correlation, the result of a nonuniform acceptance in pseudo-rapidity is the underlying triangular background in  $\Delta\eta$ .

We correct for the detector acceptance by constructing mixed event correlation functions in both  $\eta$  and  $\phi$ . The method uses actual tracks, both trigger and associated, pooled across a homogenous event sample and randomly selected to form a correlation. This method allows us to do the correction on-the-fly, with the exact specification of particles used in constructing the real correlation. One disadvantage of the technique

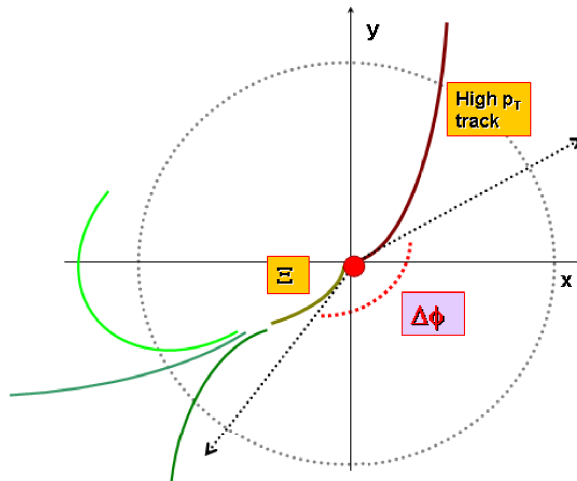


Figure 3.10: Calculating the  $\Delta\phi$  between a  $\Xi$  baryon and a charged track: the red circle in the center is the primary collision vertex, the green curves represent the  $\Xi$  baryon and its decay products seen in the TPC (the inner TPC radius is marked by the grey dotted circle). The burgundy curve represents a primary charged track seen in the TPC. The black dotted lines denote the direction of the azimuthal angles of the trigger and associated particles at the primary vertex. The red dotted arc shows the calculated  $\Delta\phi$ .

is that if the statistics are low, as is the case with the  $\Omega$  baryon correlation, this technique leads to over-sampling. Thus, we were able to correct one  $\Xi$  correlation function using the mixing in  $\eta$ , but not the  $\Omega$  functions.

A typical mixed event azimuthal correlation function is shown for  $\Omega$  and  $\Xi$  in Figure 3.12. There are twelve sectors in the TPC, which correspond to the highest points on the figure, and there are 12 sector boundaries. These correspond to the troughs in the graph.

Figure 3.13 shows the function used to correct a two-dimensional  $(\Delta\phi - \Delta\eta)$   $\Xi$  baryon correlation function. The function is normalized to the top of the "triangle," shown in Figure 3.13a, while Figures 3.13b and 3.13c show the projections of the normalized mixed events function in  $\Delta\phi$  and  $\Delta\eta$  directions respectively.

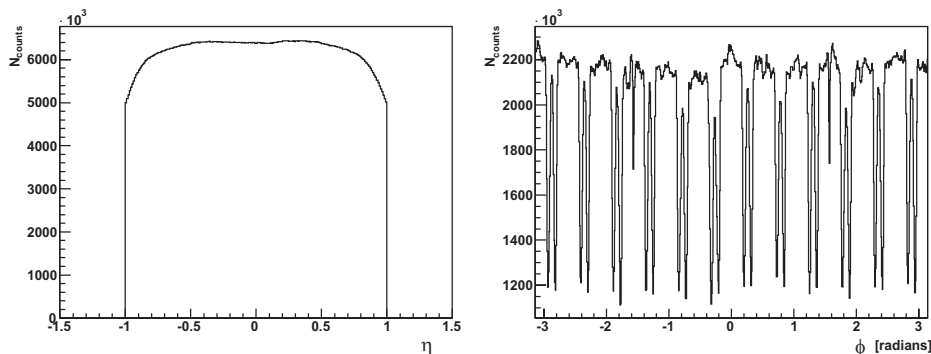


Figure 3.11: Raw distributions of associated tracks in (a) pseudo-rapidity  $\eta$  and (b) the azimuth,  $\phi$ .

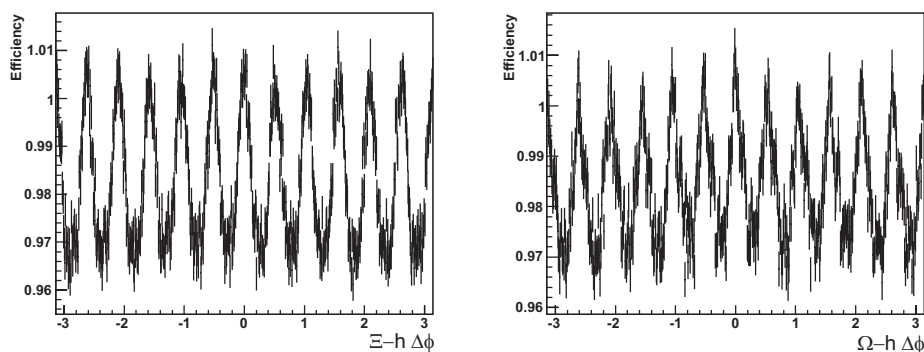


Figure 3.12: Mixed events correlation functions. (a)  $\Xi$  baryon mixed tracks correlation function (b)  $\Omega$  baryon mixed tracks correlation function.

### 3.5.2 Associated track efficiency correction

The loss of correlation pairs is not the only effect of the imperfect detector acceptance. The efficiency of reconstructing associated tracks depends on the number of track hit points left in the TPC and the track curvature, i.e., its momentum. In the  $p + p$  data set, due to the low multiplicities of the collisions, track reconstruction efficiency was very high, and its effect on the correlation function was negligible. The  $d + \text{Au}$  studies have also shown a uniform acceptance at 89%. The situation was different in the Au+Au data. Due to the high occupancy of the detector, the efficiency of track reconstruction very much depended on the  $p_T$  of the track, as seen

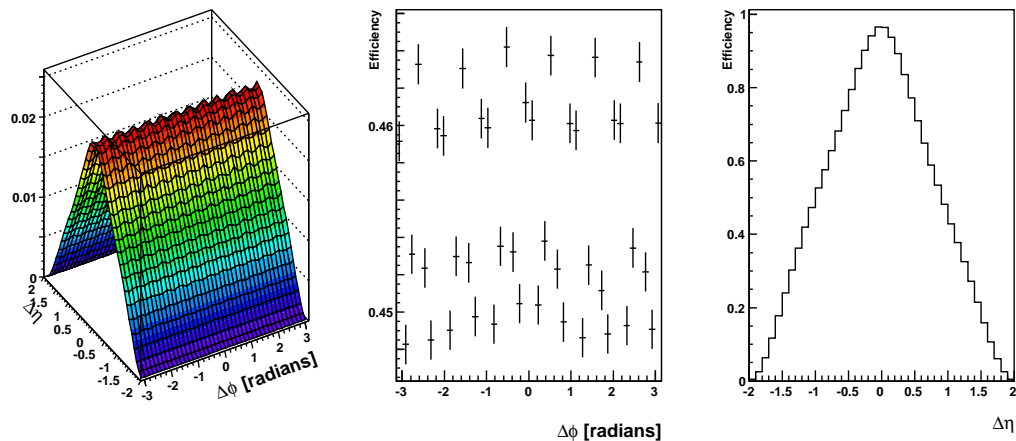


Figure 3.13: 2-dimensional detector acceptance function (a), projected into the  $\Delta\phi$  direction (b), projected into  $\Delta\eta$  direction (c).

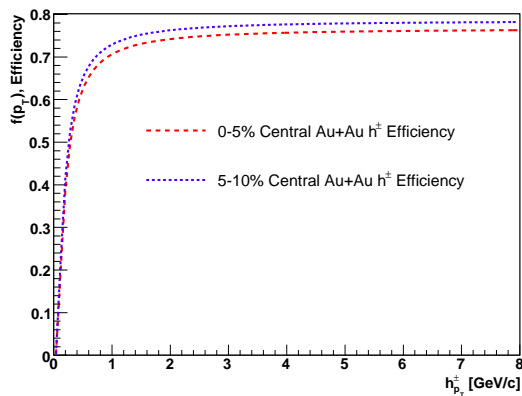


Figure 3.14: Charged track finding efficiency in two Au+Au centrality bins. The red dashed line shows the efficiency function in 0-5% central Au+Au collisions, while the blue short-dashed function shows the efficiency as a function of  $p_T$  in 5-10% central Au+Au collisions.

in Figure 3.14. This figure shows a result of a track efficiency study, performed using a Monte-Carlo simulation and a full GEANT (detector simulator tool) reconstruction of a track embedded in a real Au+Au event. This efficiency function is different in each collision centrality, and is shown here for 0-5 and 5-10% central events only. As expected, with increased centrality (and therefore event multiplicity), the track-finding efficiency falls. The lowest efficiencies are in the lower  $p_T$  region, below  $p_T$  of

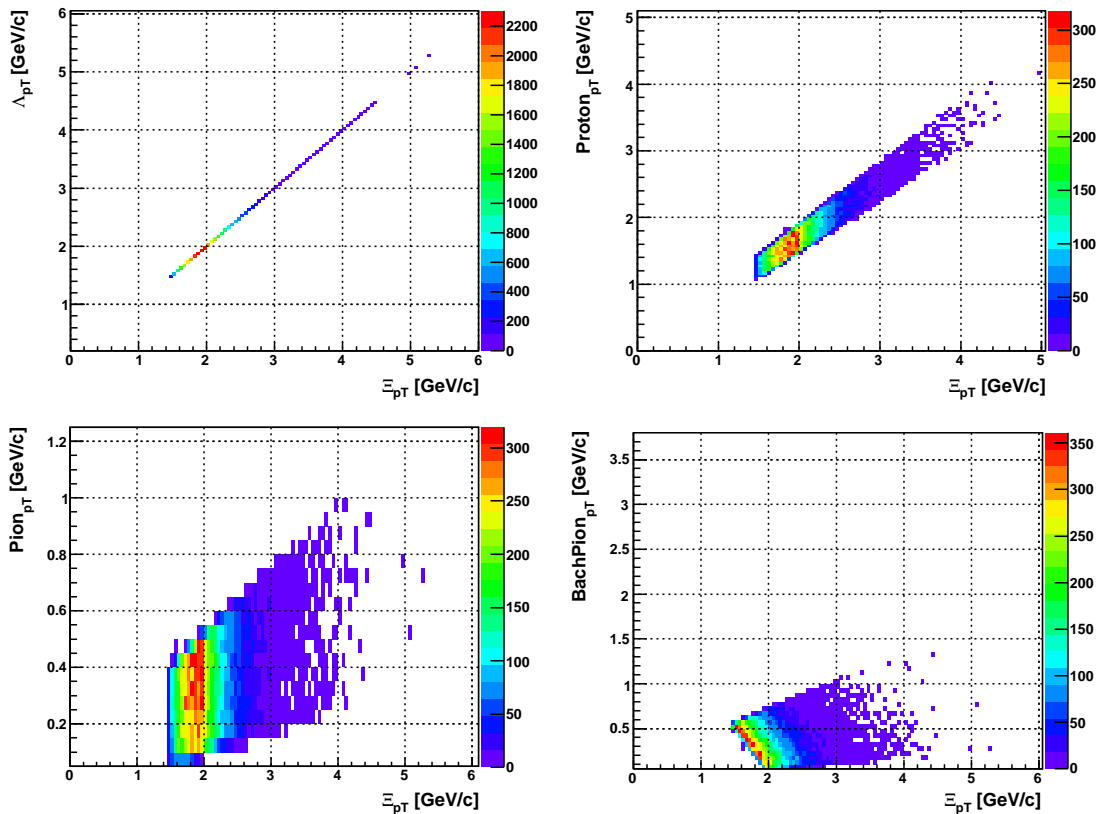


Figure 3.15: A Monte-Carlo simulation of a  $\Xi^-$  decay in vacuum. The  $x$ -axis shows the transverse momentum of the parent  $\Xi$  baryon, while the  $y$ -axis show (starting clockwise from the left)  $p_T$  of  $\Xi$  baryon  $\Lambda$  daughter,  $p_T$  of the daughter proton,  $p_T$  of the bachelor pion, and the  $p_T$  of the daughter pion.

1.0 GeV/c. Above a  $p_T$  of about 2.5 GeV/c, the efficiency function is nearly constant. The parameterizing function used to plot these curves in Figure 3.14 is as follows [49]:

$$f(p_T) = a_n e^{-\frac{b_n}{p_T} c_n} \quad (3.5)$$

Thus, when the correlation function was constructed in Au+Au, each correlation point was weighted by the efficiency  $f(p_T)$ .

## 3.6 Monte-Carlo Simulations

In order to better understand the kinematics of the  $\Xi$  and  $\Omega$  decay, we perform a simple Monte-Carlo simulation of  $\Xi^-$  decays in vacuum. The simulation result, shown in Figure 3.15, shows that most energy taken away from the collision point is taken by the daughter proton. The bachelor pion and the  $\Lambda$  daughter pion take away a negligible amount. The parent particles selected for this simulation were between 2 and 10 GeV/c in  $p_T$ . Another important piece of information gained by performing this simulation is that the  $\Lambda$  baryon takes virtually all of the  $\Xi$  baryon momentum. Subsequently, when the  $\Lambda$  baryon decays, all of that energy is passed into the proton. Thus, it is likely that both the  $\Lambda$  daughter and the daughter proton look primary, and might be used in  $\Lambda$  and proton correlations. Also, in addition, we note that the momentum of the bachelor meson is too small to be considered for high  $p_T$  correlations (it is consistently below 1 GeV/c, even for parent particles with  $p_T = 10$  GeV/c), and thus any correlation studies performed with  $\Lambda$  baryons or protons exclude the extra  $\Lambda$  (proton) - bachelor meson correlation.

### 3.6.1 PYTHIA

In the initial stages of the analysis, we wanted to simulate the correlation signal using a hard scattering in  $p + p$  collisions. This was done using the PYTHIA 6.22 event generator [50].  $3.2 \times 10^7$  PYTHIA events were produced of which  $4.2 \times 10^5$  events had at least one  $\Xi^-$  and  $1.9 \times 10^3$  had at least one  $\Xi^-$  within  $y < |0.75|$  and with  $p_T > 2$  GeV/c. Performing the correlation analysis described above, one finds that with 1921  $\Xi$  trigger particles there are 705  $\Xi$ -charged hadron correlations, with 1.4 correlations per correlated particle. In other words, if a  $\Xi^-$  was correlated, more than a third of the time it correlated with more than one track in the same event. The resultant correlation is shown in Fig. 3.16, where a clear same-side and a distinct away-side peak are seen. The same-side peak obtained in this simulation contains 12% more correlations than the away-side peak, and is 33% higher.

Although correlations are observed in both the  $p+p$  data and that of simulated particles from PYTHIA, a comparison of the two spectra shows that the simulation

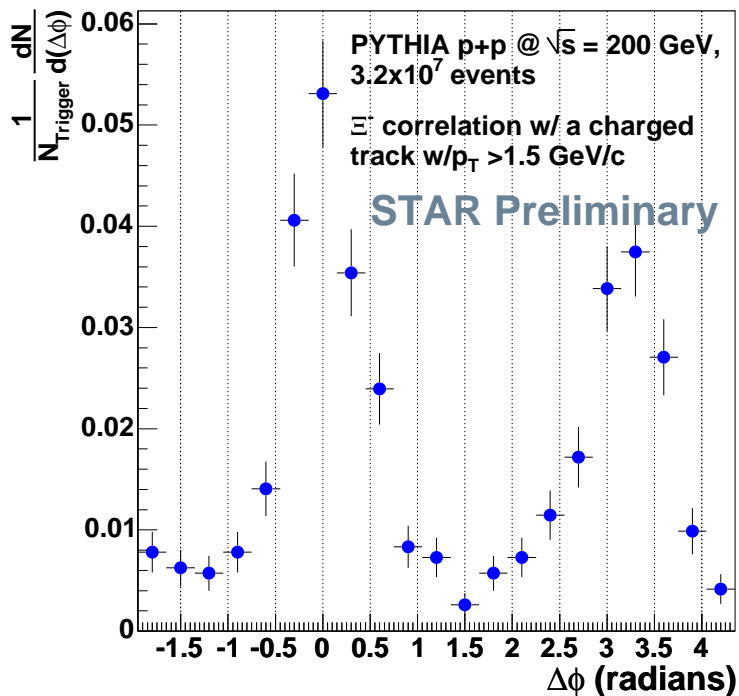


Figure 3.16:  $\Xi$ -charged track correlation function constructed using PYTHIA-generated particles.  $\Xi$  trigger  $p_T > 2$  GeV/c. The rapidity window used for both trigger and associated particles is  $|y| < 0.75$ .

does not reproduce the data. While the PYTHIA integrated yield is higher ( $dN/dy = 0.00318$  for PYTHIA,  $dN/dy = 0.00181 \pm 0.00008$  the  $p+p$  data [51]), it grossly underpredicts the yields in the region of interest ( $p_T > 2$  GeV/c), at the same time overstating the yields below  $p_T = 0.8$  GeV/c (Fig. 3.17). This might be altered by adjusting various PYTHIA parameters, such as tuning the hard processes parameters and allowing for parton rescattering, or making NLO pQCD calculations.

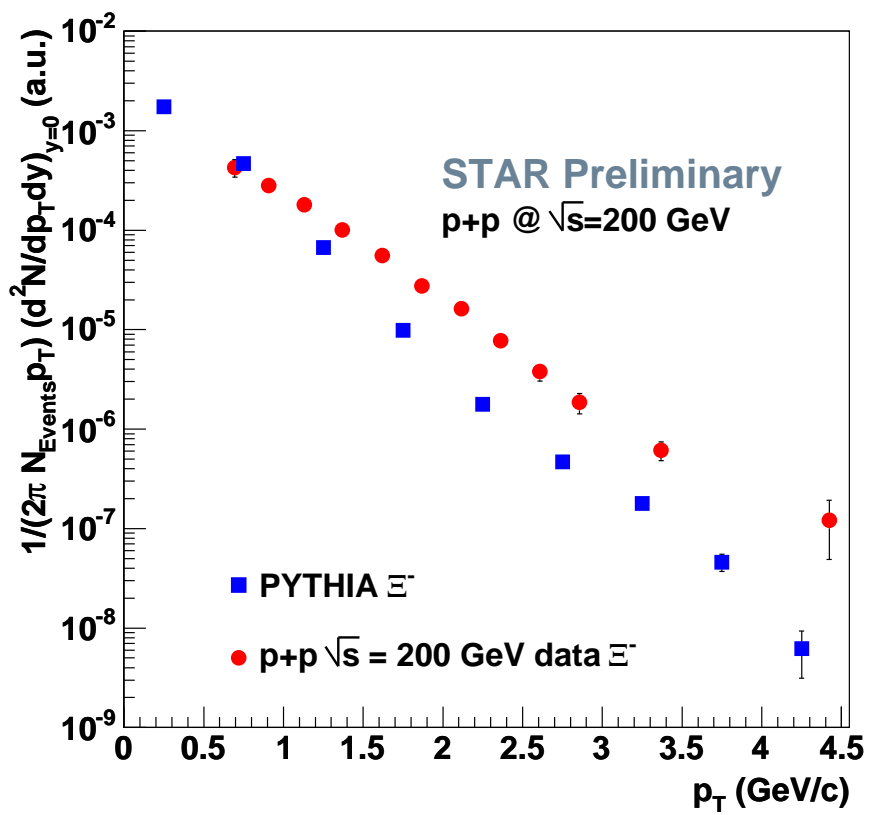


Figure 3.17:  $\Xi^-$  spectra from PYTHIA (blue points) and  $p+p$  minimum bias collisions (red points).

# Chapter 4

## Data Analysis

### 4.1 p+p

Obtaining multi-strange baryon correlations in  $p + p$  collisions presents several challenges. Firstly, because of the canonical suppression of the phase-space, production of strange particles is a relatively rare process. Secondly,  $p + p$  events on average have relatively low multiplicities, about 5 primary tracks per event. This, in conjunction with a three-particle final state decay of both  $\Omega$  and  $\Xi$  baryons, makes it difficult to find a suitable associated particle. Thus, the already scarce statistics are reduced even further.

Two different data sets, both at  $\sqrt{s} = 200$  GeV, were used to study production of multi-strange baryons in  $p + p$  collisions. One is a set of minimum bias data, the other was data triggered on energy deposits in the STAR EMC, the so-called high- $p_T$  triggered data set.

#### 4.1.1 Minimum bias $p + p$ collisions

The aim of this work is to study the mechanisms for strange baryon production in collision environments where the energy density ( $\epsilon$ ) and temperature ( $T$ ) are many times more than usual cold nuclear matter. In order to understand the effect of this extreme matter on fragmentation products, one must first study the fragmentation

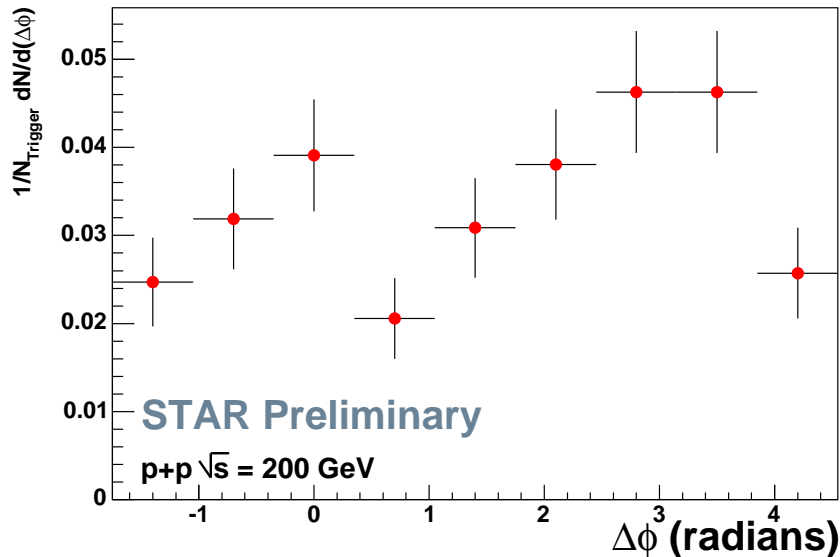


Figure 4.1:  $\Xi^\pm$ - $h^\pm$  correlations in Year 2002 minimum bias  $p + p$  data.

process in vacuum. Although it is possible to reconstruct a jet in a  $p + p$  collision, in Au+Au collisions at RHIC energies the full jet reconstruction is impeded by large background track multiplicities and small jet cross-sections. Instead, a statistical study of jets is employed. In order to be able to compare the data in the Au+Au data set to an in-vacuum reference (such as  $p + p$ ), the methods used in Au+Au were employed in the  $p + p$  data set as well. Therefore, the  $p + p$  events where there might be multi-strange baryon jets produced, were also analyzed statistically.

The strangeness production cross-section in  $p + p$  collisions is suppressed, as outlined in Chapter 1. Because of this canonical suppression, the chances of finding in this data a strange particle are slim, even less for a multi-strange particle. In the largest STAR  $p + p$  minimum bias data set only about 50  $\Omega^\pm$  baryons were found. The chances are slightly better for  $\Xi^\pm$  baryons: there were 3.0 charged  $\Xi$  baryons per 1000  $p + p$  minimum bias events. Only a fraction of these particles is suitable for correlations (using the criteria  $p_T > 2$  GeV/c). The majority are found with  $p_T < 2$  GeV/c. Moreover, once a valid  $\Xi$  baryon trigger is found for correlating, it has already accumulated over 3/5 of the available tracks of an average  $p + p$  event. This

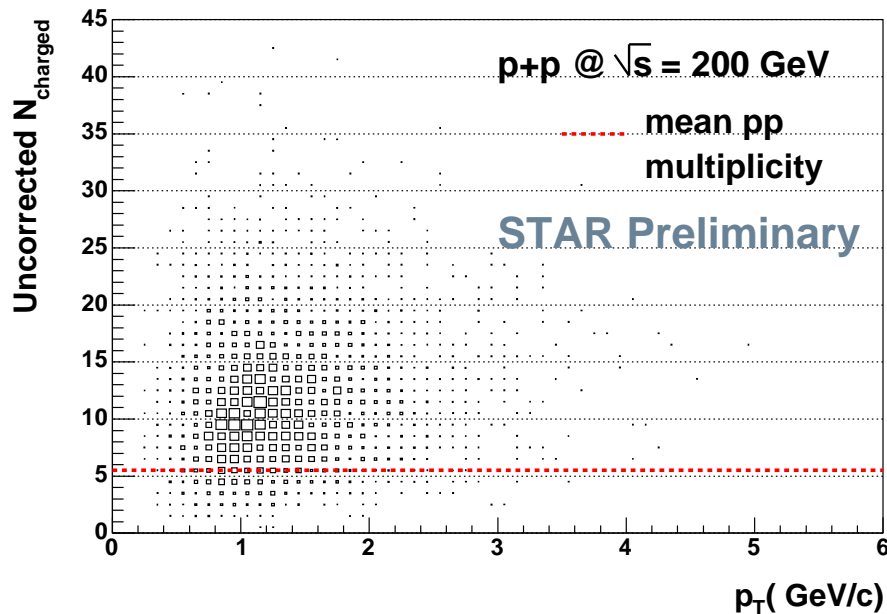


Figure 4.2: Reference event charged particle multiplicity as a function of  $p_T$  of the  $\Xi^\pm$ .

makes it less likely to find a correlation partner. In order to increase the likelihood of finding such a partner, the  $p_T$  of associated tracks was lowered to 1.5 GeV/c, with no upper transverse momentum cut-off. However, going this low in  $p_T$ -associated was still insufficient. Although 972 trigger  $\Xi$  baryons were found in this data set, only 297 correlations were possible. The resultant correlation function is shown in Figure 4.1.

If the trigger particle did have a suitable correlation partner, it was likely to have more than one in the same event. For each trigger particle that was correlated, there were 1.3 corresponding associated tracks in this data. Thus, a valid correlation is likely to select baryons produced in collisions with a higher number of high energy tracks, i.e., more violent  $p + p$  collisions.

There is little quantitative information available from the correlation found in  $p + p$ . Thus, indirect ways of studying multi-strange baryon formation mechanisms in this production environment were sought. A way to study strangeness production indirectly is to examine the quality of the events where strange baryons are produced. This is done in order to single out a particular signature or trend for production of these particles. One way of classifying a particle collision event is particle multiplicity.

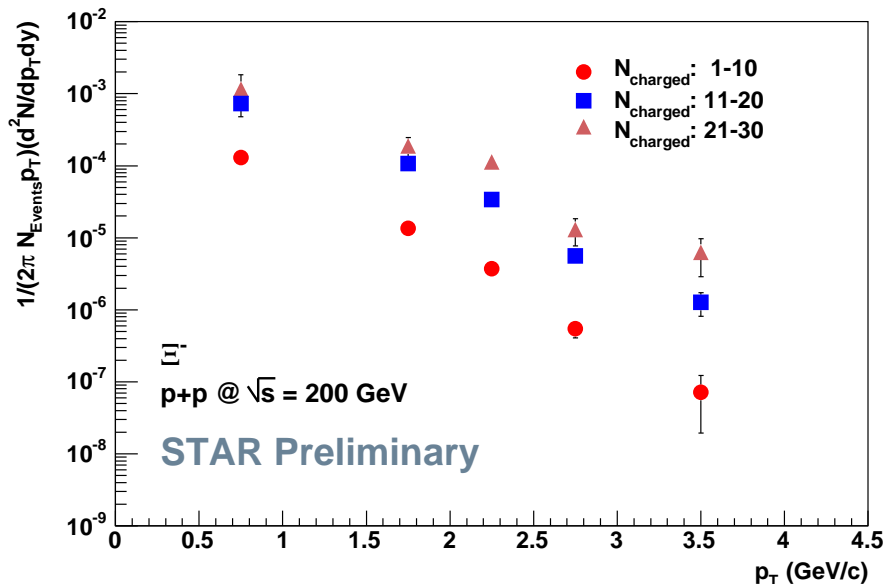


Figure 4.3:  $\Xi^-$  corrected spectrum in 3 event multiplicity bins.

Indeed, as we have seen, multi-strange particles tend to be produced in collisions where the number of tracks is larger than average. This is illustrated in Figure 4.2 and Figure 4.3. In Figure 4.2 we see that the average multiplicity of a collision where a  $\Xi$  is produced is more than twice as large as that of an average  $p+p$  collision. Figure 4.3 shows that the higher  $p_T$   $\Xi$  baryons also tend to be produced in high-multiplicity  $p+p$  collisions. This seems to be an overall trend for strange particles [46]. Since  $p+p$  collisions with enhanced multiplicities also correspond to jetty events [17], we hypothesize that multi-strange baryons above  $p_T = 2$  GeV/ $c$  threshold tend to be produced in jet-containing events.

#### 4.1.2 High-tower triggered events and trigger Bias

The unintended consequence of using an electro-magnetic calorimeter for triggering is that it may be used not only as a trigger for jet processes, but also to trigger on anti-baryons. The idea is simple. Matter is composed of atoms made of protons and neutrons; thus when an anti-proton comes in contact with matter, it annihilates, releasing its energy, plus the energy of the proton it destroys. When an anti-proton

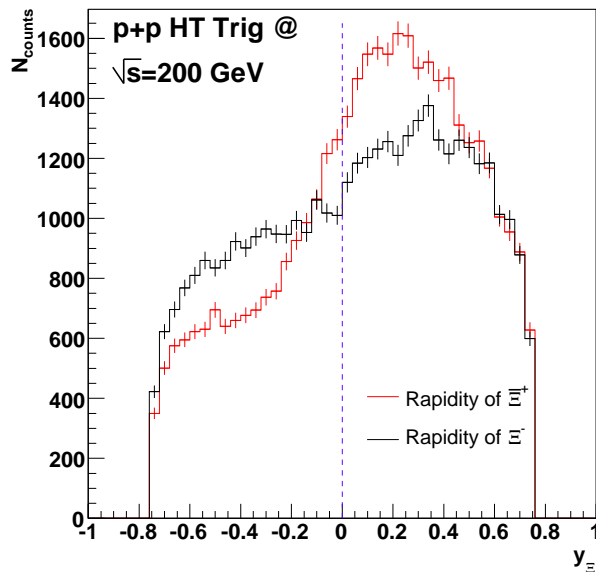


Figure 4.4:  $\Xi^-$  and  $\Xi^+$  rapidity distributions. The blue line guides the eye to the division between TPC volume equipped with the BEMC ( $y > 0$ ), and the part of the volume which was not ( $y < 0$ ).

reaches the EMC, the energy deposited in its annihilation is large enough to cause the event to be triggered and recorded on disk. Because the strange baryon number is conserved via the eventual decay into an (anti) proton, the anti-baryon spectra of strange baryons is enhanced in the high- $p_T$ -triggered events.

This is well-illustrated by looking at the rapidity distributions of identified  $\Xi$  baryons and anti-baryons in the high-tower triggered data, shown in Figure 4.4. Up to 2005, STAR only had 1/2 of its BEMC installed, and therefore the annihilation of the anti-particles was detectable also in only 1/2 of the detector volume. In the figure, we see that in the region of negative rapidities a typical particle-to-anti-particle ratio, with particles dominating over anti-particles. On the right side of the plot we see the result of triggering on the electro-magnetic calorimeter: although both particle counts are enhanced, the anti-particle is enhanced more. Thus, by using triggered data, we increase the probability of producing high  $p_T$   $\Xi$  baryons suitable for correlations, as seen in Figure 4.5.

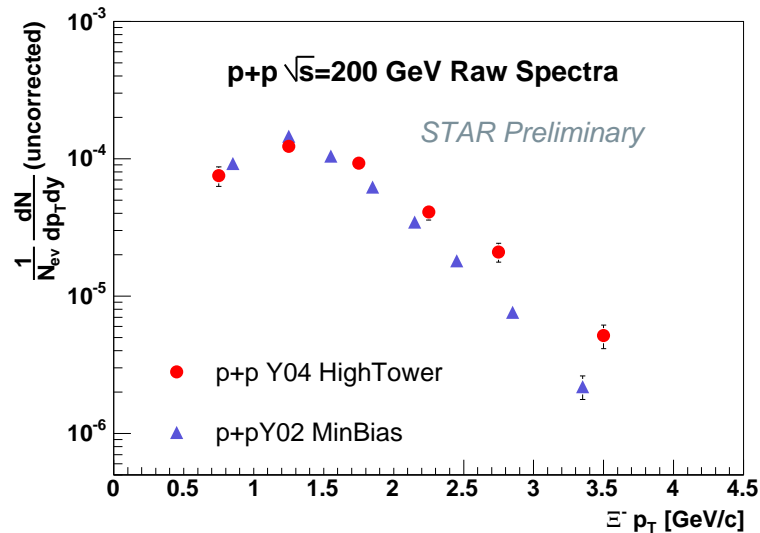


Figure 4.5: Uncorrected  $\Xi^-$  spectra: MinBias (blue triangles) and High-tower Triggered (red circles).

The high- $p_T$  triggered data set obtained in 2003 is much smaller than the min-bias data set taken the previous year. The former contains only 2M events, while the latter contains close to 14M. However, there are more  $\Xi^-$  baryons produced in the triggered data than in the min. bias set for  $p_T > 2$  GeV/c, thus increasing the  $\langle p_T \rangle$  of the  $\Xi^-$  spectrum. Therefore, triggering introduces a bias. To understand this bias, the difference between all min. bias events and those min. bias events where we reconstruct a  $\Xi$  baryon is examined. We also compare multiplicity distributions of the two data sets.

In the min. bias sample, as the multiplicity of the  $p + p$  collision increases, the  $\langle p_T \rangle$  of produced particles increases [52]. Fig.4.6 shows the difference in uncorrected charged primary track distributions between min. bias and high tower triggered events for  $|y| < 0.75$ . The mean of the former is  $5.86 \pm 0.01$  charged tracks, while the mean of the latter is  $11.94 \pm 0.01$ . When only min. bias events with a  $\Xi$  baryon are selected, the mean of the multiplicity distribution rises to  $12.12 \pm 0.05$ . Thus, events where a  $\Xi$  baryon is produced belong to the same multiplicity class as high-tower triggered events. It has been shown in [51] that the enhanced multiplicity of the  $p + p$  events

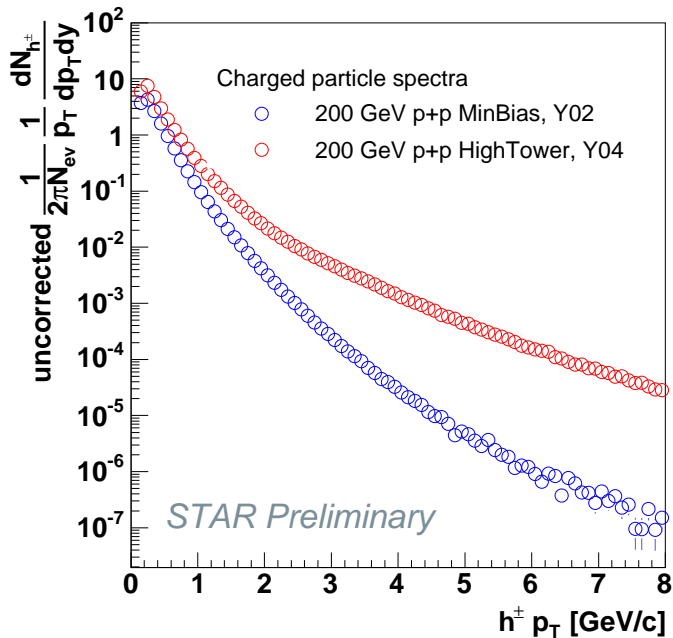


Figure 4.6: Uncorrected charged spectra: MinBias (blue) and High- $p_T$ -triggered (red).

corresponds to a higher event  $\langle p_T \rangle$ . We also know that jets can be detected by high energy deposits in electro-magnetic calorimeters. Therefore, we associate high  $\langle p_T \rangle$  events with jettiness [17], and can conclude that  $\Xi$  baryons are likely to be produced in jet events.

For further evidence of jettiness, we construct a correlation function using the available high- $p_T$  triggered baryons. To increase the statistics, the correlation function was folded around its jet axis,  $\Delta\phi = 0$  and  $\Delta\phi = \pi$ . The symmetry of the function follows from the symmetry of the jet-cone, but it can also be ascertained from Figure 4.8. The resultant correlation function, normalized by the number of triggers, is shown in Figure 4.9.

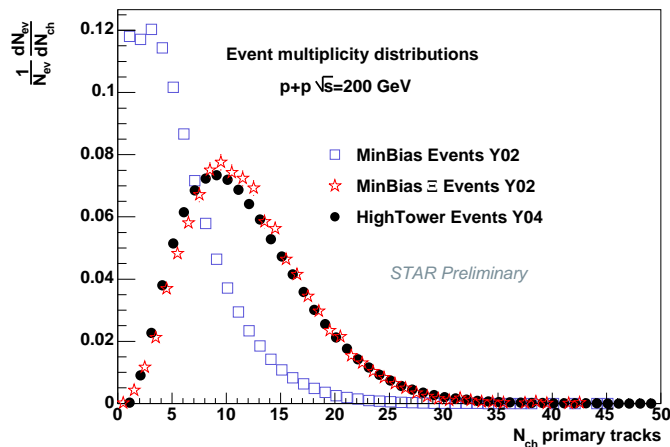


Figure 4.7: Multiplicity distributions of three event classes: blue open squares show the multiplicity distribution for minimum bias events, open red stars show the same for minimum bias events containing a  $\Xi^-$  baryon, and solid black circles represent the multiplicity distribution of all high-tower events

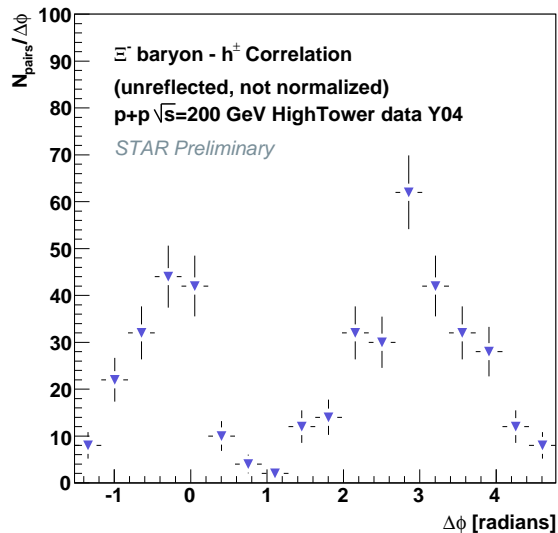


Figure 4.8: Raw  $\Xi^-$  baryon correlations with charged tracks in high- $p_T$  triggered data set.

## 4.2 d+Au

Another Au+Au reference to consider is the  $d$ +Au data set taken by STAR in 2003. Since the collisions are no longer nucleon-on-nucleon, but rather nucleus-on-nucleus,

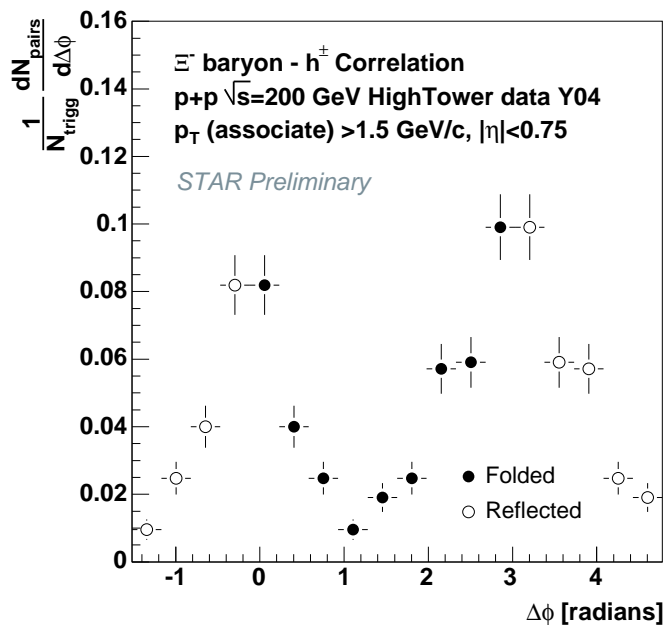


Figure 4.9: Normalized correlations:  $\Xi^-$  correlated with charged tracks.

nuclear effects such as the Cronin effect, initial state shadowing, and re-scattering are present. The  $d+Au$  collision environment is not as clean as in  $p+p$  collisions; however, the statistics are much more abundant.

Utilizing these statistics, and applying a tighter set of cuts than the one used in the  $p+p$  data set, a mass peak with over  $4 \times 10^3$  correlation candidates is obtained, as shown in Chapter 3. As before, there is a 2 GeV/c transverse momentum cut applied. Because we expect our background to be random, and the distribution of differences in azimuthal angles between a trigger and an associated track to be random, we fit two Gaussians plus a constant to the correlation function. As demonstrated in Figure 4.10, only 32% of correlated events had one primary track with sufficiently high  $p_T$ , the others had two or more tracks available for correlation. This is not surprising, since the mean multiplicity of a  $d+Au$  event is several times higher than that of a  $p+p$  collision.

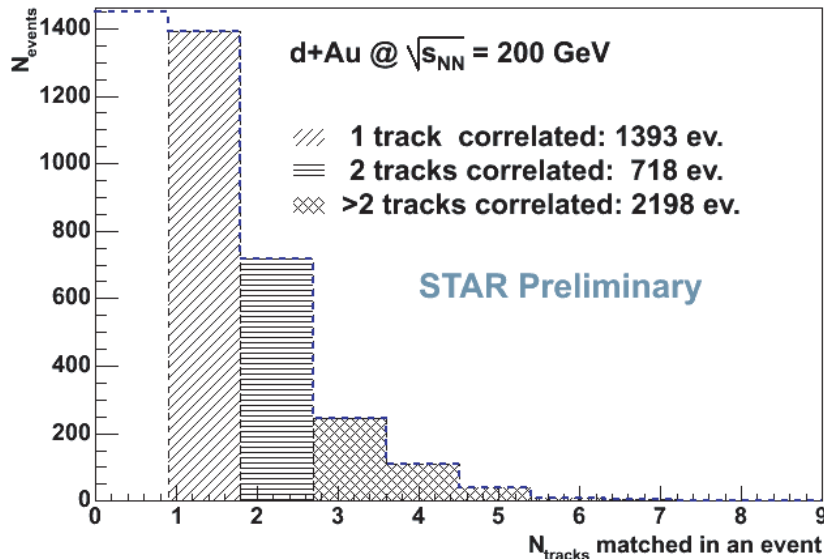


Figure 4.10: Number of uncorrected charged tracks per  $\Xi$  in an eligible  $\sqrt{s_{NN}} = 200$  GeV  $d+Au$  minimum bias event.

### 4.2.1 Correlations

Now we come to the correlation function in  $d+Au$ . As seen in Fig. 4.11, the  $d+Au$  data set has sufficient statistics to fit two emerging peaks. Contrary to what we saw in  $p+p$  PYTHIA simulations, and in line with the  $p+p$  data, the same-side peak is equal to or smaller than the away-side peak, which could be explained by depletion of the available high  $p_T$  tracks on the same-side by the  $\Xi$  decay itself, which uses up at least 3.3 GeV of the available jet-cone energy. The peaks in the  $d+Au$  correlation function have widths:  $\sigma_{\text{same}} = 0.517 \pm 0.17$  radians and  $\sigma_{\text{away}} = 0.75 \pm 0.16$  radians. The yield under the same-side peak is  $0.015 \pm 0.026$ , and the yield under the away-side peak is  $0.041 \pm 0.016$ .

## 4.3 Au+Au

Our main interest lies in understanding the strangeness production mechanisms in a dense, hot medium produced in high energy heavy ion collisions. Therefore, as

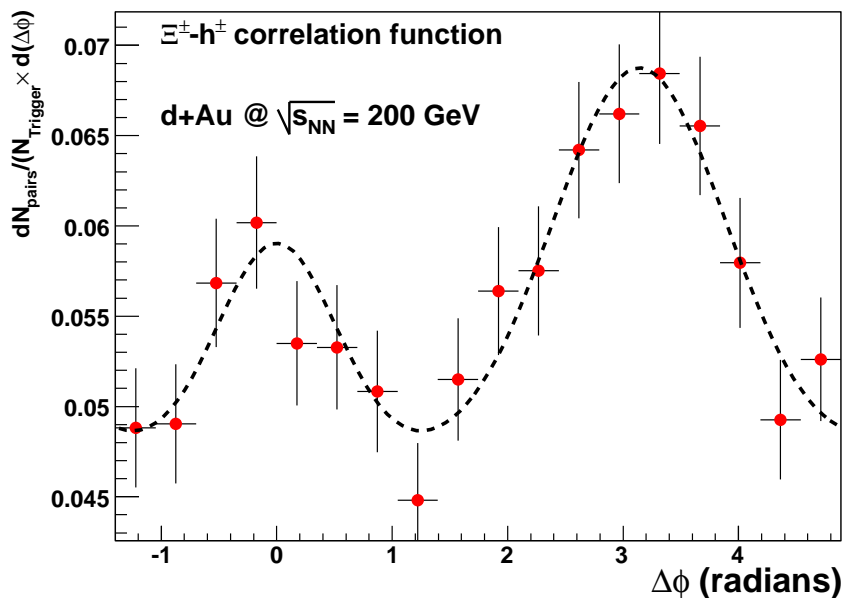


Figure 4.11: Azimuthal correlation function with  $\Xi^-$  and  $\Xi^+$  baryon triggers with  $p_T > 2$  GeV/c and associated tracks with  $1.5 < p_T < p_{T\text{-trigger}}$  in  $d+Au$  data.

mentioned earlier, the previous studies were done as a precursor to a study in Au+Au at  $\sqrt{s} = 200$  GeV data. In this section we will describe the study in Au+Au itself, which lies at the center of this dissertation.

STAR has taken two Au+Au data sets at top energy. One yielded a little over 1.5M central events, the second over 20M. For the analysis presented here only the second data set was used.

The outline of the procedure for obtaining the correlation is as follows (the details will be described after the outline):

1. As before, a raw correlation function is constructed from all available multi-strange baryons of a given species. Each entry is efficiency corrected for a given associated track availability, as described in the previous chapter.
2. The correlation function is corrected for the TPC sector boundaries and for the underlying triangular background in  $\eta$  using cross-event particle mixing.
3. The function is normalized by the number of trigger particles available and is

reflected about its axis of symmetry (around  $\phi = 0$ ).

4. The resultant function is used to determine the elliptic flow component underlying the correlation function using fits and the Zero Yield At Minimum (ZYAM) method.
5. Elliptic flow and the flat background are subtracted and the same-side jet+ridge yields are calculated. Alternatively, the jet yield is calculated using two different  $\eta$  regions, as described below.

### 4.3.1 Selection of associated tracks

To increase the statistics, the  $p_T$  of the tracks selected for correlations had a fixed lower cut-off (always 1.5 GeV/c), but a variable upper cut-off: the condition being that the momentum of the associated track should always be lower than the momentum of the trigger particle. The tracks are also selected to match the same rapidity interval as that of the multi-strange triggers,  $|\eta| < 1$ . The selected tracks also have been tracked as "valid" by the reconstruction software and are primary, i.e., their distance of closest approach to the primary event vertex is less than 1 cm.

### 4.3.2 Flow subtraction

The most significant background for any azimuthal correlation analysis comes from the second harmonic of the underlying collective flow of the event. This anisotropy is the result of the hydrodynamical expansion of the fireball, which manifests itself as collective flow of partons, and also the initial asymmetry of the geometry of the collision: if the overlap of the nuclei is not total, the collision region will not be spherically symmetric, as illustrated in Figure 4.12a.

As the reaction process unfolds, the initial anisotropy in coordinate space will result in the final anisotropy in the momentum space: particles prefer to leave the collision region in the direction where there is less matter due to the eccentric shape of the collision region. In other words, more partons will flow in the direction of the higher pressure gradient.

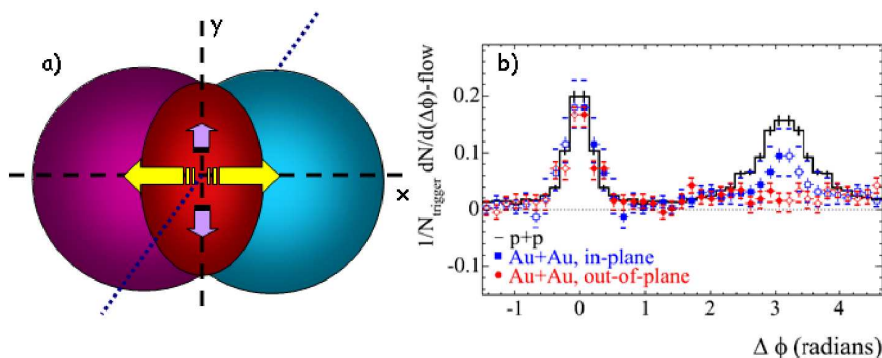


Figure 4.12: Two panels showing the physics of spatial asymmetry translated into momentum space anisotropy. (a) Cartoon representing a collision with non-zero impact parameter. The arrows represent the relative sizes of the pressure gradient in the fireball. The beam direction is denoted by the blue dotted line. (b) A figure taken from [53], showing charged-charge correlation functions in-plane (blue), where the away-side of the correlation is not completely suppressed, and out-of-plane (red), where the away-side of the correlation function is effectively zero.

One way to see this initial anisotropy is to turn to an in-plane/out-of-plane correlation analysis. The study measures the correlation functions for in-plane and out-of-plane particles separately. When complete, it shows that the "in-plane" (parallel to the x-axis in the cartoon in Figure 4.12a) away-side is significantly larger than the "out-of-plane" away-side. This is because it is harder for the away-side to escape the collision region in the out-of-plane direction (smaller pressure gradient) than in the in-plane direction. Thus, it indirectly confirms the hypothesis that there is an underlying flow of particles determined by the initial anisotropy of the collision and the subsequent density of the interaction region [53].

The collective flow structure can be described by decomposing the function of particle distributions with respect to the reaction plane in terms of Fourier coefficients,  $v_n$  [54]:

$$E \frac{d^3N}{d^3p} = \frac{1}{2\pi} \frac{d^2N}{p_T dp_T dy} \left\{ 1 + \sum_{n=1}^{\infty} 2v_n \cos[n(\phi - \Psi_R)] \right\} \quad (4.1) \quad (4.1)$$

In this expression,  $\phi$  stands for the azimuthal angle of a particle, and  $\Psi_r$  the

angle of that particle with respect to the reaction plane. The first harmonic of this expansion, characterized by coefficient  $v_1$ , is usually referred to as “directed flow,” the second harmonic, characterized by  $v_2$ , is called “elliptic flow” due to the underlying shape of the harmonic: an ellipse. Because the angle of the reaction plane is different for every collision, we turn to a variable common to all events regardless of their reaction plane orientation. This is  $\Delta\phi$ , the difference between azimuthal angles of any two particles in the same event. Using  $\Delta\phi$  we can accumulate and compare over many events of the same event class.

Unfolded in azimuth, the shape of the elliptic flow gives rise to two peaks at  $\Delta\phi = 0$  and  $\pi$ , at precisely the same locations where the back-to-back jet peaks (due to the narrow cone, usually associated with jets) are expected to be reconstructed. Thus obtaining the jet yield requires the subtraction of the elliptic flow component.

There are two methods of obtaining the second coefficient of the elliptic flow used at STAR. One method is usually referred to as the four-particle cumulant method. The other method involves calculating an approximation of the reaction plane, i.e., the plane of the collision, on which both the line parallel to the beam axis and the impact parameter segment lie, as illustrated by Figure 4.13.

The method to describe high- $p_T$  azimuthal correlations and their background has been nicely developed and described in [55]. In general, a correlation function constructed by calculating the difference in azimuthal angle of two particles is described by

$$\frac{dN_{pairs}}{d\Delta\phi} = B\left[1 + \sum_{n=1}^{\infty} 2p_n \cos(n\Delta\phi)\right] \quad (4.2)$$

where  $\sum_{n=1}^{\infty} 2p_n \cos(n\Delta\phi)$  is the Fourier decomposition of the the real part of  $e^{in(\phi_i-\phi_j)}$ ,  $p_n = \text{Re}\langle e^{in(\phi_i-\phi_j)} \rangle$ , and  $B$  is the amplitude of uncorrelated pair background (in  $d$ +Au collisions that was the only background). It is relatively straight-forward to show that

$$p_n = \text{Re}\langle e^{in(\phi_i-\phi_j)} \rangle = \text{Re}\langle (e^{in(\phi_i-\Psi+\Psi-\phi_j)}) \rangle \quad (4.3)$$

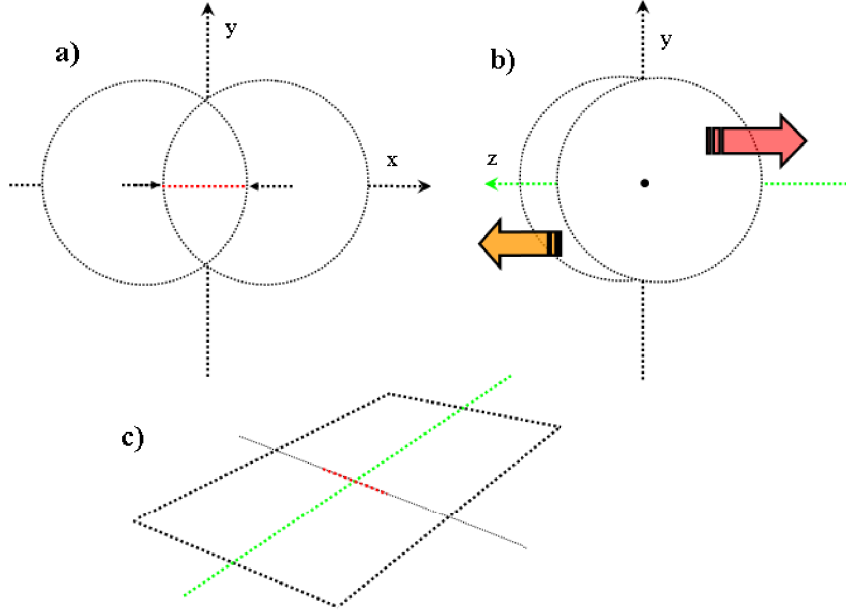


Figure 4.13: A schematic representation of the event plane. (a) This shows two schematically drawn nuclei moving in and out of the plane of the paper. The red dotted line then represents the distance between their centers, i.e., the impact parameter,  $b$ . (b) Here we see the same two nuclei, but from the side (in reality these would look like thin sheets, not circles). The  $z$ -direction is the axis parallel to the beam-line. (c) Two parameters defining collision's reaction plane: the direction of impact parameter (in this case parallel to the  $x$ -axis) and the beam-line axis.

If there were no fragmentation products forming a correlation, we would have eqn. 4.3 become  $p_N = \text{Re}\langle(e^{in(\phi_i-\Psi+\Psi-\phi_j)})\rangle = \text{Re}\langle(e^{in(\phi_i-\Psi)})\rangle\text{Re}\langle(e^{in(\phi_j-\Psi)})\rangle = v_n^i v_n^j$ , but since a jet signal is seen above that of the underlying flow,  $p_n = v_n^i v_n^j + c_n$ , so the ansatz for the correlation function then becomes:

$$C_n(\Delta\phi) = A_0 e^{-\frac{\Delta\phi^2}{2\sigma_0^2}} + A_\pi e^{-\frac{(\Delta\phi - \pi)^2}{2\sigma_\pi^2}} + B[1 + 2v_2^a v_2^t \cos(2\Delta\phi)] \quad (4.4)$$

### The Reaction Plane method

The method is predicated on the ability to estimate the reaction plane of the event, to find its approximation. To differentiate between the true reaction plane and its calculated value, the approximated reaction plane is called “the event plane.” For each  $n^{\text{th}}$  flow harmonic the angle  $\Psi_n$  of its flow vector,  $Q_n$ , is calculated using the  $x$  and  $y$  components of  $Q_n$  [56]:

$$Q_n \cos(n\Psi_n) = \sum w_i \cos(n\phi_i)$$

$$Q_n \sin(n\Psi_n) = \sum w_i \sin(n\phi_i)$$

where  $\phi_i$  is the azimuthal angle of each particle used to define the event plane, and  $w_i$  is the weighting applied to optimize the event plane resolution. Thus, for the second harmonic the event plane angle would be

$$\Psi_n = \frac{1}{2} \left[ \tan^{-1} \frac{\sum_i w_i \sin(n\phi_i)}{\sum_i w_i \cos(n\phi_i)} \right]$$

The weights depend on how the events are subdivided, i.e., how particle classes are defined. Usually,

$$w_i = f(\langle p_T \rangle) \tag{4.5}$$

where the averages refer to the specific type and class of particles, for example, all pions within a given  $\eta$  slice. At STAR the weights used are simply a given particle  $p_T$  [57].

### The Cumulant method

This method works best in azimuthally-symmetric detectors. STAR is certainly one, so this method has been successfully applied by the STAR Collaboration for flow calculation. The cumulant method takes advantage of the fact that because all flowing particles correlate with the reaction plane, they must also correlate between one

another. Using several particles at a time (2, 4, or 6), and computing their cumulants as outlined below, allows one to escape the pitfalls of estimating the reaction plane, as well as to avoid the assumption that known sources of error such as jets and resonance decays are taken into account fully, since a non-flow correlation between four or more particles is unlikely [58].

The cumulants are calculated using a generator function [59]:

$$G_n(z) = \prod_{j=1}^M \left( 1 + \frac{z^* e^{in\phi_j} + z e^{-in\phi_j}}{M} \right) = \prod_{j=1}^M \left( 1 + \frac{2x \cos(n\phi_j) + 2y \sin(n\phi_j)}{M} \right) \quad (4.6)$$

which has an average value  $\langle G_n(z) \rangle$  ( $z$  here is just a complex number,  $z = x + iy$ ) over a set of events with the same multiplicity,  $M$ . Then the cumulant  $C_n(z)$  is defined as

$$C_n(z) \equiv M(\langle G_n(z) \rangle^{1/M} - 1) \quad (4.7)$$

and can be expanded [59] in terms of particle azimuthal angles  $\phi$  as

$$C_n(z) \equiv \sum_{k,l} \frac{z^{*k} z^l}{k!l!} \langle \langle e^{in(\phi_1 + \dots + \phi_k - \phi_{k+1} - \dots - \phi_{k+l})} \rangle \rangle \quad (4.8)$$

According to Reference [59], for a detector with isotropic acceptance (such as STAR), all terms of this expansion vanish except for cases when  $k = l$ . For these cases the cumulant (denoted now as  $c_n$ ) is

$$c_n(2k) \equiv \sum_{k,l} \frac{z^{*k} z^l}{k!l!} \langle \langle e^{in(\phi_1 + \dots + \phi_k - \phi_{k+1} - \dots - \phi_{2k})} \rangle \rangle \quad (4.9)$$

Then the  $v_n$  coefficients can be computed using the values obtained from the generating function  $G_n$ , expanding  $c_n$ , and calculating the numerical value using the numbers extracted from  $G_n$ . Then we have the lower order flow coefficient estimates as  $v_n 2^2 \equiv c_n 2$ ,  $v_n 4^4 \equiv -c_n 4$ , and  $v_n 6^6 \equiv c_n 6/4$ . The four-particle ( $c_n 4$ ) method is used at STAR.

## Flow measured in STAR and quark scaling

One of the most important experimental findings to come out of RHIC has been quark scaling – the discovery that the collective flow truly is collective, i.e., is at

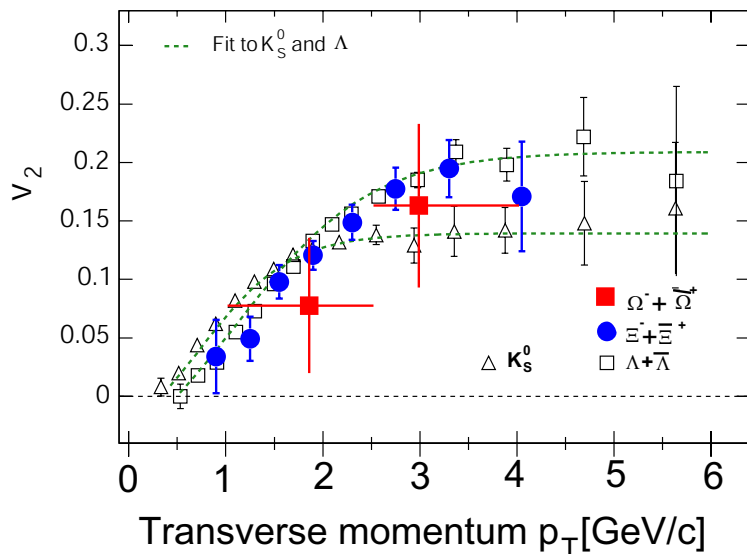


Figure 4.14: Multi-strange baryon flow measured by the STAR Collaboration in Minimum Bias Au+Au collisions at  $\sqrt{s_{NN}} = 200$  GeV [60]. The flow from singly strange particles,  $K_S^0$  and  $\Lambda^0$  is shown for reference.

the quark, and not the hadron level. In STAR, the flow has been measured as a function of  $p_T$  for many species of particles, including strange and multi-strange baryons [60]. These are shown in Figure 4.14. One striking feature of this figure is the separation of  $K_S^0$  meson flow from  $\Lambda$  and  $\Xi$  baryon flow, which will be discussed below. Dashed green curves have been added as a guide. However, we must note that the measurement of flow is a statistics-intensive measurement, very much like the study of correlation functions, and this is reflected in the error bars of the plots in Figure 4.14. The particle and the anti-particle analysis have to be summed in order to gain sufficient statistics. The result has been a definitive measurement for  $\Xi$  baryons, and a measurement that can be interpreted only qualitatively (because of its large error bars) for  $\Omega$  baryons. The  $\Xi$  flow clearly follows the pattern established by the flow of  $\Lambda$  baryons, up to 3.5 GeV/c, above which the statistics become limited, and after quark scaling, i.e., dividing the over-all measured  $v_2$  and  $p_T$  of a given species

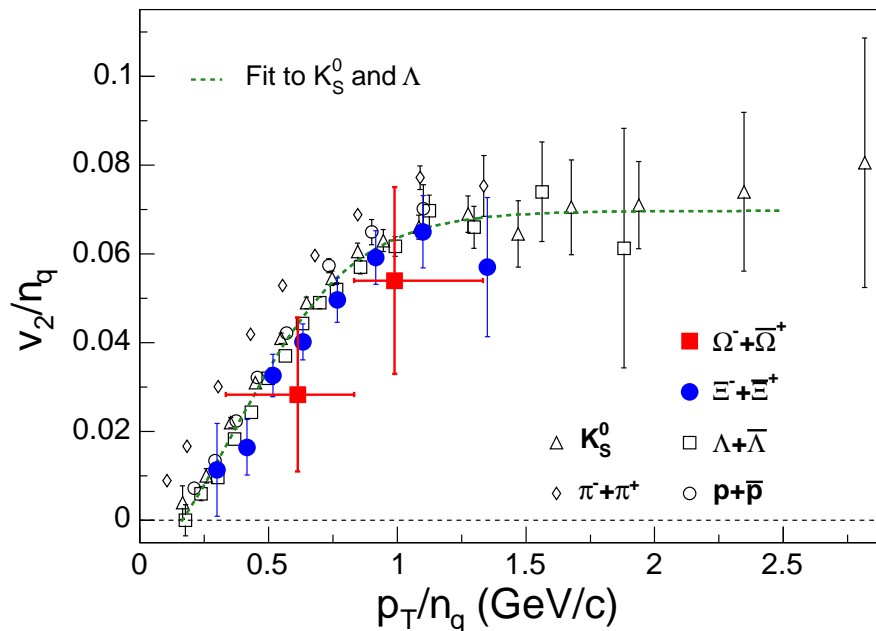


Figure 4.15: Quark scaling including multi-strange baryons. The green line is a fit to  $K_S^0$  and  $\Lambda$  points [60].

by the number of constituent quarks, one can see that the functions fall on top of one another within errors, as seen in Figure 4.15. Effectively this means that the best measured flow function for a three-quark baryon can be applied to determine the flow of baryons whose flow is not well-measured. Moreover, because of quark scaling, the flow of a baryon can be inferred from a well-measured meson. Therefore, in this analysis, the  $v_2$  function used to subtract the underlying flow from  $\Omega^\pm - h^\pm$  and  $\Xi^\pm - h^\pm$  correlations is the parameterized  $\Lambda^0$  baryon flow.

The two methods described above yield two parameterizations with respect to particle  $p_T$  that differ only in magnitude. The parameterizations are of the form [49, 61]

$$v_2 = c_1 p_T^{c_2} e^{-\frac{p_T^{c_4}}{c_3}} \quad (4.10)$$

where  $c_1$  is the constant that depends on the flow method used, and  $c_2$ ,  $c_3$ , and  $c_4$  are constants that depend on collision centrality, listed in Table 4.1

As seen in Figure 4.16, the difference in the two methods gives rise to as much as a

	$c_1$ React. Plane	$c_1$ 4-part. Cumulant	$c_2$	$c_3$	$c_4$
0-5%	0.04969	0.02485	1.273	3.133	1.352
5-10%	0.09257	0.07175	1.341	2.357	0.924

Table 4.1: Parameters used for  $v_2$  parametrization as a function of centrality class [49].

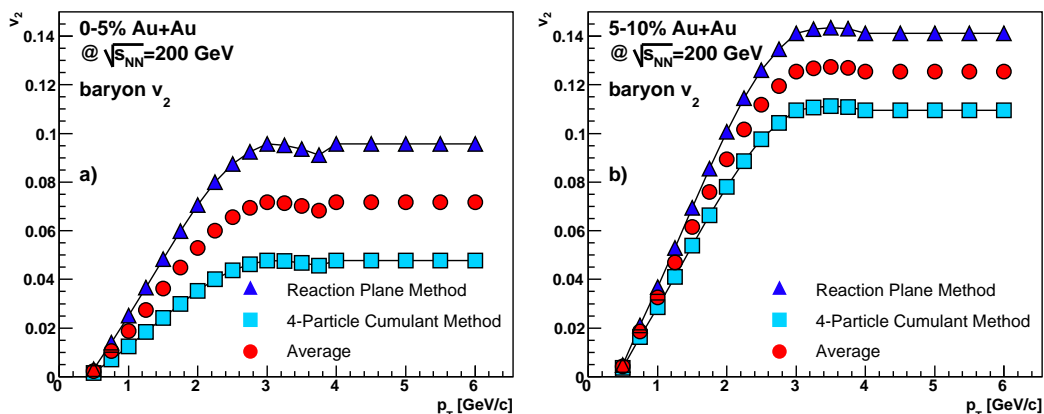


Figure 4.16: Parameterized  $v_2$  in two centrality bins. Plot *a* shows  $v_2$  in the 0-5% central bin, while plot *b* shows flow in 5-10% central bin.

35% difference in the  $v_2$  value. This uncertainty is the main source of systematic error in the correlation yields obtained below. Also we observe a nearly 50% difference in magnitude between the flow in the 0-5% central and 5-10% central collisions. This is due to the fact that the 0-5% central events are nearly completely symmetric (the anisotropy of the fireball is small), and thus the elliptic flow coefficient is also very small. The shape anisotropy is, evidently, not negligible in the 5-10% event class, hence the striking difference in magnitudes.

### 4.3.3 The ZYAM method

A signature of a back-to-back jet is the appearance of two narrow peaks with  $\Delta\phi = 180$  deg. Given the narrow jet width in  $\Delta\phi$ , we assume that the peaks do not overlap, this means that the height of the trough, the minimum between the two jet peaks, is due only to the correlated (flow and resonance decays) and uncorrelated (correlations of random tracks) background. This is then used to calculate the height of the flow

signal, the  $B$  value. Let  $p$  be such a minimum point with coordinates  $(x_p, y_p)$ , where  $x = \Delta\phi$  and  $y = dN_{pairs}/(d\Delta\phi N_{triggers})$ . Then the correlation function,  $C(\Delta\phi)$  at  $p$  will be

$$C(\Delta\phi) = y_p = B[1 + 2v_2^g v_2^t \cos(2x_p)] \quad (4.11)$$

In this equation every variable except  $B$  is known. Then  $B$  is calculated to be

$$B = \frac{y_p}{1 + 2v_2^g v_2^t \cos(2x_p)} \quad (4.12)$$

The method has been proven to work well [62].

Effectively, this means that one can calculate the height of the uncorrelated background from the lowest points of the correlation function, and then use that, along with the calculated  $v_2$  component to find the flow contribution without performing a full-data fit.

In this analysis, the ZYAM calculation has been performed with 1, 2, and 3 points around the minimum. The result for each calculation is presented in the following sections, for both  $\Xi$  and  $\Omega$  baryon correlation analyses. The ZYAM calculation is plotted, and along with a value from a free fit, yields the measurement of the systematic error associated with the particular correlation function. Below, the values obtained from ZYAM accompany every plot where the calculation was applied.

#### 4.3.4 Correlations

It should be emphasized that the measurement of multi-strange baryon correlations is extremely statistics-demanding. The statistics available allowed the  $\Xi$  baryon signal to be divided into five transverse momentum bins, while there were only enough  $\Omega^-$  and  $\bar{\Omega}^+$  triggers for one wide bin in  $p_T$ . There were two analysis methods used in obtaining these results. One method only utilized the azimuthal angle, where the corrections applied and measurements only used the projection in  $\Delta\phi$ . This has been a well-established method [10], and at the early stages of this analysis it was sufficient. However, as the importance of correcting for detector acceptance in  $\Delta\eta$  space became evident, the analysis has been extended into the second dimension:

pseudorapidity  $\eta$ . Therefore this section is divided into two parts. One deals solely with the 1-dimensional analysis, for which there are sufficient statistics, the other describes what can be done in two dimensions.

### 1-dimensional analysis

For a 1-dimensional analysis the procedure is very similar to that applied in  $d$ +Au. A correlation is constructed, the boundary correction is applied, and the function is fit using an ansatz described by Equation 4.4. The only difference between correlations in  $d$ +Au and correlations in this data is the presence of the underlying collective flow background.

As mentioned above, the relative abundance of  $\Xi$  baryons allows for five trigger- $p_T$  bins, while the one  $\Omega$  baryon bin spans a  $p_T$ -trigger range from 2.5 to 4.5 GeV/ $c$ . The mean  $p_T$  of this bin is 3.016 GeV/ $c$ . This allows us to investigate the intermediate (2-4 GeV/ $c$ )  $p_T$  range, which is an interest of this study.

First, raw correlations for both  $\Xi^\pm$  and  $\Omega^\pm$  baryons are presented. Then, in each case, we present the acceptance corrected correlation function with the elliptic flow component also plotted for comparison. We then reflect around 0 radians, subtract the background and plot the yields as a function of the trigger particle  $p_T$ .

#### a. $\Xi$

The  $\Xi$  baryon correlation signal is divided into five bins, three of which are 0.5 GeV/ $c$  wide (2.0-2.5 GeV/ $c$ , 2.5-3.0 GeV/ $c$  and 3.0-3.5 GeV/ $c$ ), the fourth – 1 GeV/ $c$  wide (3.5-4.5 GeV/ $c$ ), and the last 2 GeV/ $c$  wide (4.5-6.5 GeV/ $c$ ). The corrected and reflected correlation function is presented for each  $p_T$  bin as indicated in the panels of Figure 4.17. The panels are arranged such that panel (a) corresponds to the lowest  $p_T$ -trigger, panel (b) is the next higher trigger  $p_T$  bin, and so on up to panel (e). Panel (f) shows a much wider  $p_T$  trigger bin: from 2.5 to 4.5 GeV/ $c$ . This bin is used for comparison with the  $\Omega$ -triggered correlations and, in the next chapter, for comparison with singly-strange baryon-triggered correlations.

Table 4.2 lists the parameters used to calculate the flow component contained in the correlation function for each bin. With the notable exceptions of bins (d) and

Centrality	$\langle p_T \rangle_{Tr}$	$\langle p_T \rangle_{As}$	%	$\langle p_T \rangle_{Tr}$	$\langle p_T \rangle_{As}$	%
	<i>2.0-2.5 [GeV/c]</i>			<i>2.5-3.0 [GeV/c]</i>		
<b>0-5%</b>	2.2403	1.75901	68.1	2.7217	1.8356	68.3
<b>5-10%</b>	2.2408	1.7600	31.9	2.720	1.8355	31.7
	<i>3.0-3.5 [GeV/c]</i>			<i>3.5-4.5 [GeV/c]</i>		
<b>0-5%</b>	3.216	1.8718	66.3	3.8650	1.8901	67.7
<b>5-10%</b>	3.215	1.8723	33.7	3.8648	1.8920	32.3
	<i>4.5-6.5 [GeV/c]</i>			<i>2.5-6.5 [GeV/c]</i>		
<b>0-5%</b>	4.8987	1.8961	67.3	2.9870	1.8515	62.8
<b>5-10%</b>	4.9228	1.9005	32.7	2.9899	1.8534	37.2

Table 4.2: Centrality and mean  $p_T$  parameters for  $\Xi^\pm$ - $h^\pm$  correlation functions, used to produce panels *a-f* of Figure 4.17. The mean  $p_T$  values are given in GeV/c. The table is divided into six parts, for the six  $p_T$  bins. The first column labeled “Centrality” defines the centrality of values presented to the right. Columns labeled “ $\langle p_T \rangle_{Tr}$ ” refer to the mean  $p_T$  of the trigger  $\Xi^-$  or  $\Xi^+$  in a given  $p_T$  and centrality bin, columns labeled “ $\langle p_T \rangle_{As}$ ” show the mean  $p_T$  of the associated particles of a given bin, and columns labeled “%” show the percentage of a given centrality in the particular  $p_T$ -trigger bin. The numbers in italics denote the limits on  $p_T$ -trigger of a given bin.

	<b>2-2.5</b>	<b>2.5-3.0</b>	<b>3.0-3.5</b>	<b>3.5-4.5</b>	<b>4.5-6.5</b>	<b>2.5-6.5 [GeV/c]</b>
<b>fit</b>	6.12665	6.98283	7.20792	7.10615	7.17176	7.01288
<b>ZYAM 1</b>	6.10552	6.90992	7.13596	7.25427	6.96569	7.02016
<b>ZYAM 2</b>	6.12348	6.97108	7.19685	7.24661	7.16746	7.03770
<b>ZYAM 3</b>	6.13607	6.97300	7.23021	7.31796	7.21100	7.04250
$v_2^t v_2^a \times 10^3$	4.603	3.4856	6.0031	5.79953	5.891	6.1172

Table 4.3: Flow parameters for 6  $\Xi$   $p_T$ -trigger bins. The first four rows give  $B$ -parameter values from fitting Eq. 4.4 and from ZYAM calculations. The  $v_2^t v_2^a$  is calculated as outlined in 4.3.2.

(e), the functional fit to the data differs very little from the ZYAM calculation. In determining of the systematic errors on the yield in every bin except bins (d) and (e), the upper and lower yield bounds were determined using the upper and lower flow calculations. In bins (d) and (e) the outlying fit was removed from the calculations. All flow parameters from fits and calculations are listed in Table 4.3.

The yields from the five  $p_T$  bins are plotted in Figure 4.18. There is a rise in yield up to 3.5 GeV/c, and then the signal appears to saturate.

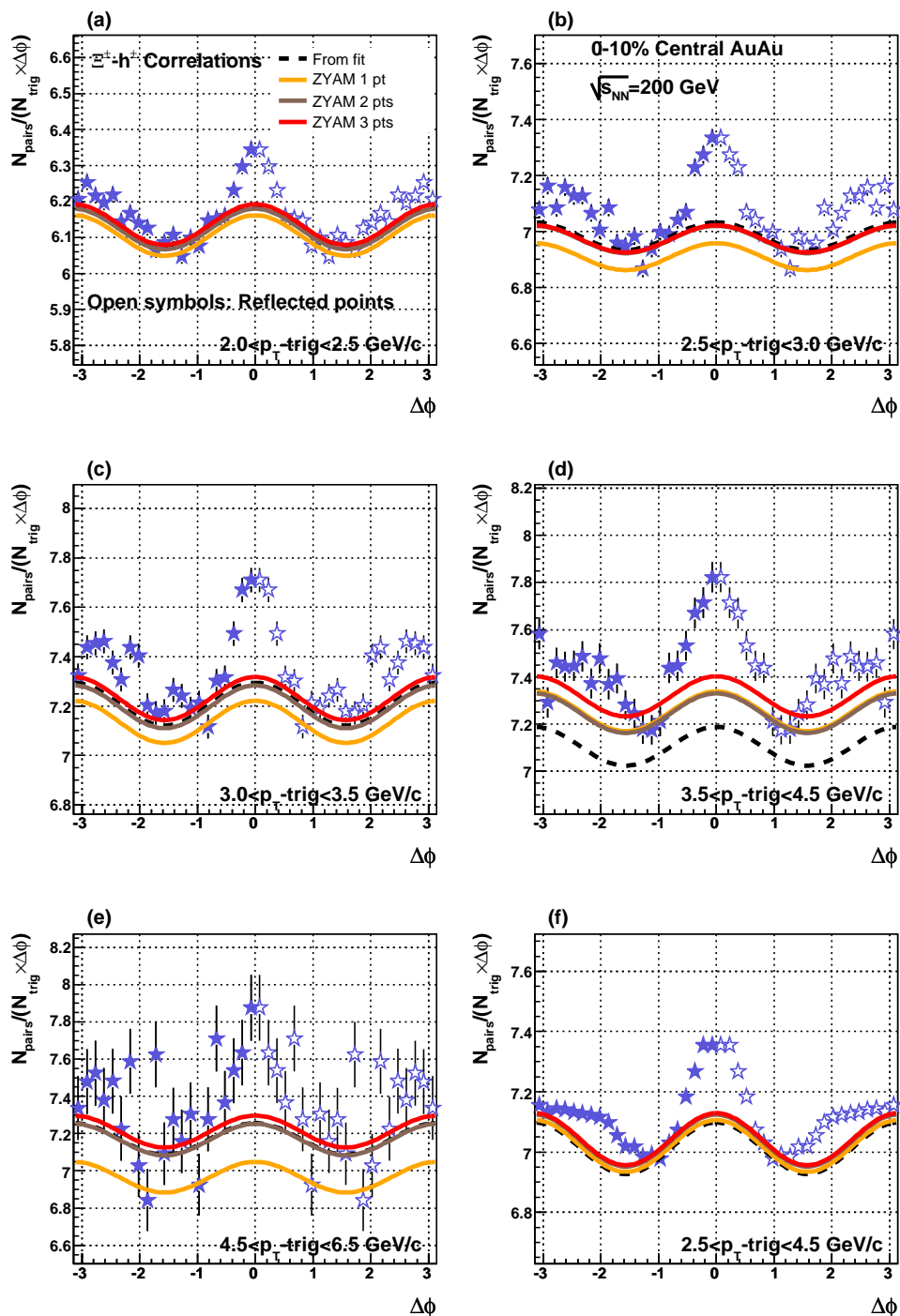


Figure 4.17:  $\Xi^\pm$ - $h^\pm$  correlation functions in six  $p_T$ -trigger bins indicated in each panel with possible flow functions calculated for each bin. The parameters used to plot the dashed curves are obtained from fitting Eq. 4.4, the parameters used to produce the three other functions are a ZYAM calculation with 1, 2, and 3 points at the function minimum.

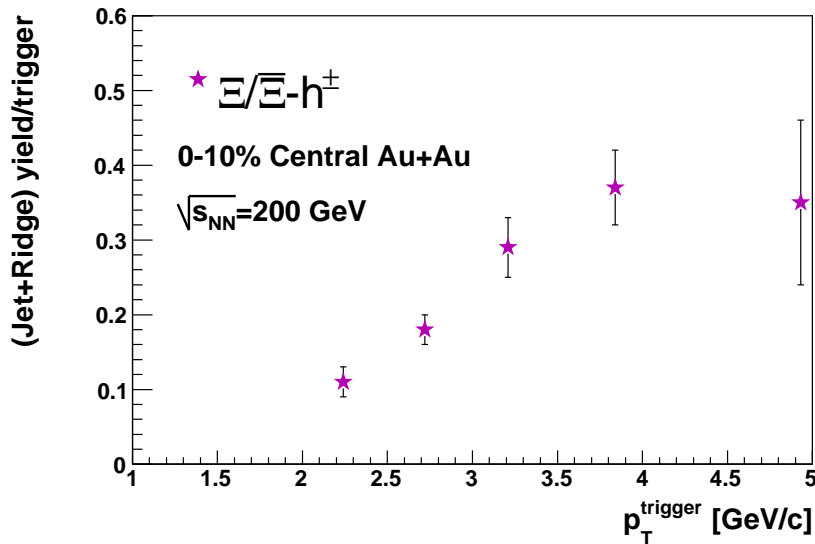


Figure 4.18:  $\Xi^\pm$ - $h^\pm$  correlation function yields. The errors shown are statistical only.

### b. $\Omega$

Applying methods used to obtain the  $\Xi$  correlation functions, we now turn to  $\Omega$  baryons. Figure 4.19 shows the Omega baryon correlation function, where the counts are corrected only for the associated particle efficiency. The same-side peak is clearly there, but we need to correct for detector acceptance to reduce the signal's fluctuations. The important feature of the figure is not only that the peak is there, but also that the correlation function, although points fluctuate, is symmetric around 0 radians. Thus, we can double the statistics by "folding" around its axis of symmetry. Figure 4.20 shows the near final product of the  $\Omega$  analysis, presenting the correlation function just before background subtraction.

For comparison, the  $\Xi$  correlation function in the same trigger and associated  $p_T$  bin is plotted. There are several interesting features of this plot. Firstly, it seems that the same-side peak for both functions is nearly identical. This indicates that there is a weak to little effect of the one non-strange quark in the  $\Xi$ , as compared to the  $\Omega$ . Another feature is the difference in height of the correlation function and

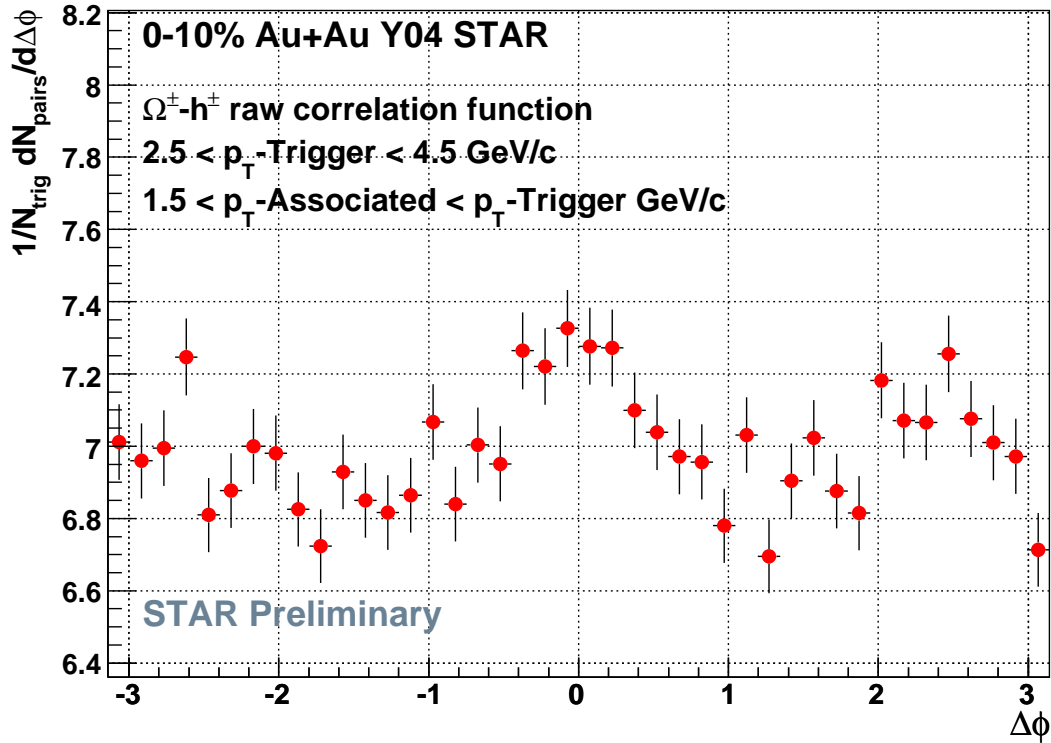


Figure 4.19: Raw  $\Omega$  correlation function, corrected for associated track efficiency, but not for detector acceptance.

the calculation of the largest possible amount of elliptic flow. The difference between the maximum magnitude of the background and that of the data is over  $1.5\sigma$ . The two unusually low  $\Omega$  data points near  $\pm\pi$  and  $\pm 0.5$  radians are believed to be due to statistical fluctuations: in studies where the expansion of the vertex cut or additional events from the same trigger class were added (and thus statistics increased), these points no longer appeared unusually low.

For clarity, we show the  $\Xi$  and the  $\Omega$  correlation function after collective flow subtraction in Figure 4.21. The dashed and solid lines illustrate the systematic error due to uncertainty in the flow background determination, and give the minima and maxima of the correlation functions after background subtraction. We see that the functions remain very close within the errors.

	0-5%		0-10%	
	$\Xi$	$\Omega$	$\Xi$	$\Omega$
%	62.78	64.24	37.22	35.76
$\langle p_T \rangle_{Tr}$	2.9870	3.000	2.9899	3.009
$\langle p_T \rangle_{As}$	1.852	1.852	1.853	1.853

Table 4.4: Multiplicity and associated and trigger particle  $\langle p_T \rangle$  parameters used to produce the correlation functions in Figure 4.20.

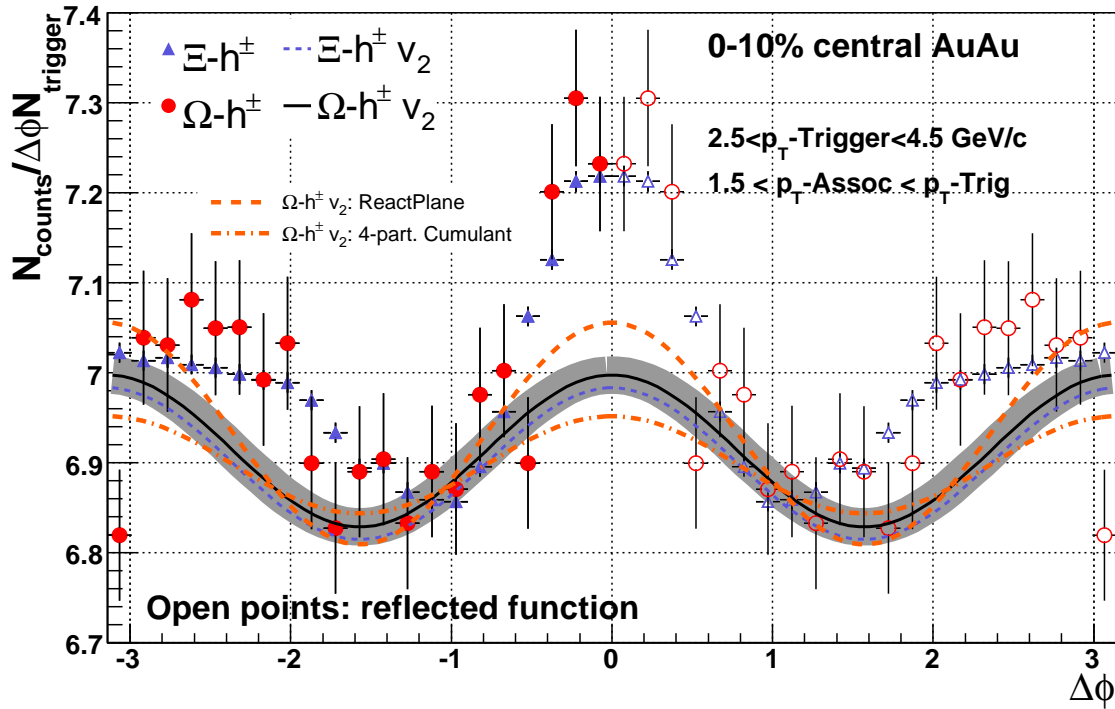


Figure 4.20:  $\Omega$  and  $\Xi$  correlation functions in 0-10% central Au+Au collisions. The  $\Omega$  function is represented by red circles, while the  $\Xi$  correlation function, plotted for comparison, is shown as blue stars. The error on the data is statistical only, however, systematic error on the flow reconstruction is shown as a grey band for  $\Omega$  baryons and covers that for  $\Xi$ . The orange dotted curves show the systematic error due to the difference in two methods for  $v_2$  determination.

## 2-dimensional analysis

In analyzing particle correlations in two dimensions, it was discovered that in  $\Delta\eta$  the same-side of the jet is accompanied by an elongated structure [63] that has come to

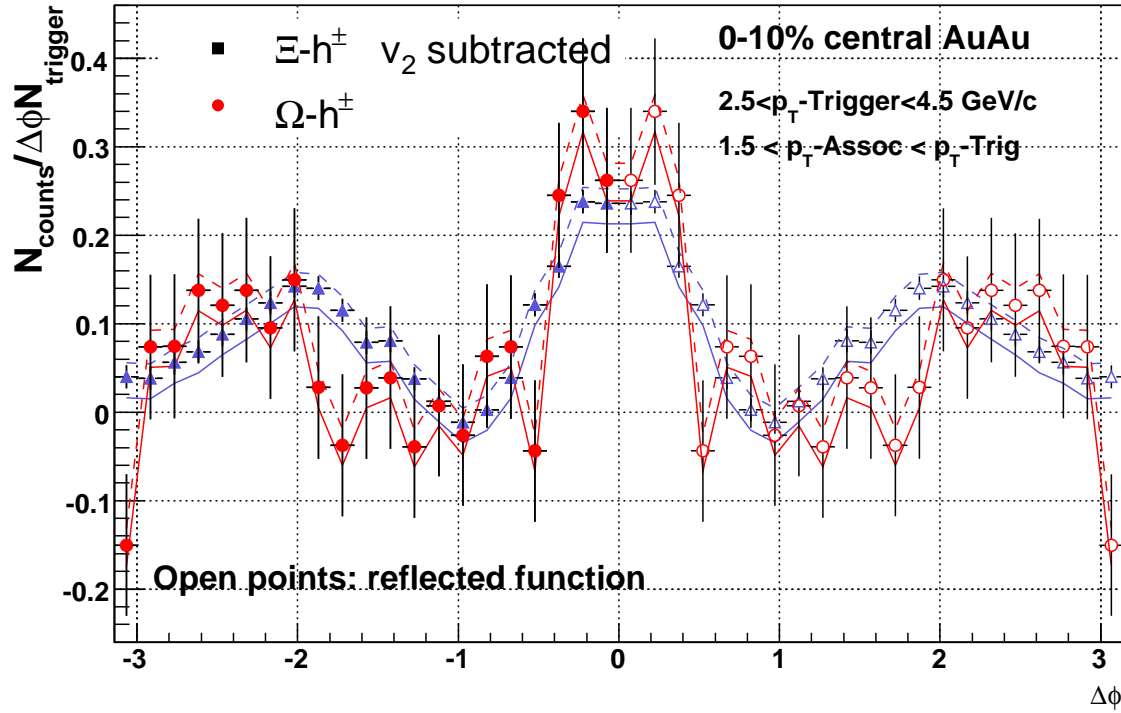


Figure 4.21:  $\Xi$  (blue triangles) and  $\Omega$  (red circles) correlation functions after background subtraction. The dashed and solid curves represent systematic errors in the determination of the background amplitude. The errors due to uncertainties in  $v_2$  determination are not shown.

be known as the *ridge* [64]. At the present time the structure of the ridge is unknown, and there are several ongoing investigations devoted to this topic [65, 66]. What is known so far is that the ridge is closely associated with the most central collisions and low  $p_T$  associated particles. At a sufficiently high  $p_T$  for the associated particle, the ridge disappears [64].

The ridge is easily seen in charged-charged correlations because of the abundant statistics. For illustration, we can use the charged-charged correlation obtained in Au+Au events containing a multi-strange baryon. A clear peak above the ridge is seen for associated particles with  $p_T$  as low as 1.5 GeV/c, but the ridge starts to diminish in importance when the associated particle  $p_T$  is increased to 2.5 GeV/c, and the trigger  $p_T$  is raised from the 2.0-3.5 GeV/c range to the 3.5-6.5 GeV/c range,

as shown in Figure 4.22.

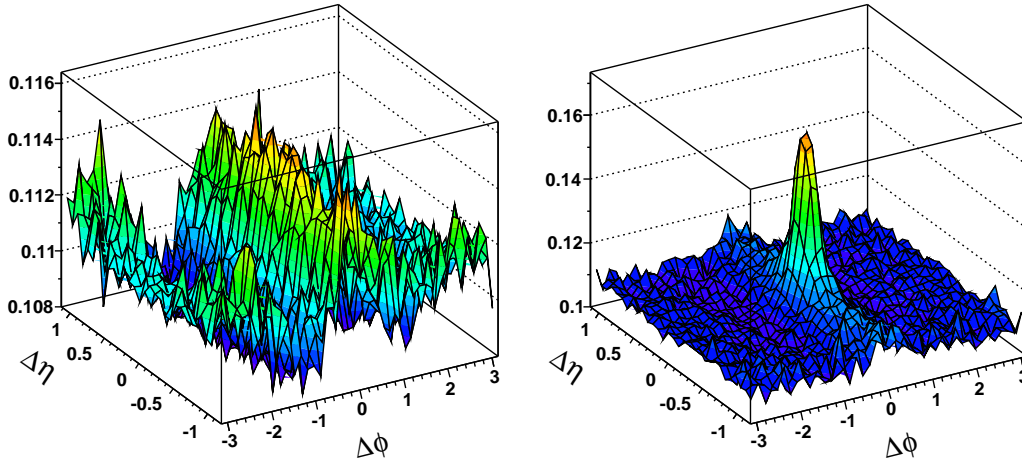


Figure 4.22: The importance of the ridge in 0-10% central Au+Au collisions is illustrated using unidentified charged particles. At low  $p_T$  of the associated and trigger particle the ridge dominates (left). When the  $p_T$  of the trigger and associated particles is increased, the ridge loses its significance with respect to the peak. In the left panel the  $p_T$ -associated is between 1.5 GeV/c and the  $p_T$  of the trigger, where  $2.0 \text{ GeV/c} < p_{T\text{-trigger}} < 3.5 \text{ GeV/c}$ . The right panel shows the jet and the associated ridge for  $3.5 < p_{T\text{-trigger}} < 6.5 \text{ GeV/c}$  and  $2.5 < p_{T\text{-associated}} < p_{T\text{-trigger}}$ .

There is a sufficient number of pairs in the  $\Xi^\pm\text{-h}^\pm$  correlations to see the ridge. However, the statistics for the  $\Omega^\pm\text{-h}^\pm$  correlation are so scarce, they wash out the signal when a two-dimensional correction is applied. Therefore, the focus of this section will be on the  $\Xi$  baryons.

To gain statistics, in the  $\Xi$  baryon 1-dimensional analysis we have made a 1.5 GeV/c cut-off for the  $p_T$  of the associated particles. In the 2-dimensional (2D) analysis, in order to be able to achieve maximum statistics for both the peak and the ridge, the lower  $p_T$  cut-off of the associated particle was raised to 2 GeV/c, and the trigger particle  $p_T$  was kept between 2.5 and 6.5 GeV/c. Panel (a) of Figure 4.23 shows a peak at  $\Delta\phi \simeq \Delta\eta \simeq 0$ . We correct for detector acceptance, by mixing the  $\phi$  and  $\eta$  coordinates of the associated and trigger particles across the event sample, as discussed in the previous chapter, to obtain the plot of panel (b) of Figure 4.23. The

mixed events are normalized to the top of the distribution by fitting a straight line to the side of the projected  $\Delta\eta$  "triangle," as illustrated on panel (f) of the same plot. Panel (e) shows the projection of the mixed events background in the  $\Delta\phi$  direction. The troughs correspond to TPC sector boundaries, and the high points to the middle of TPC sectors. The function looks the same as the 1-dimensional sector-boundary correction, as expected.

The middle section of Figure 4.23, panels (c) and (d), show the 2D correlation after the acceptance correction. One can see that the jet signal is smeared, but appears to concentrate in the  $|\Delta\eta| < 0.7$  region. One notable feature of the two-dimensional  $\Xi$  correlation is the dip in the peak at the  $\Delta\eta = \Delta\phi \sim 0$  region. This feature is being extensively studied by the collaboration, and is currently thought to be an artifact of track merging in the TPC. However, the details are still not understood.

Now that it is established that there is an elongation of the same-side peak along the pseudo-rapidity axis, the following ridge-subtraction method is applied:

1. The  $\Delta\eta$  region is broken up into three slices, one with  $|\Delta\eta| < 0.7$  (region 1), another with  $0.7 < \Delta\eta < 1.4$  (region 2), and the third, final slice, with  $-1.4 < \Delta\eta < -0.7$  (region 3), as shown in Figure 4.24
2. Each  $\Delta\eta$  slice is projected independently into a 1-dimensional histogram in  $\Delta\phi$ , and the region 2 and 3 data are summed.
3. Similar to the 1-dimensional analysis, the data in the two resulting histograms is folded about  $\Delta\phi = 0$  to double the statistics.
4. By performing steps 1 and 2 above, we have obtained two slices with equal  $\Delta\eta$  intervals. The slice of the histogram in region 1 should contain both the jet and the ridge, while the region 2 and 3 slices should only have the ridge contributing to the same-side peak in  $\Delta\phi$ . Subtracting region 2 and 3 from region 1, one can obtain the pure jet yield. There is no need to subtract the  $v_2$  or the background, as there are no systematic  $v_2$  measurement errors associated with this procedure, as all of the background, both correlated and not, has been subtracted along with the ridge.

5. Now we are left with determining the ridge contribution. This can be done by fitting

$$A_0 e^{\frac{-x^2}{2\sigma^2}} + B[1 + 2v_2^a v_2^t \cos(2\Delta\phi)]$$

to the projection of region 1, subtracting the background, and then subtracting the already known jet contribution. The ridge is what remains after all subtractions.

6. Both the jet and the ridge function are then fit with a gaussian to obtain the yields.

Unfortunately, while steps 1-3 of the above procedure do not pose a problem (the result of these steps is shown in Figure 4.25, the last step results in a function that is consistent with zero in the region of interest.

Thus, instead of subtracting the correlation functions and calculating the yield, the yields in each correlation function slice are calculated and then subtracted. The result is consistent both with zero, and with the previous pure jet yields calculations done with the  $\Lambda$  [67]:  $-0.02 \pm 0.28$ . The only encouraging result is the subtraction of the two fits themselves: the yield there is clearly above zero, as seen in Figure 4.26.

Thus, it remains unclear, whether the multi-strange jet can be decomposed into the two components. As we will see in the following chapter, this decomposition is successfully used for the analysis of its non-strange and singly-strange counterparts. One remains optimistic that the pure-jet signal is not seen due to the loss of pairs in the  $\Delta\eta = \Delta\phi = 0$  region, however, because we cannot yet correct for the dip, no conclusion can be drawn.

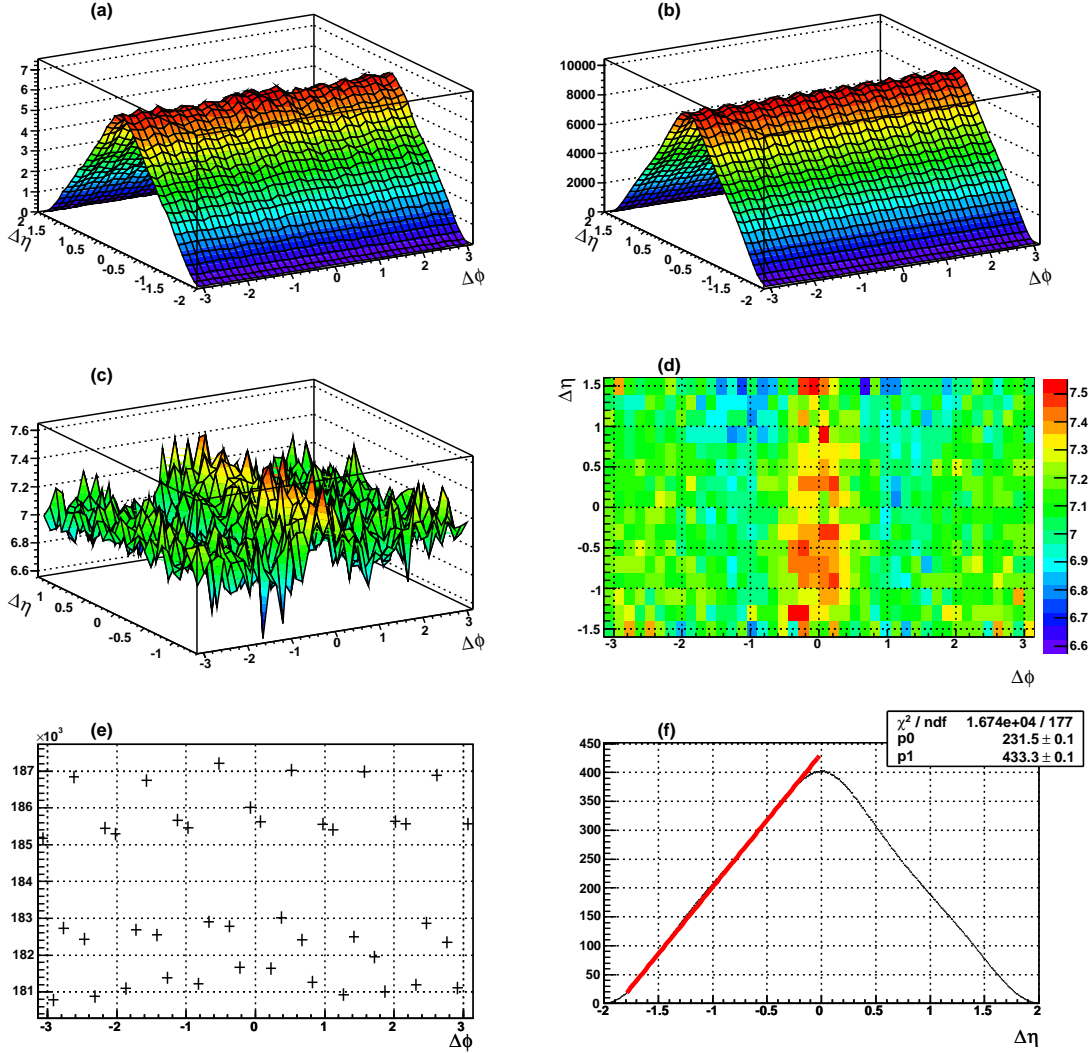


Figure 4.23: Analyzing  $\Xi^\pm$ - $h^\pm$  correlations in 2 dimensions ( $\Delta\phi, \Delta\eta$ ): (a) The raw 2D correlation function; (b) 2-dimensional event mixing before normalization; (c) 2D correlation function corrected using 2D mixed events; (d) a color-coded scatter plot of a 2D correlation function corrected using 2D mixed events (color code is on the right side); (e) a projection of the un-normalized 2D mixed events function in  $\Delta\phi$  direction; (f) a projection of the un-normalized 2D mixed events function in  $\Delta\eta$  direction and a fit to the function designed to find the magnitude of normalization. The 2D function presented is for  $2.5 < p_{T\text{-trigger}} < 6.5$  GeV/c, and for  $2.0 < p_{T\text{-associate}} < p_{T\text{-trigger}}$ .

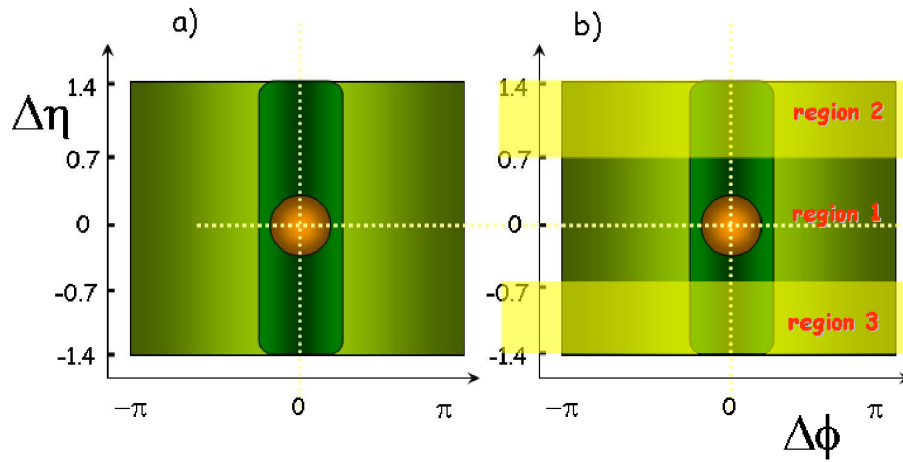


Figure 4.24: a) A schematic representation of a 2-dimensional correlation function as seen from above. The Dark Green band represents the ridge, the orange circle - the jet signal visible above the ridge. b) Dividing the 2-dimensional correlation function into three regions. Regions 2 and 3 (shaded yellow) represent the ridge-only slices, while region 1 contains both the jet and the ridge.

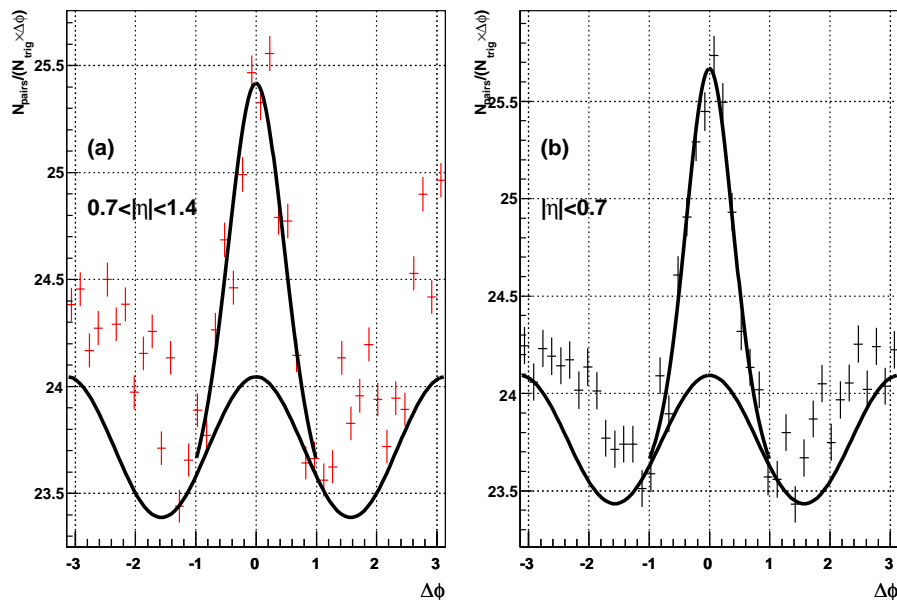


Figure 4.25: Fits to the ridge-only region ( $0.7 < |\Delta\eta| < 1.4$ , panel (a)) and the ridge+jet region ( $|\Delta\eta| < 0.7$ , panel (b)) same-side peaks using Eq. 4.4.

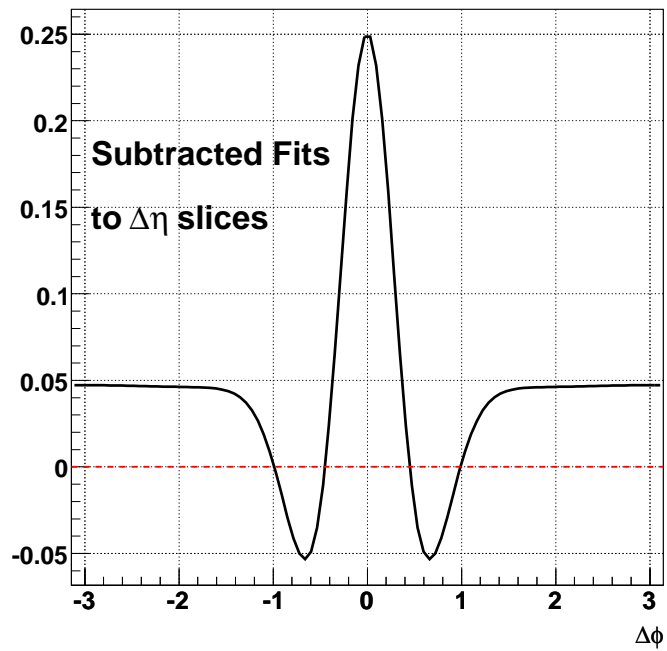


Figure 4.26: The remainder of the subtraction of the  $0.7 < |\Delta\eta| < 1.4$  correlation function slice from the  $|\Delta\eta| < 0.7$  slice.

# Chapter 5

## Interpretation and Context

In this chapter the correlation results obtained in the previous section will be presented in the context of the existing theoretical framework and in relationship to measurements made in STAR and in other RHIC experiments.

The goal of studying the multi-strange particle correlations is to investigate the mechanism of hadron production in an extremely hot and dense medium that may resemble the medium formed after the Big Bang. As we have seen in Chapter 1, the  $s$ -quark is a very convenient candidate for such a study. There are no valence  $s$ -quarks in the colliding nuclei, therefore all of them are produced in the collision; the mass of the strange quark is closer to that of quarks composing ordinary nuclear matter than any other heavy quark; a system with partonic degrees of freedom is expected to produce copious amounts of  $s$ -quarks for study.

One of the earliest predicted QGP creation signatures is that creating a hot and an extremely dense medium would remove the phase-space constraint (“canonical suppression”) on the  $s$ -quark production, present when strangeness is produced via hadronic interactions. If true, the strangeness content measured after the collision would increase dramatically. Indeed, when measured, the strangeness content has been seen to rise with number of nucleons participating in the collision, and possibly saturate in the most central Au+Au events [68].

Thus we know more strangeness is produced at levels that cannot be explained by interactions inside a hadronic gas. This is strongly suggestive of formation of

the Quark Gluon Plasma. However, we have also seen an increase in strangeness yields in systems with lower energy-density (e.g., SPS, AGS), which are just at or below the QGP phase transition (Figure 1.1). Therefore, the increase in strangeness is not sufficient to postulate the formation of a QGP. Correlation studies with multi-strange baryons help to understand the system that is formed. The modification of unidentified particles angular correlation by the medium can reveal the density of the medium. The modification of a correlation made with a leading particle composed entirely or predominantly from  $s$ -quarks can reveal information on in-medium particle formation. First, we compare the azimuthal correlation yields obtained for doubly-strange baryons in a non-QGP system ( $d$ +Au) and a system where the energy-density is expected to be sufficient for a phase-transition (Au+Au) [69, 70]. Then we will discuss the same side yield in the Au+Au collisions across strange particle species and in two spatial directions,  $\Delta\phi$  and  $\Delta\eta$ . Finally, we will discuss the future directions and the outlook for the study of multi-strange correlations.

## 5.1 Comparison to other correlation measurements

### 5.1.1 $p + p$ measurement

Due to the canonical suppression of strangeness in  $p + p$  interactions and a small data sample, it was not possible to obtain a quantitative multi-strange correlation measurements from the STAR  $p + p$  collision data. The measurement was only possible for doubly-strange  $\Xi^\pm$  baryons, as the entire minimum bias  $p + p$  data set contained only 50  $\Omega$  baryon triggers [46]. A correlation function using  $\Xi$  baryons exhibited a wide correlation peak, narrower and smaller in amplitude than the away-side peak. However, the statistical error bars were too large to determine the quantitative parameters.

From event-characteristic indicators, it is evident that the majority of  $\Xi$  baryons produced in minimum bias  $p + p$  collisions are produced in jetty events, with higher than normal multiplicities and  $\langle p_T \rangle$ . The multiplicities of events containing a  $\Xi$  are similar to those triggered by high energy localized deposits in the STAR BEMC,

supporting the hypothesis of an increase in event jettiness.

### 5.1.2 $d$ +Au measurement

The  $\sqrt{s_{NN}} = 200$  GeV  $d$ +Au data set, contains a sufficient number of  $\Xi$  triggers and charged hadron correlation candidates to obtain one large trigger- $p_T$  bin, with trigger particle  $p_T$  varying from 2 to just over 6 GeV/c. The mean trigger  $p_T$  of this ensemble is 2.54 GeV/c, and the statistics are sufficient to obtain the same-side and the away-side yields. The widths of the peaks can also be measured. The same-side yield that is obtained (the "jet yield") is  $0.015 \pm 0.026$ . This is more than an order of magnitude smaller than the integrated same-side yield of  $0.20 \pm 0.05$  for Au+Au collisions with the  $\Xi$  trigger  $p_T$  from 2 to 6.5 GeV/c. However, in singly-strange and non-strange correlation analyses, it was found that a significant contribution to the jet yield in the low trigger  $p_T$  bin is from the so-called "ridge" – an elongation of the pedestal of the same-side peak in the  $\Delta\eta$  direction, as described in Chapter 4. In the absence of multi-strange data with the  $\Delta\eta$  information, it is useful to compare the yield with other, more abundant singly-strange particle measurements made by STAR. Thus the  $\Xi$  measurement in  $d$ +Au is compared to  $\Lambda^0$  and  $K_S^0$  integrated yields and the yield as a function of  $p_T$  trigger, obtained in  $d$ +Au collisions by Jana Bielcikova of our group [65, 67].

The integrated jet yield per trigger as a function of centrality is shown in Figure 5.1 for h-h (charged-charged),  $K_S^0$ -h and  $\Lambda$ -h correlations in  $d$ +Au and Au+Au data. The  $\Xi$ -h jet yield is much lower, but within errors of both the  $K_S^0$  and  $\Lambda^0$  yields in the same collision system. On one hand, the lower yield might be expected, since the  $\Xi$  baryon is more massive than either the  $K_S^0$  or  $\Lambda$  trigger particles, and thus requires a larger fraction of jet energy to form. This would leave less energy to produce suitable associated particles. Thus, it is possible that an increase in mass of the leading hadron would lead to a reduction of the same-side yield for fragmenting partons of comparable energies.

On the other hand, the difference in mass is insufficient to make the yields very different. The difference in mass between the  $K_S^0$  and  $\Lambda^0$  is much larger ( $0.498$  GeV/c<sup>2</sup>

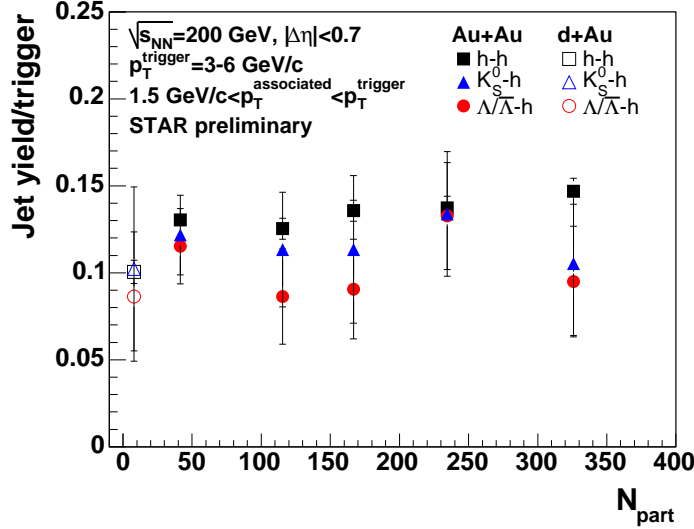


Figure 5.1: Integrated jet yields as a function of collision centrality. Open points represent the yields in  $d+Au$  collisions. As presented at the Quark Matter 2006 conference [65]

and  $1.115 \text{ GeV}/c^2$ ) than between the  $\Lambda^0$  and  $\Xi^\pm$  ( $1.115 \text{ GeV}/c^2$  and  $1.321 \text{ GeV}/c^2$ ), yet the integrated  $d+Au$  same-side yields for  $K_S^0-h$  and  $\Lambda^0-h$  are nearly identical. We also cannot attribute the possible difference between the  $\Xi-h$  and  $\Lambda-h$  same-side yield to the phase-space suppression of the  $s$ -quark and therefore the suppression of the particle with the greater  $s$ -quark content. The yields are measured per trigger. Therefore, a reduced number of triggers should not reduce the yield, only decrease the available statistics, which is reflected in the large error bar. Moreover, it is important to take the error bars on the measurement seriously, and within error the yields are the same. Thus, we conclude that the integrated yields of  $K_S^0-h$ ,  $\Lambda-h$ , and  $\Xi-h$  correlations in  $d+Au$  are consistent with one another.

We can also compare the  $\Xi-h$   $d+Au$  yield to jet-only yields in  $Au+Au$ . Figure 5.2 shows the dependence of the jet yield on the  $p_T$  of the trigger particle in 0-10% central  $Au+Au$  collisions. The rapidity window for the jet yields shown in the figure is  $|\eta| < 0.7$ , while the rapidity range for the  $d+Au$  measurement was  $|\eta| < 1$ . Scaling the  $\Xi-h$  correlation yield in  $d+Au$  by the rapidity acceptance, we

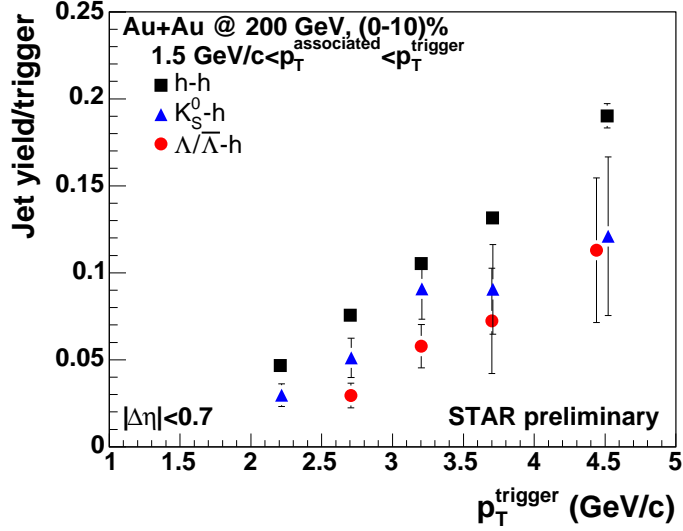


Figure 5.2: Jet yield as a function of trigger particle  $p_T$  in 0-10% central Au+Au collisions [67]

obtain the yield  $0.029 \pm 0.012$  for  $|\eta| < 0.7$ . The mean  $p_T$  of the measured  $d$ +Au  $\Xi$  correlation bin is 2.53 GeV/c, just to the left of the lowest  $\Lambda^0$  trigger  $p_T$  bin. Comparing the measurements, we see again that the  $\Xi$ -h correlation yield is slightly lower than the yield obtained for the  $\Lambda$ -h correlation, but consistent within the errors. This establishes an important framework for the study of jet+ridge yields in the Au+Au collisions: we know that the jet components of the singly and doubly strange particles in  $d$ +Au (where there is no medium) are the same within errors. We also know that the extracted  $\Lambda$ -h jet yield in  $d$ +Au is the same within errors as the  $\Lambda$ -h Au+Au yield. Therefore, if a pure  $\Xi$ -h jet yield could be extracted in Au+Au, we would expect it to be similar to the  $d$ +Au yield, and the excess to be due to the "ridge".

### 5.1.3 Au+Au results

The most striking result of this study is the observation of the non-zero same-side  $\Omega$  correlation peak. The data has been shown in the previous chapter. Here we, as we

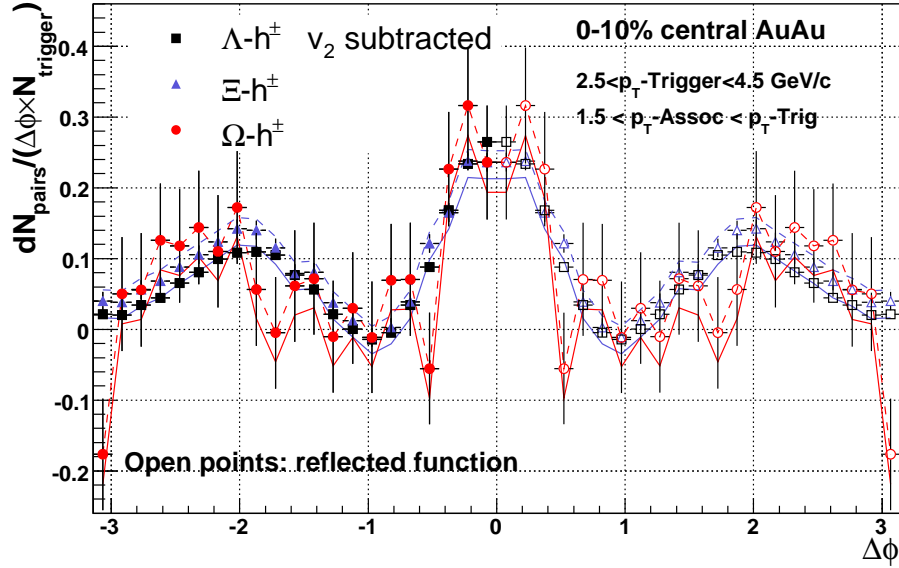


Figure 5.3: Correlation functions after elliptic flow subtraction.

did in the  $d+Au$  section, compare our results with the correlation function of singly-strange baryons also measured in STAR. As seen in Figure 5.3, after the background subtraction, the three correlation functions obtained using trigger baryons with one, two, and, finally, three  $s$ -quarks, all fall on top of one another within errors. Not only the heights of the peaks, but also their widths appear very similar. All three functions were triggered on baryons with  $p_T$  between 2.5 and 4.5 GeV/c, all three were made with associated charged tracks of  $p_T > 1.5$  GeV/c and up to the  $p_T$  of a given trigger particle. All three were chosen from the same centrality (0-10%) and  $\eta$  range ( $|\eta| < 1$ ). The dashed and solid lines on the figure, as before, represent the systematic error due to uncertainties in the subtraction of the elliptic flow.

In the previous chapter we showed the yields obtained in various  $p_T$  trigger bins both for the  $\Omega$  and  $\Xi$  baryons. We now put these yields in the context of the correlations of other species measured in STAR. Figure 5.4 presents the yields obtained using  $\Lambda^0$  (blue triangles),  $K_S^0$  (red circles),  $\Xi^\pm$  (closed stars),  $\Omega^\pm$  (open star), and charged hadron triggers (black squares). Shaded bands denote the systematic uncertainty due to the flow subtraction for each particle in each  $p_T$  trigger bin. We see that the  $\Xi$  correlation yields are consistent with both the  $\Lambda$  and  $K_S^0$  yields throughout the

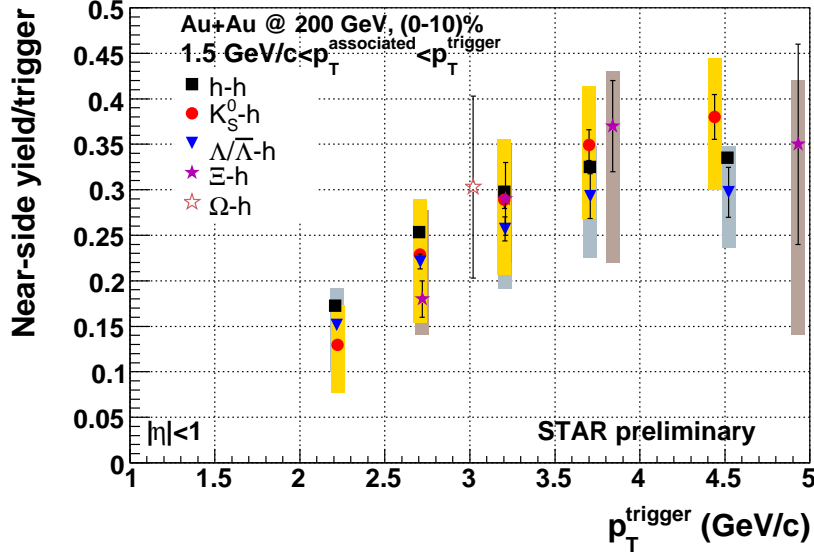


Figure 5.4: Jet+Ridge yields of strange particles in 0-10% central Au+Au collisions [65]. The shaded bands represent systematic errors due to elliptic flow subtraction. Yellow corresponds to the error on the  $K_S^0$  measurement, light blue – the error on the  $\Lambda$  measurement. The brown bands represent the error on the  $\Xi$  yield determination.

spectrum. Moreover, the yield obtained for the triply-strange  $\Omega$  baryon correlations follows the pattern. The yields increase up to 3.75 GeV/c, and then appear to saturate. These are the so-called "jet+ridge" yields, i.e., yields integrated over the entire  $\Delta\eta$  region without the "triangle" subtraction. To separate the ridge contribution to the yields from fragmented quarks (the so-called Shower partons), we compare this figure to Figure 5.2. The two figures are consistent, and when considered together indicate that the rise in the  $\Xi$  correlation yield with the rise of  $p_T$  trigger is due to the increased jet yield, not the ridge.

The last significant finding of this work is the ridge result for a multi-strange baryon correlation. Panels (c) and (d) of Figure 4.23 show an elongation below the same-side peak, and what appears to be a concentrated jet signal in the  $|\Delta\eta| < 0.7$  region.

### 5.1.4 Other RHIC experiments

The STAR detector is unique among the RHIC experiments in its capabilities to reconstruct strange particles, and thus is the only one where strange particle correlation measurements are attempted. Therefore, we cannot directly compare the heavy ion strange particle correlation measurement done in STAR to those done in other experiments.

However, we can compare to the non-strange identified particle correlation measurements made by the PHENIX experiment. The azimuthal correlation studies can help to discern the difference in production mechanisms for mesons and baryons, and the PHENIX detector is well-suited to measure pions and protons. The PHENIX Collaboration was instrumental in developing the ZYAM method and was the first to implement it in their unidentified hadrons correlation studies [71]. A direct comparison of the study presented in this work to PHENIX analysis is not possible, as mentioned above. Thus, we first compare the results of the multi-strange baryon correlation analysis to STAR unidentified charged track correlation analysis, and then compare the STAR h-h result to that seen by the PHENIX collaboration.

Having done the comparison, we observe that the multi-strange results are inconsistent with the PHENIX data [71]. While the measurement made in this dissertation agrees with the measurement done in STAR for the charged-charged correlation functions, the same-side yields (PHENIX calls these the "near-side yields") obtained by the PHENIX collaboration in its most central Au+Au collision region at mid-rapidity ( $0.13 \pm 0.02$  [71]), seen in Figure 5.5, is consistent with the STAR jet-yield only, but significantly underestimates the jet+ridge yield. There is no indication that a ridge subtraction has been performed. Also, the PHENIX Pseudo-rapidity acceptance is significantly smaller than that of STAR ( $|\eta| < 0.35$  for PHENIX). Thus, it remains to be seen where the analyses differ, and why.

The PHOBOS collaboration, with its many spectrometers and large rapidity coverage may provide a good comparison measurement in  $\Delta\eta$ - $\Delta\phi$  correlations. However, the correlation analysis available by this experiment are for Cu+Cu and  $p+p$  charged-charged data only, and only became available very recently [72]. These first results show no indication of a ridge in  $p+p$  collisions, only a hint of one in the most central

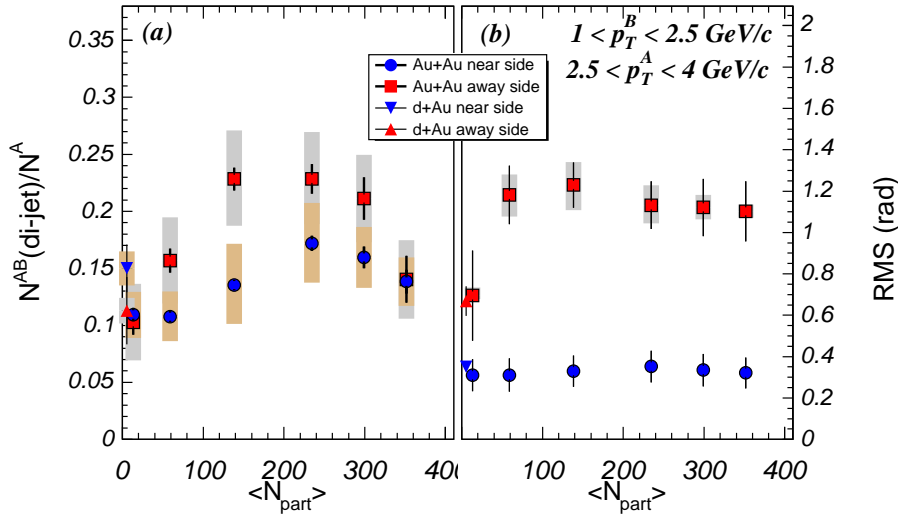


Figure 5.5: Jet yields and widths measurement by the PHENIX collaboration in Au+Au  $\sqrt{s_{NN}} = 200 \text{ GeV}/c$  collisions. [71]. (a) The near-side (blue circles) and away-side (red squares) yields as a function of  $N_{ch}$ . (b) The widths of the near-side (blue circles) and the away-side (red squares) of the azimuthal correlation function also as a function of  $N_{ch}$ . The triangles show the results in  $d$ +Au collisions at the same energy.

0-10% Cu+Cu event sample.

## 5.2 Discussion

With sufficient statistics, the multi-strange baryon correlations open a wealth of opportunities. By studying the deformation of the medium due to a passing jet (the ridge), we can perhaps access the interaction mechanisms between thermally produced quarks and those produced via fragmentation. The multi-strange correlation functions can be compared to correlations measured with singly-strange particles as a function of  $p_T$  and centrality to access mechanisms with which particles at intermediate  $p_T$  are created. Finally, by measuring the away-side modification, we may learn how the energy lost by the away-side of a strange jet is deposited. However, the statistics are barely sufficient for a detailed doubly-strange baryon measurement, and are only enough for a first measurement of triply-strange baryons.

The measurement of the pure  $\Xi$  jet yield, only available in  $d$ +Au is very important. Parton fragmentation is an initial state process. There is no hard scattering possible in the thermal bath. Therefore, although in a Au+Au collision the number of hard scatterings is increased with respect to a  $d$ +Au collision, the initial number of associated particles per trigger due to fragmentation should be the same. This conjecture is supported by the measurement of integrated  $\Lambda$ -h and  $K_S^0$ -h correlation yields across centralities that we have seen in Figure 5.1. The jet yields for a given particle species are the same within errors for all multiplicity bins.

The  $\Xi$ -h integrated yield in  $d$ +Au and Au+Au was measured at a relatively low  $p_T$  (2.53 GeV/c in  $d$ +Au, 2.6 GeV/c in Au+Au). This is just the region where the calculations of the University of Oregon Recombination Model apply. This is to say that the constituent partons of baryons at this  $p_T$  are expected to be produced both thermally and via fragmentation.

The  $\Xi$ -h integrated correlation measurement can be seen in the context of the mid- $p_T$  enhancement of the  $R_{CP}$  ratio. In both cases the central Au+Au yield is enhanced. The enhancement is over the  $d$ +Au yield in the case of the correlation function, and over peripheral Au+Au spectrum in the case of  $R_{CP}$  measurement. This enhancement can be seen as a result of thermal  $s$ -quarks, copiously produced from a thermal bath and recombining into baryons in the large volume of the medium.

The basic physics of the University of Oregon Recombination Model predicts this: contributions to the spectrum are expected from  $STT$ ,  $TTT$ ,  $SST$  and  $SSS$  hadrons [28], as described in Chapter 1. The  $SST$ ,  $STT$  and  $TTT$  components are not available in a smaller systems, and thus the yields are smaller. This is to be expected. The unexpected finding that comes from the measurement presented in this work, is what we observe when we compare yields from  $\Omega$ ,  $\Xi$  and  $\Lambda$  baryon correlations in the same trigger momentum, centrality, and  $\eta$  range. The similarity of the yields is puzzling, and is contrary to the Recombination Model's assumption [28] that the fragmentation component is irrelevant in the  $\Omega$  spectrum up to 8 GeV/c because of the  $s$ -quark suppressed fragmentation.

We have seen that the  $\Lambda$ -h and  $\Xi$ -h same-side yields in  $d$ +Au are the same within errors. This is somewhat contrary to Hwa's assertion that the  $S_s$ , the shower  $s$ -quark

contribution, is suppressed in fragmentation. The assertion is based on a calculation of shower parton distribution functions (SPDs) [73] normalized to fragmentation functions obtained from experimental data [74]. However, the errors on the same-side  $\Lambda$  and  $\Xi$  yields that measurement in  $d$ +Au are large, and the calculation may yet be correct.

Nevertheless, if the calculation is accurate, the similarity across particle species in central Au+Au collisions is even more striking. One possible explanation is that the  $TSS$  or even  $TTS$  part of the strange baryon spectra contribute to the same-side jet+ridge yield by manifesting itself as the ridge. However, what then remains unclear is why the ridge yield is different for different particle species. Why does it "compensate" for the heavier particles. Perhaps it is not the mass of the strange particle, but the strangeness content – perhaps the ridge is increased with increased strangeness, but by which mechanism? At the present time the composition of the ridge is unknown. Moreover, as we have seen in Chapter 4, the statistics are insufficient for a multi-strange baryon ridge measurement. Thus, this argument remains a speculation. Perhaps the similarity of the same-side peaks suggests that within measurable errors, the  $u$ ,  $d$ , and  $s$  produced quarks behave similarly in the QGP.

It is evident that the understanding of the origin of the  $\Delta\eta$  ridge and its composition will be key to understanding the nature of multi-strange correlations. There are a number of models seeking to explain the elongation under the jet-peak observed in the most central Au+Au collisions. Some possible explanations recently proposed are introduced below.

The model championed by Armesto et al. [75] explains the "ridge" as an effect of flow, being in a different co-moving frame from the jet, "scattering" the gluon radiation in the  $\eta$  direction, as illustrated in Figure 5.6. If this model is correct, the ridge should be strongly anti-correlated with the  $\eta$  of the leading particle of the jet.

Another model by Majumder et al. presents the ridge as a result of plasma instabilities and subsequent gluon field self-interactions [76]. In this model, gluons radiated from a jet interact with the medium, assumed to be a plasma of quarks and gluons. As the radiated gluons interact, they produce a longitudinal broadening, symmetric in  $\Delta\eta$  around the jet cone.

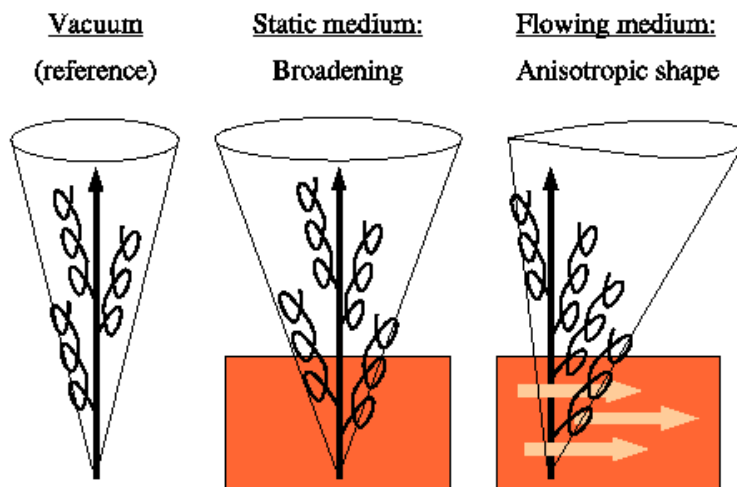


Figure 5.6: A sketch of fast parton in vacuum (a), in a static medium (b), and in a flowing medium (c) [75].

Yet another model from Hwa and collaborators [77] treats the ridge as a product of fragmenting partons recombining with thermal ones, in line with the reasoning outlined in the framework of the University of Oregon Recombination Model. Initial considerations did not involve multi-strange baryons, however since the discovery of the same-side  $\Omega$  peak, the model has been revised to include the peak.

Sergei Voloshin's model treats the ridge as a result of radial flow of soft particles, created along the jet axis [78]. This is the only model that can explain the apparent absence of the away-side ridge, as the away-side is likely to be anti-correlated to radial flow.

Apart from Rudy Hwa's model, none of these models treat the strange quark differently. The first two models cited do not need to; they consider gluons interacting with a uniform medium. In Hwa's model, the  $T_s$  (thermal  $s$ -quark) term is somewhat suppressed with respect to the non-strange  $T$  component. Thus, qualitatively, it is unclear why a suppressed  $T_s$  component would preferentially combine with the  $S$  component to form the ridge and "compensate" the multi-strange same-side to make it similar to that of  $\Lambda$ -h same-side. However, we must remember that the idea of the ridge is very new, and models trying to explain it are very recent.

### 5.3 Conclusion

In this work, we have presented the first measurement of multi-strange baryon azimuthal and longitudinal correlations in relativistic heavy ion collisions. Correlation functions were obtained in the  $p + p$ ,  $d + \text{Au}$  and the central 0-10% Au+Au data sets. The yields measured for  $\Xi$  baryon correlations in the  $d + \text{Au}$  data are consistent with other strange particle results in the same data and with jet yields of singly-strange particles in the same trigger-momentum region of the most central Au+Au data. However, the main foci of this work are the triply-strange baryon correlations. An  $\Omega$  baryon correlation function was obtained in the 0-10% most central Au+Au collisions and after background subtraction, the same-side peak was compared to that of the  $\Xi$  baryon correlation and  $\Lambda$  baryon correlation in the same data. Contrary to the University of Oregon Recombination Model predictions, the  $\Omega$  same-side peak yield is  $3\sigma$  above a null value. In fact, the yields of the three strange baryon species,  $\Lambda$ ,  $\Xi$ , and  $\Omega$  are consistent within errors. This leads one to conclude that the behavior of the three lightest ( $uds$ ) quarks in the QGP environment is similar. Further studies of multi-strange correlations in  $\Delta\eta$  space will yield more details, however at present the available statistics do not allow for a more detailed measurement.

### 5.4 Outlook

Although there are sufficient statistics to *observe* a  $\Xi$  baryon correlation function in  $\Delta\eta - \Delta\phi$  space in the most central Au+Au collisions, we are not yet ready to draw definitive conclusions before the so-called dip at  $\Delta\eta \sim \Delta\phi \sim 0$  is understood fully. At the moment, there is a strong effort in the STAR collaboration to account for the loss of correlation pairs in this region. Although the study to determine it has been in progress for over a year, we still do not know what causes the loss. The "dip" problem should be answered once more statistics are available. RHIC is scheduled to take more Au+Au data in the upcoming year.

Another interesting direction for future studies of the ridge is looking at its particle composition. An analysis using charged track correlations has already begun,

however, a study using strange particles will further our understanding of the medium that produces the ridge. With twice the statistics available, such a study should be feasible.

The analyses presented in this work are focused only on the same-side of the correlation function. Studying the away-side would be another exciting analysis direction. One notable feature of the away-side is the dip precisely  $\pi$  radians away from the same-side peak. The nature of the away-side dip and the over-all composition of the away-side is yet unknown, but presents another statistics-hungry frontier for future studies. Current studies suggest a possibility of a shock wave-like effect due to the away-side jet propagating through the medium, the formation of a Mach cone. In air, a Mach cone forms when an object moves at supersonic speeds. In a thermalized, equilibrated quark-gluon medium, a fast-moving jet may leave behind characteristic Mach rings [79]. However, the studies to determine the existence of a Mach cone surrounding the away-side jet are not yet conclusive [80].

Yet, there is another frontier. The LHC will see its first  $p + p$  collisions in 2007 and relativistic heavy ion collisions in 2008 or 2009. The LHC 10 GeV/c jet cross sections are predicted to be more than an order of magnitude higher than those at RHIC [81], making the mid- $p_T$  region ever more accessible. At the LHC the identified particles will include those containing  $c$  and possibly  $b$  quarks. Correlation studies with these will significantly expand our understanding of this quark-gluon medium, which will be even denser and hotter than the one at RHIC.

# Appendix A

## Kinematic Variables

Throughout the text, we refer to several kinematic variables without much explanation to their origin. This is a short glossary meant to explain exactly what transverse momentum ( $p_T$ ), rapidity ( $y$ ), and pseudorapidity ( $\eta$ ) are.

### Particle momentum

The total particle momentum is given by the four-momentum:

$$p^\mu = (p^0, p^1, p^2, p^3) = (E/c, p_x, p_y, p_z) = (E/c, \vec{p}) = (E/c, \vec{p}_T, p_z) \quad (\text{A.1})$$

where  $p_T = \sqrt{p_x^2 + p_y^2}$ .

### Rapidity

A useful variable to utilize in a relativistic environment is the almost boost-invariant *rapidity* variable, defined as

$$y = \frac{1}{2} \ln \left( \frac{E/c + p_z}{E/c - p_z} \right) \quad (\text{A.2})$$

To change from rapidity in one frame of reference to that in another, one needs to subtract a constant which only depends on the velocity of the moving frame,  $\beta$ :

$$y' = y - y_\beta \quad (\text{A.3})$$

$$y_\beta = \frac{1}{2} \ln \left( \frac{1 + \beta}{1 - \beta} \right) \quad (\text{A.4})$$

### Pseudorapidity

Strictly speaking, pseudorapidity  $\eta$  is a geometric, not a kinematic variable, as it can be expressed in terms of the angle between the particle momentum vector and the beam axis:

$$\eta = -\ln \left[ \tan \left( \frac{\theta}{2} \right) \right] \quad (\text{A.5})$$

Pseudorapidity can also be expressed in terms of particle momentum components:

$$\eta = \frac{1}{2} \ln \left( \frac{|\vec{p}| + p_z}{|\vec{p}| - p_z} \right) \quad (\text{A.6})$$

Thus we see that when the energy of the particle is very close to the magnitude of the total particle momentum, we can use rapidity and pseudorapidity interchangeably.

All of this and much more can be found in Reference [3].

# Appendix B

## Centrality definition in Au+Au collisions

Throughout this work, we refer to “the most central Au+Au” and “peripheral Au+Au” collisions. These refer to a parameter that is a function of the initial geometry of the colliding nuclei.

The Au ions are spherically symmetric and at the time of the collision are Lorentz-contracted. The impact parameter,  $b$ , is defined as the distance between the centers of the colliding nuclei. The larger the impact parameter, the fewer of the constituent nucleons take part in the collision. The impacted nucleons are called “participants,” while the rest are called “the spectators,” both shown in Figure B.1. The impact parameter defines the *centrality* of the collision. The most central collisions have the most participants, while the most *peripheral* collisions have the fewest.

We cannot measure  $b$  directly; thus, we use another variable to determine the centrality of the collision experimentally. The most central collisions, because they have the most participants, produce the largest number of charged tracks ( $N_{ch}$ ), which are then detected in STAR. The centrality is then determined as percent of cross-section of all the collisions based on the number of  $N_{ch}$  produced, as seen in Figure B.2

The data presented in this thesis were collected using a special “Central” trigger, as described in section 2.2.4. The on-line trigger uses the lowest ZDC counts to

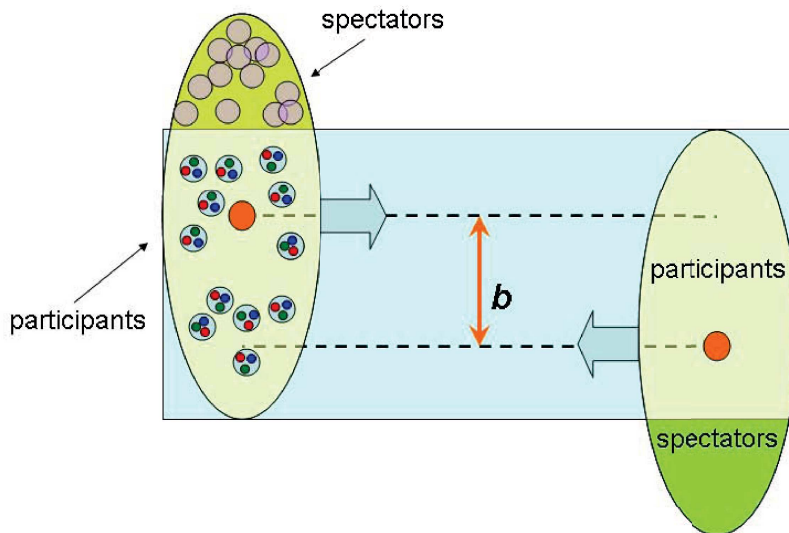


Figure B.1: A representation of two Au ions colliding. The impact, parameter,  $b$ , which is the distance between nuclei centers (shown in orange) is plotted. The participants are shown as light blue circles with red-blue-green representations of partons inside. The part of the nucleus that does not participate in the collision (made up of spectator nucleons) is shown in green.

determine the centrality of the collision, and if an event passes the predetermined threshold, it is stored by the STAR DAQ. The Central trigger typically selects the top 0-12% central event. We plot the normalized  $N_{ch}$  distribution of events selected by the Central trigger in Figure B.3. The black histogram represents the normalized min. bias distribution, given for reference.

In the Au+Au analysis presented in this work, in order to conform to the centrality of the elliptic flow measurement, we selected only the events with  $N_{ch}$  corresponding to the same  $N_{ch}$  as that in the 0-10% minimum bias data. Thus, the analyzed event sample is slightly different from events in the min. bias 0-10%, but negligibly so. The

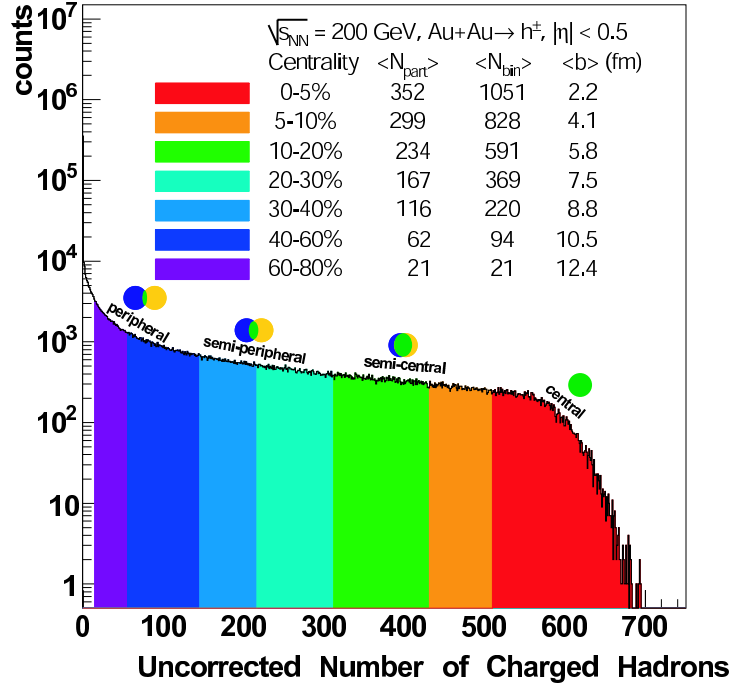


Figure B.2:  $\sqrt{s_{NN}} = 200$  GeV Au+Au minimum bias distribution with centrality definitions as labeled in the plot.

flow measurement in the modified data sample is the same within errors to the true 0-10% of the minimum bias data. The normalized  $N_{ch}$  distribution of the events used in this dissertation is shown in Figure B.4. The black histogram in the background represents the min. bias  $N_{ch}$  distribution, as before.

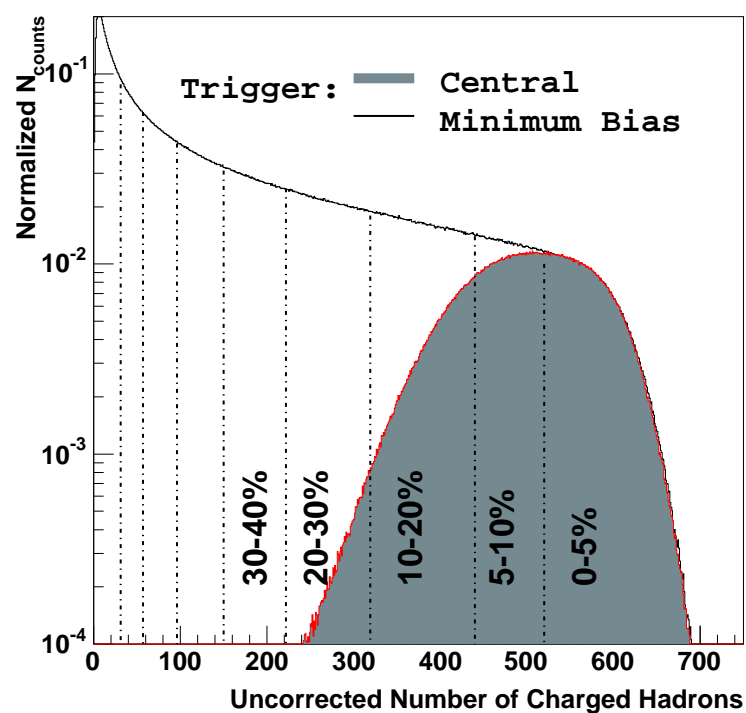


Figure B.3: Central trigger event selection. The two histograms (note the logarithmic scale) represent the normalized number of events as a function of raw charged tracks in an event for two event classes. The events selected by the Central trigger are shown as the grey histogram. The black histogram represents the minimum bias event selection. The histograms are divided in centrality classes.

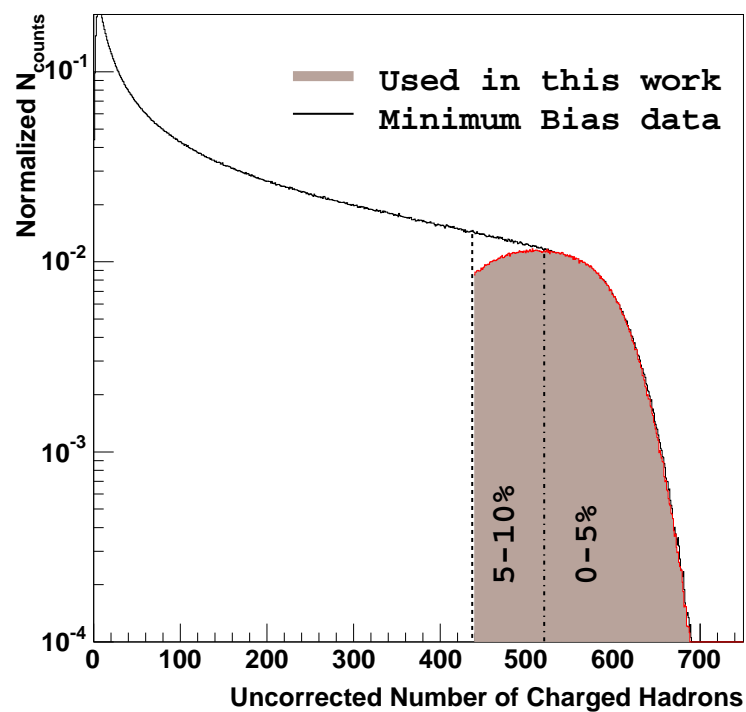


Figure B.4: Event selection for this thesis. The two histograms (note the logarithmic scale) represent the normalized number of events as a function of raw charged tracks in an event for two event classes. The events selected by the Central trigger and used in this work are shown as the purple histogram. The black histogram represents the minimum bias event selection. The two most central minimum bias event classes are shown for reference.

# Bibliography

- [1] W. M. Yao *et al.* (Particle Data Group Collaboration), *Review of particle physics*, J. Phys. **G33**, 1 (2006).
- [2] D. J. Griffiths, *Introduction to Elementary Particles* (Wiley, New York, US, 1987).
- [3] C. Y. Wong, *Introduction to high-energy heavy ion collisions*, Singapore, Singapore: World Scientific (1994) 516 p.
- [4] P. Braun-Munzinger, *Chemical equilibration and the hadron-QGP phase transition*, Nucl. Phys. **A681**, 119 (2001), nucl-ex/0007021.
- [5] J. Schaffner-Bielich, *What is so special about strangeness in hot matter?*, J. Phys. **G30**, R245 (2004), nucl-th/0408012.
- [6] S. Hamieh, K. Redlich, and A. Tounsi, *Canonical description of strangeness enhancement from  $p+A$  to  $Pb+Pb$  collisions*, Phys. Lett. **B486**, 61 (2000), hep-ph/0006024.
- [7] J. Letessier and J. Rafelski, *Hadrons and quark - gluon plasma*, Cambridge Monogr. Part. Phys. Nucl. Phys. Cosmol. **18**, 1 (2002).
- [8] R. Stock, *The strangeness signal in hadron production at relativistic energy*, (2003), hep-ph/0312039.
- [9] D. W. Sivers, S. J. Brodsky, and R. Blankenbecler, *Large Transverse Momentum Processes*, Phys. Rept. **23**, 1 (1976).

- [10] M. L. Miller, *Measurement of jets and jet quenching at RHIC*, PhD thesis, Yale University, 2003, UMI-31-25263.
- [11] E. Wang and X.-N. Wang, *Interplay of soft and hard processes and hadron  $p_T$  spectra in  $p+A$  and  $A+A$  collisions*, Phys. Rev. **C64**, 034901 (2001), nucl-th/0104031.
- [12] K. Gallmeister, C. Greiner, and Z. Xu, *Quenching of high  $p_T$  hadron spectra by hadronic interactions in heavy ion collisions at RHIC*, Phys. Rev. **C67**, 044905 (2003), hep-ph/0212295.
- [13] W. Cassing, K. Gallmeister, and C. Greiner, *Suppression of high transverse momentum hadrons at RHIC by (pre-) hadronic final state interactions*, Nucl. Phys. **A735**, 277 (2004), hep-ph/0311358.
- [14] J. Adams *et al.* (STAR Collaboration), *Evidence from  $d+Au$  measurements for final-state suppression of high  $p_T$  hadrons in  $Au+Au$  collisions at RHIC*, Phys. Rev. Lett. **91**, 072304 (2003), nucl-ex/0306024.
- [15] E. Wang and X.-N. Wang, *Parton energy loss with detailed balance*, Phys. Rev. Lett. **87**, 142301 (2001), nucl-th/0106043.
- [16] M. Gyulassy, I. Vitev, X.-N. Wang, and B.-W. Zhang, *Jet quenching and radiative energy loss in dense nuclear matter*, (2003), nucl-th/0302077.
- [17] J. Gans, *Charged particle spectra in  $p+p$  collisions at  $\sqrt{s}=200$  GeV*, PhD thesis, Yale University, 2005, nucl-ex/0111003.
- [18] J. W. Cronin *et al.*, *Production of hadrons with large transverse momentum at 200 GeV, 300 GeV, and 400 GeV*, Phys. Rev. **D11**, 3105 (1975).
- [19] B. I. Abelev *et al.* (STAR Collaboration), *Transverse momentum and centrality dependence of high- $p_T$  non-photon electron suppression in  $Au+Au$  collisions at  $\sqrt{s_{NN}} = 200$  GeV*, (2006), nucl-ex/0607012.

- [20] S. S. Adler *et al.* (PHENIX Collaboration), *Centrality dependence of charm production from single electrons measurement in Au+Au collisions at  $\sqrt{s_{NN}} = 200$  GeV*, Phys. Rev. Lett. **94**, 082301 (2005), nucl-ex/0409028.
- [21] M. A. C. Lamont (STAR Collaboration), *Recent results on strangeness production at RHIC*, J. Phys. Conf. Ser. **50**, 192 (2006), nucl-ex/0608017.
- [22] J. Adams *et al.* (STAR Collaboration), *Measurements of identified particles at intermediate transverse momentum in the STAR experiment from Au+Au collisions at  $\sqrt{s_{NN}} = 200$  GeV*, (2006), nucl-ex/0601042.
- [23] S. Salur (STAR Collaboration), *System and energy dependence of strangeness production with STAR*, Nucl. Phys. **A774**, 657 (2006), nucl-ex/0509036.
- [24] J. Adams *et al.* (STAR Collaboration), *Multi-strange baryon production in Au+Au collisions at  $\sqrt{s_{NN}} = 130$  GeV*, Phys. Rev. Lett. **92**, 182301 (2004), nucl-ex/0307024.
- [25] R. J. Fries, B. Muller, C. Nonaka, and S. A. Bass, *Hadron production in heavy ion collisions: Fragmentation and recombination from a dense parton phase*, Phys. Rev. **C68**, 044902 (2003), nucl-th/0306027.
- [26] V. Greco, C. M. Ko, and P. Levai, *Parton coalescence at RHIC*, Phys. Rev. **C68**, 034904 (2003), nucl-th/0305024.
- [27] R. C. Hwa and C. B. Yang, *Recombination of shower partons at high  $p_T$  in heavy-ion collisions*, Phys. Rev. **C70**, 024905 (2004), nucl-th/0401001.
- [28] R. C. Hwa and C. B. Yang, *Production of strange particles at intermediate  $p_T$  at RHIC*, (2006), nucl-th/0602024.
- [29] J. W. Harris, *Future of jets, heavy flavor, and EM probes at RHIC and RHIC II*, (2005), nucl-ex/0504023.
- [30] M. Harrison, T. Ludlam, S. Ozaki, *RHIC Project Overview*, Nucl. Instrum. Meth. **A499**, 235 (2003).

- [31] I. Alekseev *et al.*, *Polarized proton collider at RHIC*, Nucl. Instrum. Meth. **A499**, 392 (2003).
- [32] M. Bai *et al.*, *RHIC beam instrumentation*, Nucl. Instrum. Meth. **A499**, 372 (2003).
- [33] S. S. Adler *et al.* (PHENIX Collaboration), *PHENIX on-line systems*, Nucl. Instrum. Meth. **A499**, 560 (2003).
- [34] B. B. Back *et al.* (PHOBOS Collaboration), *The PHOBOS detector at RHIC*, Nucl. Instrum. Meth. **A499**, 603 (2003).
- [35] M. Adamczyk *et al.* (BRAHMS Collaboration), *The BRAHMS experiment at RHIC*, Nucl. Instrum. Meth. **A499**, 437 (2003).
- [36] M. Anderson *et al.*, *The STAR time projection chamber: A unique tool for studying high multiplicity events at RHIC*, Nucl. Instrum. Meth. **A499**, 659 (2003), nucl-ex/0301015.
- [37] D. Lynn *et al.*, *The STAR silicon vertex tracker: A large area silicon drift detector*, Nucl. Instrum. Meth. **A447**, 264 (2000).
- [38] M. E. Beddo *et al.* (STAR Collaboration), *STAR: Conceptual design report for the Solenoidal Tracker at RHIC*, BNL-PUB-5347.
- [39] B. I. Abelev (STAR Collaboration), *Neutral kaon interferometry in Au+Au collisions at  $\sqrt{s_{NN}} = 200$  GeV*, (2006), nucl-ex/0608012.
- [40] M. Beddo *et al.* (STAR Collaboration), *The STAR barrel electromagnetic calorimeter*, Nucl. Instrum. Meth. **A499**, 725 (2003).
- [41] F. S. Bieser *et al.* (STAR Collaboration), *The STAR trigger*, Nucl. Instrum. Meth. **A499**, 766 (2003).
- [42] J. M. Landgraf *et al.* (STAR Collaboration), *An overview of the STAR DAQ system*, Nucl. Instrum. Meth. **A499**, 762 (2003).

- [43] B. Lasiuk and T. Ullrich, *STAR C++ Class Library: User guide and reference manual*, 2001, STAR Offline Library Long Writeup.
- [44] M. Lisa, 1996, Technical report, STAR Note #0238.
- [45] S. Margetis and D. Cebra, *Main Vertex reconstruction in STAR*, 1992, STAR Note #89.
- [46] B. Abelev *et al.* (STAR Collaboration), *Measurements of strange particle production in  $p + p$  collisions at  $\sqrt{s} = 200$  GeV*, (2006), nucl-ex/0607033.
- [47] M. Estienne, *Propriétés chimiques et dynamiques des collisions d'ions lourds aux énergies du RHIC par la mesure de la production des baryons doublement étranges dans l'expérience STAR.*, PhD thesis, SUBATECH-Nantes, 2005.
- [48] B. Hippolyte, *Etude de la production d'étrangeté dans les collisions d'ions lourds ultra-relativistes à  $\sqrt{s_{NN}} = 130$  GeV avec l'expérience STAR au RHIC*, PhD thesis, Institut Pluridisciplinaire Hubert Curien, 2002.
- [49] F. Wang, Private communications, 2005.
- [50] T. Sjostrand, L. Lonnblad, and S. Mrenna, *PYTHIA 6.2: Physics and manual*, (2001), hep-ph/0108264.
- [51] B. I. Abelev *et al.* (STAR Collaboration), *Strange particle production in  $p + p$  collisions at  $\sqrt{s} = 200$  GeV*, (2006), nucl-ex/0607033.
- [52] M. Heinz (STAR Collaboration), *Strange particle production in  $p + p$  collisions at  $\sqrt{s} = 200$  GeV*, J. Phys. **G31**, S141 (2005), hep-ex/0501017.
- [53] J. Adams *et al.* (STAR Collaboration), *Azimuthal anisotropy and correlations at large transverse momenta in  $p + p$  and  $Au + Au$  collisions at  $\sqrt{s_{NN}} = 200$  GeV*, Phys. Rev. Lett. **93**, 252301 (2004), nucl-ex/0407007.
- [54] A. M. Poskanzer and S. A. Voloshin, *Methods for analyzing anisotropic flow in relativistic nuclear collisions*, Phys. Rev. **C58**, 1671 (1998), nucl-ex/9805001.

- [55] J. Slivová, *Azimuthal Correlations of High- $p_T$  Pions in 158 AGeV/c Pb-Au Collisions Measured by the CERES Experiment*, PhD thesis, Charles University in Prague, 2003, nucl-ex/0111003.
- [56] J. Adams *et al.* (STAR Collaboration), *Azimuthal anisotropy in Au + Au collisions at  $\sqrt{s_{NN}} = 200$  GeV*, Phys. Rev. **C72**, 014904 (2005), nucl-ex/0409033.
- [57] C. Adler *et al.* (STAR Collaboration), *Elliptic flow from two- and four-particle correlations in Au + Au collisions at  $\sqrt{s_{NN}} = 130$  GeV*, Phys. Rev. **C66**, 034904 (2002), nucl-ex/0206001.
- [58] N. Borghini, P. M. Dinh, and J.-Y. Ollitrault, *Flow analysis from cumulants: A practical guide*, (2001), nucl-ex/0110016.
- [59] N. Borghini, P. M. Dinh, and J.-Y. Ollitrault, *Flow analysis from multiparticle azimuthal correlations*, Phys. Rev. **C64**, 054901 (2001), nucl-th/0105040.
- [60] J. Adams *et al.* (STAR Collaboration), *Multi-strange baryon elliptic flow in Au + Au collisions at  $\sqrt{s_{NN}} = 200$  GeV*, Phys. Rev. Lett. **95**, 122301 (2005), nucl-ex/0504022.
- [61] J. Bielčíková, Private communications, 2006.
- [62] N. N. Ajitanand *et al.*, *Decomposition of harmonic and jet contributions to particle-pair correlations at ultra-relativistic energies*, Phys. Rev. **C72**, 011902 (2005), nucl-ex/0501025.
- [63] J. Adams *et al.* (STAR Collaboration), *Minijet deformation and charge-independent angular correlations on momentum subspace ( $\eta, \phi$ ) in Au+Au collisions at  $\sqrt{s_{NN}} = 130$  GeV*, Phys. Rev. **C73**, 064907 (2006), nucl-ex/0411003.
- [64] J. Putschke (STAR Collaboration), *Near-side  $\Delta\eta$  correlations of high- $p_T$  hadrons from STAR*, AIP Conf. Proc. **842**, 119 (2006).
- [65] J. Bielčíková, *Azimuthal and pseudo-rapidity correlations with strange particles at intermediate- $p_T$  at RHIC*, (2007), nucl-ex/0701047.

- [66] J. Putschke, *Intra-jet correlations of high- $p_T$  hadrons from STAR*, (2007), nucl-ex/0701074.
- [67] J. Bielčíková, *High- $p_T$  strange particle spectra and correlations in STAR*, (2006), nucl-ex/0612028.
- [68] H. Caines, *Using strange hadrons as dense matter probes*, (2006), nucl-ex/0608008.
- [69] F. Karsch, *Lecture Notes in Physics*, (2002), vol 583.
- [70] J. Adams *et al.* (STAR Collaboration), *Experimental and theoretical challenges in the search for the quark gluon plasma: The STAR collaboration's critical assessment of the evidence from RHIC collisions*, Nucl. Phys. **A757**, 102 (2005), nucl-ex/0501009.
- [71] S. S. Adler *et al.* (PHENIX Collaboration), *Modifications to di-jet hadron pair correlations in Au + Au collisions at  $\sqrt{s_{NN}} = 200$  GeV*, Phys. Rev. Lett. **97**, 052301 (2006), nucl-ex/0507004.
- [72] D. J. Hofman (PHOBOS Collaboration), *Latest results from PHOBOS*, (2007), nucl-ex/0701051.
- [73] R. C. Hwa and C. B. Yang, *Recombination model for fragmentation: Parton shower distributions*, Phys. Rev. **C70**, 024904 (2004), hep-ph/0312271.
- [74] J. Binnewies, G. Kramer, M. Erdmann, and B. A. Kniehl, *Access to the NLO gluon distribution of the photon*, Prepared for Workshop on Future Physics at HERA (Preceded by meetings 25-26 Sep 1995 and 7-9 Feb 1996 at DESY), Hamburg, Germany, 30-31 May 1996.
- [75] N. Armesto, *Flow effects on jet profiles and multiplicities*, Eur. Phys. J. **C43**, 255 (2005), hep-ph/0501214.
- [76] A. Majumder, B. Muller, and S. A. Bass, *Longitudinal broadening of quenched jets in turbulent color fields*, (2006), hep-ph/0611135.

- [77] C. B. Chiu and R. C. Hwa, *Pedestal and peak structure in jet correlation*, Phys. Rev. **C72**, 034903 (2005), nucl-th/0505014.
- [78] S. A. Voloshin, *Two particle rapidity, transverse momentum, and azimuthal correlations in relativistic nuclear collisions and transverse radial expansion*, Nucl. Phys. **A749**, 287 (2005), nucl-th/0410024.
- [79] R. A. Lacey, *Is there a sonic boom in the little bang at RHIC?*, (2006), nucl-ex/0608046.
- [80] J.-y. Jia (PHENIX Collaboration), *From Mach cone to reappeared jet: What do we learn from PHENIX results on non-identified jet correlation?*, AIP Conf. Proc. **828**, 219 (2006), nucl-ex/0510019.
- [81] A. Accardi *et al.*, *Hard probes in heavy ion collisions at the LHC: Jet physics*, (2004), hep-ph/0310274.

# Index

- $R_{AA}$ , 10, 11, 15, 18, 19
- $R_{CP}$ , 11, 15, 19
- $\gamma$ -jet, 16
- AGS, 26, 27
- associated, 14, 60
- back-to-back jet, 13, 19
- BBC, 32, 44
- BEMC, 32, 40, 41, 44, 46, 77
- Bethe-Bloch, 55
- Bethe-Bloch curves, 38
- Bethe-Bloch formula, 38
- Booster, 26, 27
- BRAHMS, 27, 30
- canonical suppression, 107
- cascade, 52
- Cronin effect, 11
- CTB, 31, 42, 49, 62
- CTB matching, 49, 50
- daughter tracks, 52
- decay topology, 51
- dilepton, 16
- disappearance of the away-side jet, 14
- Drell-Yan, 16
- EEMC, 32, 40
- EMC, 77
- FTPC, 32, 34
- hidden charm, 15, 32
- ionization points, 47
- Kalman filter, 48
- leading particle, 14
- LHC, 120
- LINAC, 26
- nuclear modification factor, 10, 15
- open charm, 15
- partonic energy loss, 11
- PHENIX, 27, 29, 32, 36, 114
- PHOBOS, 27, 29, 30, 114
- PMD, 32
- primary vertex, 49, 50, 63
- PYTHIA, 70
- QGP, 10, 15, 16, 29, 107
- recombination mechanism, 20
- Recombination Model, 20, 22, 23, 116

RHIC, 14, 16, 19, 24, 26, 27, 31, 40, 41,  
107, 114, 119, 120

ridge, 102

SMD, 41

SSD, 40, 47

STAR, 27, 29, 32, 34, 36, 38, 41, 44, 86,  
107, 114

SVT, 32, 34, 40, 47

TOF, 32

TPC, 31, 34–37, 40, 41, 47, 49, 52, 54, 64,  
102

track merging, 102

tracking, 41

trigger, 60

triggering, 41

Upton, NY, 24

Van de Graaff, 26

ZDC, 29, 31, 41, 123

ZYAM, 92, 93